

JAERI - M
94-027

PROGRESS REPORT ON SAFETY RESEARCH ON RADIOACTIVE
WASTE MANAGEMENT FOR THE PERIOD
APRIL 1992 TO MARCH 1993

March 1994

(Eds.) Susumu MURAOKA, Muneaki SENOO and Keiichi SEKINE

JAERI-Mレポートは、日本原子力研究所が不定期に公刊している研究報告書です。
入手の間合わせは、日本原子力研究所技術情報部情報資料課（〒319-11茨城県那珂郡東海村）あて、お申しこしてください。なお、このほかに財団法人原子力弘済会資料センター（〒319-11 茨城県那珂郡東海村日本原子力研究所内）で複写による実費頒布をおこなっております。

JAERI-M reports are issued irregularly.

Inquiries about availability of the reports should be addressed to Information Division
Department of Technical Information, Japan Atomic Energy Research Institute, Tokai-mura, Naka-gun, Ibaraki-ken 319-11, Japan.

©Japan Atomic Energy Research Institute, 1994

編集兼発行	日本原子力研究所
印 刷	いばらき印刷株

Progress Report on Safety Research on Radioactive Waste
Management for the Period April 1992 to March 1993

(Eds.) Susumu MURAOKA, Muneaki SENOO and Keiichi SEKINE

Department of Environmental Safety Research
Tokai Research Establishment
Japan Atomic Energy Research Institute
Tokai-mura, Naka-gun, Ibaraki-ken

(Received January 31, 1994)

This report summarizes the research and development activities on radioactive waste management at the Engineered Barrier Materials Laboratory, Shallow Land Migration Laboratory, Environmental Geochemistry Laboratory and Environmental Radiochemistry Laboratory of the Department of Environmental Safety Research during the fiscal year of 1992 (April 1, 1992-March 31, 1993).

The topics are as follows:

- 1) As for waste forms and engineered barrier material, performance assessment studies were carried out on various waste forms, buffer materials and mortar.
- 2) In the safety evaluation study for shallow land disposal, migration behavior in the soil layer were studied.
- 3) In the safety evaluation study for geological disposal, chemical behavior of nuclide in water, nuclide migration and fixation in geosphere were studied.
- 4) Distribution of uranium and migration of uranium series nuclide in uranium ore were examined as a natural analogue study.

Keywords: High-level Waste, Low-level Waste, Waste Form, Engineered Barrier, Natural Barrier, Geosphere, Migration, Fixation, Natural Analogue

放射性廃棄物処理処分の安全性に関する平成4年度報告書

日本原子力研究所東海研究所環境安全研究部

(編) 村岡 進・妹尾 宗明・関根 敬一

(1994年1月31日受理)

人工バリア研究室、浅地処分研究室、深地処分研究室及び環境放射化学研究室において、平成4年度に実施した放射性廃棄物処理処分の安全性に関する研究成果をまとめた。

その内容は次の通りである。

- 1) 廃棄物固化体及び人工バリア材の研究開発では、各種固化体、緩衝材及びモルタルの性能評価試験を継続した。
- 2) 浅地中埋設に関する安全評価試験では、土壌中の核種移行試験を継続した。
- 3) 地層処分の安全性評価試験では、核種の水中での化学的挙動、地層中での核種の移行・固定機構の研究を継続した。
- 4) ナチュラルアナログ研究として、ウラン鉱床中のウラン系列核種の移行・分布に関する研究を継続した。

Contents

Introduction

1. Research and Development of Waste Forms and Engineered Barrier Materials	1
1.1 Performance of Waste Forms	1
1.1.1 Durability of High-level Waste Glass in Flowing Groundwater under Gamma-ray Irradiation	1
1.1.2 Long Term Leaching Test of Low Level Radioactive Solidified Waste	7
1.2 Performance of Ceramic Waste Forms	22
1.2.1 Preparation of Cm-doped Perovskite Material	22
1.2.2 Durability of an $\text{La}_2\text{Zr}_2\text{O}_7$ Waste Form Containing Various Amounts of Simulated HLW Elements	26
1.2.3 8 mol% Yttria-stabilized Zirconia (YSZ) and Alumina-based Ceramic Waste Forms Containing Ce and Nd ..	31
1.3 Performance of Engineered Barrier Materials	39
1.3.1 Sorption Characteristics of Neptunium by Smectite	39
1.3.2 Sorption Behavior of ^{14}C by Mortar	42
1.3.3 Changes in the Properties of Mortar Containing Durability Improving Agent under Gamma-ray Irradiation ..	45
2. Safety Evaluation Study on Shallow Land Disposal	50
2.1 Nuclide Migration Study	50
2.1.1 Migration Behavior of Radionuclides on the Undisturbed Soil Layer	50
2.1.2 Ground Surface Radionuclide Migration Test	54
2.1.3 Influence of Humic Acid on Migration of ^{60}Co , ^{85}Sr and ^{137}Cs in Coastal Sandy Soil	59
2.1.4 Migration Behavior of Bicarbonate- ^{14}C in Underground Soil Layer	67
3. Safety Evaluation Study on Geological Disposal	72
3.1 Chemical Behavior of Radionuclides in Water	72
3.1.1 Effect of Complexation on Solubility of Pu(IV) in Aqueous Carbonate System	72
3.2 Nuclide Migration and Retardation	86
3.2.1 Redistribution of Neptunium(V) during the Crystallization of Amorphous Ferrihydrite	86

3.3 Long-term Radionuclide Fixation Mechanisms	91
3.3.1 The Use of Color to Quantity Effects of pH and Temperature on the Crystallization Kinetics of Goethite under High Alkaline Conditions	91
4. Natural Analogue Study	106
4.1 Groundwater Geochemistry and Distribution of U-series Radionuclides in the Koongarra Uranium Ore Deposit, Australia	106

目 次

まえがき

1. 廃棄物固化体と人工バリアに関する研究開発	1
1.1 廃棄物固化体の性能	1
1.1.1 γ 線照射下, 流動地下水中的の高レベル廃棄物ガラス固化体の耐久性	1
1.1.2 低レベル廃棄物固化体の長期浸出試験	7
1.2 セラミック固化体の性能	22
1.2.1 Cm含有ペロブスカイト材の作製	22
1.2.2 模擬高レベル廃棄物元素含有ランタンジルコネートの耐久性	26
1.2.3 Ce, Nd含有8モルイットリア安定化ジルコニア及びアルミナ基セラミック固化体	31
1.3 人工バリア材の性能	39
1.3.1 スメクタイトへのネプツニウムの吸着	39
1.3.2 モルタルへの ^{14}C の吸着	42
1.3.3 耐久性改善材添加モルタルの γ 線照射による特性変化	45
2. 浅地中埋設の安全性評価研究	50
2.1 核種移行研究	50
2.1.1 不飽和土壤中における放射性核種の移行挙動	50
2.1.2 地表面核種移行試験	54
2.1.3 海岸砂質土壤中における ^{60}Co , ^{85}Sr 及び ^{137}Cs の移行に及ぼすフミン酸の影響	59
2.1.4 土壤中における重炭酸型 ^{14}C の移行挙動	67
3. 地層処分の安全性評価研究	72
3.1 核種の水中の化学的挙動	72
3.1.1 炭酸水溶液系におけるプルトニウム(IV)の溶解度に対する錯生成の影響	72
3.2 核種の移行と遅延	86
3.2.1 非晶質鉄酸化物の結晶化過程におけるネプツニウム(V)の再分配	86
3.3 長期の核種固定機構	91
3.3.1 色による針鉄鉱結晶化の速度論的研究	91
4. ナチュラルアナログ研究	106
4.1 豪州クングラウラン鉱床の地下水化学とウラン系列放射性核種の分布	106

Introduction

In order to achieve the safe disposal of radioactive wastes, it is necessary to promote the development of waste management and safety assessment methodology.

The Japan Atomic Energy Research Institute (JAERI) has been conducting safety assessment study and development of new technology to contribute the establishment of national system for the radioactive waste management in Japan.

This report summarizes the status and results of studies performed in the fiscal year 1992 at Engineered Barrier Materials Laboratory, Shallow Land Migration Laboratory, Environmental Geochemistry Laboratory and Environmental Radiochemistry Laboratory of the Department of Environmental Safety Research, JAERI.

The progress report series have been issued in the following numbers: JAERI-M 82-145, 83-076, 84-133, 85-090, 86-131, 87-131, 88-201, 89-192, 91-019, 92-022 and 93-037.

1. Research and Development of Waste Forms and Engineered Barrier Materials

1.1 Performance of Waste Forms

1.1.1 Durability of High-level Waste Glass in Flowing Groundwater under Gamma-ray Irradiation

H. Kamizono

1. Introduction

Disposal sites suitable for the isolation of high-level waste glass (HLW glass) may be constructed in geologic formations more than several hundred meters below the land surface. During the first several hundreds of years after the disposal, a considerable amount of ^{137}Cs emits gamma-ray to the surrounding area. If the glass comes into contact with groundwater during this period, leaching behavior from the glass will be affected by radiolysis in groundwater.

There are many studies on the effects of gamma-irradiation on the HLW glass durability in water. However, in most studies leach experiments are carried out under static conditions, and therefore in the present study we examine the dynamic effects of gamma-irradiation on the HLW glass in flowing groundwater.¹⁻⁴⁾ We also mention that groundwater is not oxidized nor acidified under gamma-irradiation in the absence of nitrogen and oxygen.

2. Experimental

2.1 Preparation of Simulated HLW Glass

The simulated HLW glass containing 11.8 wt% of simulated fission products was prepared.

2.2 Leach Apparatus

The continuous-flow leach tests were carried out at $90 \pm 1^\circ\text{C}$ using an MCC-4 type leaching apparatus. The apparatus had been improved in five ways as follows.

- (1) The shape of the leach containers was designed to provide three

glass-surface-area to leachant-volume ratios of 10, 1 and 0.1 cm^{-1} . These conditions need about fifty pineapple-sliced specimens, five pineapple-sliced specimens, and one discoid specimen, respectively.

(2) The leach containers and the connected leachant-inlets and outlets were made of stainless steel capable of enduring gamma-irradiation of about 1 MGy.

(3) The movable parts of the apparatus, such as the receiver bottles, which had to be handled throughout the experiments, were designed to be easily manipulated in a hot cell.

(4) All outlets were covered with heaters to maintain their temperature at about 90°C in order to prevent any precipitation of elements while the leachates were transported to the receiver bottles.

(5) The air in the upper space of the reservoirs and the receiver bottles was replaced with argon which was flowing at a rate of $50 \text{ cm}^3/\text{min}$. This prevents the influence of nitrogen and oxygen from air.

2.3 Synthetic Groundwater

Synthetic J-13 tuff groundwater was prepared in accordance with the recipe described by Johnson.⁵⁾

3. Results

3.1 Eh-pH Excursion during Leaching

Figure 1 shows an example of the Eh-pH excursion in the present experiments. The results show that the flowing groundwater tends to be reduced under a constant gamma-irradiation of about 10^4 R/h .

The relationship between the Eh values and the pH values can be expressed, for example, at a flow rate of 1000 ml/year with the irradiation.

$$\text{Eh} = 0.780 - 0.060\text{pH},$$

and for the same flow rate without the irradiation,

$$\text{Eh} = 0.914 - 0.069\text{pH}.$$

Note that the reduction is estimated as much as -0.12 V for the present conditions.

3.2 Concentrations of the Elements in the Leachates

At a flow rate of 10000 ml/year, the concentrations of the network formers Si and B increase for the initial 20 day duration and then reach constants. At a flow rate of 1000 ml/year, however, the duration of about 400 days is needed to achieve the steady state conditions (Fig. 2).

The alkaline earth elements Ca and Mg show "negative leach rates" as a result of adsorption of Ca and Mg onto the sylanol groups on the glass surface (Fig. 2). The word "negative" means that the concentration of the elements in the leachates are lower than those in the fresh leachant. This phenomenon was observed in the experiments with and without the gamma-irradiation.

4. Discussion

4.1 Eh-pH Excursion during Leaching

Gamma-irradiation is a cause of the formation of hydrogen radicals which is reductive in a chemical reaction. In addition, hydrogen radical may form another reducing agent O_2^- in alkaline or neutral groundwater. We think that, in alkaline groundwater without much oxygen, some elements such as Ce may be reduced. When a reduced chemical species of an element has higher solubility in water, then the gamma-irradiation will effect an increase of the leach rates. For example, $Ce(OH)_3$ may have higher solubility in water than $Ce(OH)_4$, and is expected to dissolve more easily in reducing environments.

However, this issue is sometimes controversial in that divalent iron is reported to be oxidized under similar irradiation conditions. This is because oxidizing potential of divalent iron is not so high, and it is easily oxidized by the secondary chemical species H_2O_2 rather than reduced by hydrogen radicals.

4.2 Leach Rates of the Elements Studied

The elements studied can be divided into three groups. First, leach rates of the network former elements Si and B are not affected easily by the irradiation, because they are single valent cations under the present experimental conditions, and their solubilities are stable during the irradiation.

Second, leach rates of alkaline earth elements Ca and Mg tend to decrease with time as a result of the adsorption onto silanol groups on the glass surface. However, this is independent of the cumulative dose and were also observed in a blank run without irradiation.

Third, as mentioned above, leach rates of the divalent cations may be affected considerably. When an element which is oxidized or reduced by the irradiation has a higher solubility, then leach rates of the element is to be higher under irradiation.

5. Concluding Remarks

Our experiments simulate the conditions in a geologic disposal site over several hundreds of years after burial, where radiation dose is still in the order of about 10^4 R/hour. This irradiation to the surrounding groundwater is a major issue for predicting leach rates of HLW glass.

Long-lived alpha-emitters such as Pu and Cm also change the groundwater chemistry, and therefore study on gamma-irradiation will clarify part of the influence of the alpha-emitters on the leaching behavior in a long run. This will be studied further in the near future with HLW glass containing TRU elements.

Acknowledgements

The present study was initiated under a cooperative research program between the United States Nuclear Regulatory Commission (USNRC) and the Japan Atomic Energy Research Institute (JAERI).

References

- 1) H. Kamizono, I. Shimizu and T. Banba, "Continuous-Flow Leach Tests of Simulated High-Level Waste Glass in Synthesized Groundwater and Deionized Water", J. Nucl. Sci. Technol., 24[4], 308-314 (1987).

- 2) H. Kamizono, T. Sagawa and S. Tashiro, "Continuous-Flow Leach Tests of Simulated High-Level Waste Glass in Synthetic Basalt Groundwater", Waste Manage., 9[4], 189-194 (1989).
- 3) H. Kamizono, T. Sagawa and S. Tashiro, "Factor of Dilution with Freshly Pumped Leachant in Continuous-Flow Leach Tests on High-Level Waste Glass", J. Nucl. Sci. Technol., 26[8], 811-813 (1989).
- 4) H. Kamizono et al., JAERI memo 03-246 (1991).
- 5) K.M. Johnson, "Laboratory Procedures for the Preparation of Simulated Tuff Groundwater", Quality Assurance Document, QA003, Devision 0, Cortest Columbus, Inc., Columbus, Ohio, (1988).

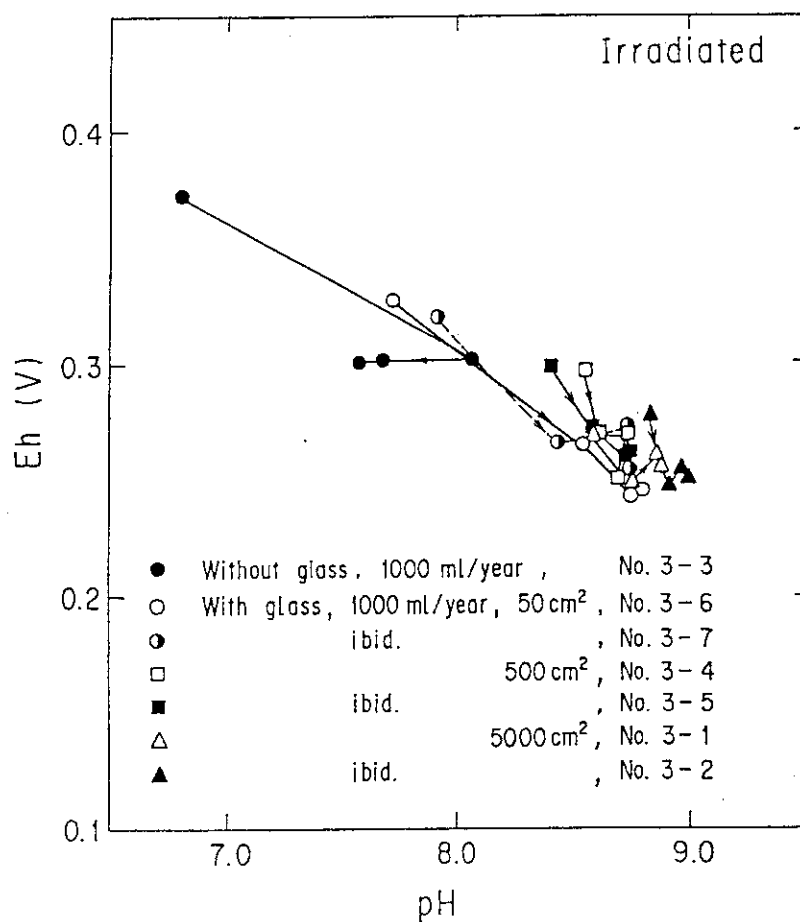


Fig. 1 Eh-pH excursion at a flow rate of 1000 ml/year with gamma-irradiation.

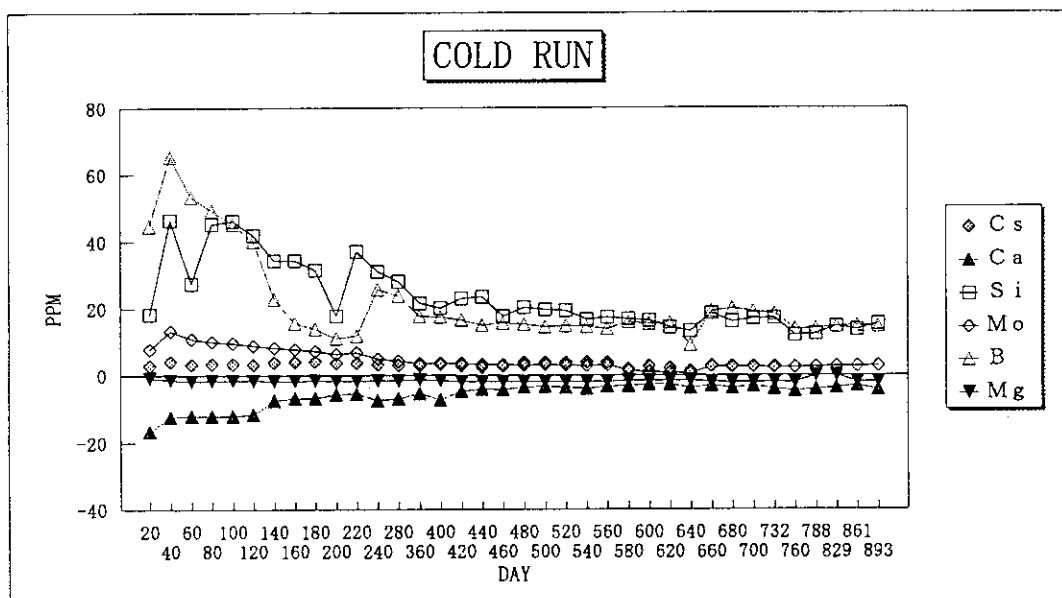


Fig. 2 Leach rates of the elements studied at a flow rate of 1000 ml/year and a glass surface area of 5000 cm².

1.1.2 Long Term Leaching Test of Low Level Radioactive Solidified Waste

T. Takeda, K. Saito and H. Takazawa

1. Introduction

Large quantity of LLW (Low Level Radioactive Waste) are generated from various facilities such as power plants, research organizations and industries every year. Most of LLWs are generated from nuclear power plants, and they are categorized into liquid wastes, combustible wastes, miscellaneous solid wastes and other wastes.

LTLT (Long Term Leaching Test) was started from 1982 fiscal year as shown in Table 1 in JAERI (Japan Atomic Energy Research Institute) based on the budget of STA (Science and Technology Agency of Japan). In 1989, LTLT on homogeneous waste forms was finished, and LTLT on miscellaneous waste forms was started in 1988 fiscal year and have been conducted.

The liquid wastes have been concentrated and converted to stable forms such as homogeneously solidified with cement, bitumen (asphalt) and plastic forms, and stored in the site of nuclear power plants. The solidified wastes are safely disposed of shallow land at Rokkasho-mura in Aomori Prefecture, Japan.

2. Schematic Diagram of Test Equipments

The outlined structure of a test unit for actual size waste in sea and/or land water is shown in Fig. 1. Circulation speed by stirrer is about 2 cm/sec around a body of waste form. One for actual size waste in soil is shown in Fig. 2. All of these leaching test units are opened to atmosphere.

Total volume of water in a test unit for sea or land water condition was decided to be equivalent to about 10 times of a form as shown in Tables 2 and 3.

Actual size simulated homogeneous forms were manufactured with addition of three radionuclides, which are two typical fission products, (a) Cs-137 and (b) Sr-90, and a typical corrosion product, (c) Co-60 as listed in Tables 1 through 3.

The solidification matrices used for LTLT were (a) cement, (b)

asphalt and (c) plastic.

LTLT on homogeneous forms was carried out for about 4 years. But, leaching time for each form is about 1,000 days in maximum. In order to study the effect of environments of disposal sites on leaching phenomena, LTLT was conducted under the following three environmental conditions.

(1) Sea water conditions :

Eight forms (K1 through K8) as listed in Table 1 were immersed in test units with full of real sea water of 2°C, which simulated deep sea water in case of sea disposal.

(2) Land water conditions :

Ten forms (R1 through R10) as listed in Table 2 were immersed in test units with full of deionized water of 20°C, which simulated groundwater in case of shallow land disposal.

(3) Soil conditions :

Sixteen forms (D1 through D16) as listed in Table 3 were buried in test units with full of soils saturated with deionized water of 20°C, which simulated soils containing groundwater in case of shallow land disposal.

The combination of actual size waste forms tested is summarized in Table 4.

In addition, many kinds of small size leaching tests (IAEA size tests) were conducted as shown in Table 5.

3. Test Conditions and Test Procedures

Drum containers on the surface of solidified wastes should be corroded away by groundwater before long after the disposal. From a view point of conservative evaluation, all of steel drum on the surface of these forms were peeled off before starting of leaching test.

In the leaching test in water, solidified waste form without steel drum (bared form) was immersed in sea water of about 2°C or land water of about 20°C under constant stirring condition. Leachate was sampled every 1 or 2 months. After sampling, whole of water remaining in a test unit was changed to fresh sea or land water.

Gamma-ray emitters such as Cs-137 and Co-60 in leachate were directly measured by gamma-ray spectrometer adopted with pure Ge semiconductor

detector after concentration using evaporator. On the other hand, beta-ray emitter such as Sr-90 in leachate was chemically separated from gamma-ray emitters with the standard procedure using fuming nitric acid, which was authorized by STA. And Sr-90 was measured by a 2π gas flow counter under the radiological equilibrium of Sr-90 and Y-90.

In the leaching test in soil, solidified waste form without steel drum was immersed in the wet soil, whose thickness was about 310 cm for waste form of 200 liters size and about 180 cm for waste form of 50 liters size. The annular lateral and upper parts of waste form were covered with soil. Soil of each test unit was saturated with land water of 20°C. Leachate leaked out through soil layer was also sampled every 1 or 2 months. Radionuclides in leachate was measured by means of the same procedure of sea and land water conditions. After sampling, whole of remaining water in a test unit was drained out, and fresh deionized water was fed into a test unit for next leaching test duration.

After the termination of LTLT, all forms tested in sea, land waters and in soil stack were pulled out from respective test units, and were disassembled into small pieces with a cutter in order to observe degradation of matrix, to measure distribution of radionuclides in the body of waste forms and to analyze some of chemical elements.

4. Cumulative Leaching Ratio (F) in the Cases of Sea Water and Land Water

After the measurements of radioactivity in leachate of sea water or land water every 1 or 2 months, radioactivity measured was corrected considering the decay time of radionuclides. Cumulative leaching ratio (F) of radionuclides such as Co-60, Sr-90 and Cs-137 was calculated by the following formula.

$$F = \sum A_i / A_o$$

where, A_o is initial radioactivity of radionuclide charged into a solidified form, and A_i is radioactivity in leachate of sea or land water during of sampling times (i-1) through (i).

Some transient curves of the cumulative leaching ratio F of each nuclide for sea water condition are shown in Fig. 3, and for land water condition in Fig. 4.

5. Cumulative Leaching Ratio (F') in the Case of Soil

In the case of soil condition, cumulative leaching ratio (F') of radionuclides such as Co-60, Sr-90 and Cs-137 was calculated by the following formula.

$$F' = \sum A_i' / A_o$$

where, A_o is initial radioactivity of radionuclide charged into a solidified form, and A_i' is radioactivity in leachate leaked from soil layer into drained water during of sampling times (i-1) through (i).

Some transient curve of the cumulative leaching ratio F' of each nuclide is shown in Fig. 5 for soil condition.

6. Miscellaneous Waste Forms of LTLT

LTLT is now conducted for three kinds of actual size simulated miscellaneous waste forms.

The first is the non-compacted metal wastes with Non-liner Steel Drum, the second is the non-compacted metal wastes with Liner Steel Drum, and third is the compacted metal wastes with Liner Steel Drum. The manufacturing processes of simulated miscellaneous forms is schematically shown in Figs. 6 through 8.

Test conditions of these miscellaneous waste forms are the same as those of homogeneous waste under which the land water was used.

The detail of miscellaneous waste forms is summarized in Tables 6 and 7.

For the specimen which has finished the leaching test, a cutting work has initiated to inspect the inside leaching phenomena of the specimen.

Table 1 Major Items of Actual Size Waste Form in Sea Water at Preparation.

Test Piece Number	Nominal Volume		Solidification Agent (Matrix)	Chemical Form of Waste before Preparation	Mixing Ratio of Waste	Radionuclide Added to Waste Form(mCi)			Diameter(mm)			Height (mm)	Weight (kg)
	Classification of Waste Form	l				⁶⁰ Co	⁹⁰ Sr	¹³⁷ Cs	Top	Center	Bottom		
K 1	Simulated BWR Cement Waste	200	Slug Cement Type C in JIS	ca.15% Na ₂ SO ₄ soln. +Fe ₂ O ₃	0.05	4.4	0.98	3.8	567	568	568	726	359.4
K 2						4.4	0.98	3.8	567	568	568	725	359.0
K 3				ca.20% Na ₂ SO ₄ soln. +Fe ₂ O ₃	0.067	0.67	0.45	0.32	567	567	568	744	373.8
K 4						0.67	0.45	0.32	567	568	568	748	375.2
K 5	Simulated PWR Asphalt (Bitumen) Waste	100	Straight Asphalt(Bitumen)(Penetration 60-80)	H ₂ BO ₃ soln. +NaOH soln.	0.35	2.3	3.0	0.58	452	452	---	674	138.2
K 6						1.8	2.4	0.46	451	452	---	530	109.4
K 7	Simulated BWR Plastic Waste	50	Unsaturated Polyester	Na ₂ SO ₄ soln. +Fe ₂ O ₃	0.60	3.4	2.0	0.76	385	385	385	432	86.6
K 8						3.4	2.0	0.76	385	385	385	434	87.2

(Note) Mixing Ratio of Waste : Waste / Test Piece in Weight

Table 2 Major Items of Actual Size Waste Form in Land Water at Preparation.

Test Piece Number	Nominal Volume		Solidification Agent (Matrix)	Chemical Form of Waste before Preparation	Mixing Ratio of Waste	Radionuclide Added to Waste Form(mCi)			Diameter(mm)			Height (mm)	Weight (kg)
	Classification of Waste Form	l				⁶⁰ Co	⁹⁰ Sr	¹³⁷ Cs	Top	Center	Bottom		
R 1	Simulated BWR Cement Waste	200	Slug Cement Type C in JIS	ca.15% Na ₂ SO ₄ soln. +Fe ₂ O ₃	0.05	0.67	0.45	3.1	568	568	568	760	372.2
R 2						0.66	0.44	3.1	568	567	567	751	369.4
R 3				ca.20% Na ₂ SO ₄ soln. +Fe ₂ O ₃	0.067	0.78	0.52	0.30	568	567	567	706	360.0
R 4						0.78	0.52	0.31	567	567	567	707	362.2
R 5		50		ca.15% Na ₂ SO ₄ soln. +Fe ₂ O ₃	0.05	0.19	0.13	0.092	390	390	390	463	107.6
R 6				ca.20% Na ₂ SO ₄ soln. +Fe ₂ O ₃	0.067	0.19	0.13	0.091	390	390	389	453	107.8
R 7	Simulated PWR Asphalt (Bitumen) Waste	50	Straight Asphalt(Bitumen)(Penetration 40-60)	H ₂ BO ₃ soln. +NaOH soln.	0.40	1.6	0.70	0.79	367	367	367	397	* 60.8
R 8						1.6	0.70	0.79	367	367	367	409	* 63.0
R 9	Simulated BWR Plastic Waste	50	Unsaturated Polyester	Na ₂ SO ₄ soln. +Fe ₂ O ₃	0.60	0.60	0.36	1.1	385	385	385	385	79.0
R 10						0.60	0.36	1.1	384	385	385	384	78.4

(Note) * : Weight Including Steel Drum

Table 3 Major Items of Actual Size Waste Form in Soil at Preparation.

Test Piece Number	Nominal Volume	Kind of Soil	Solidification Agent (Matrix)	Chemical Form of Waste before Preparation	Mixing Ratio of Waste	Radioisotope Added to Waste Form(μCi)			Diameter(mm)			Height (mm)	Weight (kg)	
	Classification of Waste Form					Z	Top	Center	Bottom					
										⁶⁰ Co	¹³⁷ Sr			¹³⁷ Cs
D 1	Simulated BWR Cement Waste	200	Masado S	Slag Cement Type C in JIS	ca.15% Na ₂ SO ₄ soln. +Fe ₂ O ₃	0.05	0.64	0.43	0.30	567	567	567	744	361.0
D 2		Sand A	0.66				0.44	0.31	567	567	567	752	369.2	
D 3		Mixed S.	0.68				0.45	0.32	568	567	568	771	379.8	
D 4		Sand A	0.65				0.42	0.30	568	568	569	720	353.2	
D 5		50	Masado S				0.21	0.14	0.097	391	390	390	498	114.6
D 6			Sand A				0.18	0.12	0.085	390	390	388	430	101.0
D 7			Mixed S.				0.21	0.14	0.098	390	389	389	499	116.4
D 8			Sand C				0.20	0.14	0.093	390	389	390	447	109.8
D 9	Simulated PWR Asphalt (Bitumen) Waste	50	Masado S	Straight Asphalt (Bitumen) (Penetration 40-60)	H ₃ BO ₃ soln. +NaOH soln.	0.40	0.77	0.34	0.39	390	389	390	365	55.2
D 10		Sand A	0.78				0.35	0.39	390	389	390	394	59.2	
D 11		Mixed S.	0.77				0.34	0.39	390	390	395	406	60.4	
D 12		Sand A	0.78				0.35	0.39	389	390	390	399	60.8	
D 13	Simulated BWR Plastic Waste	50	Masado S	Unsaturated Polyester	Na ₂ SO ₄ soln. +Fe ₂ O ₃	0.60	0.61	0.37	1.1	384	385	386	394	80.6
D 14		Sand A	0.60				0.36	1.1	384	384	385	384	78.2	
D 15		Mixed S.	0.60				0.36	1.1	384	385	384	392	78.8	
D 16		Sand A	0.60				0.36	1.1	384	384	385	384	78.6	

(Note) Masado Soil (One of Typical Japanese Soils) : Sampled in Hitachi City, Ibaraki Prefecture
 Sand-dune Soil A : Sampled in Oh-arai Town, Ibaraki Prefecture
 B : Sampled in Asahi Village, Ibaraki Prefecture
 C : Sampled in Rokkasho Village, Aomori Prefecture
 Volcanic Ash Soil : Sampled in Tama Ward, Tokyo
 Mixed Soil : Sand-dune Soil A 70% + Volcanic Ash Soil 30%

Table 4 Combination of Actual Size Waste Forms

Nominal Volume Classification of Waste Form	l	Solidification Agent (Matrix)	Chemical Form of Waste before Preparation	Test Piece Number		
				Sea Water	Land Water	Soil
Simulated BWR Cement Waste	200	Slag Cement Type C in JIS	ca.15% Na ₂ SO ₄ soln. + Fe ₂ O ₃	K 1 K 2	R 1 R 2	D 1 D 4
			ca.20% Na ₂ SO ₄ soln. + Fe ₂ O ₃	K 3 K 4	R 3 R 4	
	50		ca.15% Na ₂ SO ₄ soln. + Fe ₂ O ₃		R 5	D 5 D 8
			ca.20% Na ₂ SO ₄ soln. + Fe ₂ O ₃		R 6	
Simulated PWR Asphalt (Bitumen) Waste	100	Straight Asphalt (Penetration: 60-80)	H ₃ BO ₃ soln. + NaOH soln.	K 5 K 6		
	50	(Penetration: 40-60)			R 7 R 8 (*)	D 9 D 12
Simulated BWR Plastic Waste	50	Unsaturated Polyester	Na ₂ SO ₄ soln. + Fe ₂ O ₃	K 7 K 8	R 9 R 10	D 13 D 16

(Note) Mixing Ratio of Waste : Waste / Test Piece in Weight
 * : Weight Including Steel Drum

Table 5 Supplementary Small Size Test for
Survey of Detailed Behavior (1/2)

Test Item	Test No.	Matrix (Pieces)	Environment	Temperature (°C)	Dimension D x H (mm)	Radionuclide Added
Dimension	KC 1	Cement x 6	Sea Water	2	50x80, 60, 40	Cs-137
	KA 1	Asphalt x 6			50x80, 40, 20	Cs-137, Co-60
	RC 1	Cement x 5	Land Water	20	50x80, 40, 30, 20	Cs-137
	RP 1	Plastic x 6			63x64, 48, 32	Cs-137, Co-60
Particle Size	KC 2	Cement x 6	Sea Water	2	10-5, 5-2.5, 2.5-1.2	Cs-137, Co-60
	RC 2	Cement x 4	Land Water	20	20-10, 10-5, 5-2.5, 2.5-1.2	Cs-137, Sr-85, Co-60, Mn-54
Leaching Environment Temperature	RC 4	Cement x 6	Land Water	10, 20, 30, 40	45x44 (IAEA)	Cs-137
	RP 2	Plastic x 6		10, 20, 30	50x50	Cs-137, Co-60
	DC 1	Cement x 4	Soil		45x44 (IAEA)	
	DA 1	Asphalt x 4			50x50	
Water Pressure	DC 2	Cement x 1	Sea Water (0.350, 700 atm.)	2	50x100	Cs-137
	RC 5	Cement x 6	Land Water	20	45x44 (IAEA)	Cs-137, Co-60
	KC 3	Cement x 6	Sea Water	2	45x44 (IAEA)	Cs-137
	RC 3	Cement x 6	Land Water	20		
Waste Ratio	KA 2	Asphalt x 6	Sea Water	2	50x50	Cs-137, Co-60
Admixture Ratio	KA 4	Asphalt x 4	Sea Water	2	50x50	Cs-137, Co-60
Temperature at Preparation	KA 3	Asphalt x 8	Sea Water	2	50x50	Cs-137, Co-60

Table 5 Supplementary Small Size Test for
Survey of Detailed Behavior (2/2)

Test Item	Test No.	Matrix (Pieces)	Environment	Temperature (°C)	Dimension D x H (mm)	Radionuclide Added
Property (Mechanical, Chemical, Microscopic and Others) (Cold Sample)	KCB1	Cement x15	Sea Water	2	100x200	(none)
	KAB1	Asphalt x 8			50x50	
	KPB1	Plastic x 8			45x44 (IAEA)	
	RCB1	Cement x15	Land Water	20	100x200	
	RPB1	Plastic x 8			45x44 (IAEA)	
	DCB1	Cement x 6	Soil	20	100x200	
(Reference Standard)	DAB1	Asphalt x12			50x50	
	DPB1	Plastic x12			45x44 (IAEA)	
	KC 5	Cement x 2	Sea Water	2	50x50	Cs-137, Sr-85, Mn-54
	KA 5	Asphalt x 2				Cs-137, Sr-85, Co-60, Mn-54
	KP 1	Plastic x 2				Cs-137, Sr-90, Co-60

Table 6 Major Items of Actual Size Miscellaneous Waste Forms for LLW

Test Piece Number	Waste Form	Type of Liner	Mortar Filling	Inner Basket	Radionuclide Added to Waste Form (mCi)	Diameter (mm)	Height (mm)	Weight (kg)	Dose Rate (mrad/h)						
									Upper	Side (°)					
										0	90	180	270		
A-1	Simulated Metal Waste (1) Simulated Steel Pipe (2) Content: 54 Pipes (3) Material: Carbon Steel	(Non-Liner)	Filling Mortar Type 2	With Inner Basket Material : Carbon Steel	¹³⁷ Cs 0.79 ⁶⁰ Co 0.36	567	835	636.5	0.3	0.5	0.6	0.9	1.8		
A-2	Simulated Metal Waste (1) Simulated Steel Pipe (2) Content: 38 Pipes (3) Material: Carbon Steel				¹³⁷ Cs 0.49 ⁶⁰ Co 0.51	568	822	580.2	1.2	1.2	1.0	2.2	2.2		
A-3					¹³⁷ Cs 0.49 ⁶⁰ Co 0.51	568	830	603.9	0.9	1.5	4.0	2.0	0.8		
A-4					¹⁴ C 1.02	569	840	602.3	*	*	*	*	*	*	
A-5					¹⁴ C 1.02	569	842	602.3	*	*	*	*	*	*	
B-1	Simulated Metal Waste (1) Simulated Steel Pipe (2) Content: 38 Pipes (3) Material: Carbon Steel	Resin Mortar	Filling Mortar Type 2	(Without Inner Basket)	¹³⁷ Cs 0.49 ⁶⁰ Co 0.51	569	832	566.8	0.9	2.5	2.1	1.2	1.3		
B-2					¹³⁷ Cs 0.49 ⁶⁰ Co 0.51	568	830	561.3	0.2	1.3	2.2	4.0	2.4		
B-3					¹⁴ C 1.02	569	831	577.3	*	*	*	*	*	*	
B-4					¹⁴ C 1.02	568	831	575.3	*	*	*	*	*	*	
B-5		Resin Mortar	Filling Mortar Type 1	(Without Inner Basket)	¹³⁷ Cs 0.53 ⁶⁰ Co 0.50	390	438	127.6	4.0	9.0	8.0	8.4	6.8		
B-6					¹³⁷ Cs 0.53 ⁶⁰ Co 0.50	390	443	135.0	3.8	9.0	5.8	6.7	10.0		
B-7					¹⁴ C 1.21	390	438	134.0	*	*	*	*	*	*	
B-8					¹⁴ C 1.21	390	439	132.6	*	*	*	*	*	*	
B-9			Filling Mortar Type 3		¹³⁷ Cs 0.53 ⁶⁰ Co 0.50	390	435	129.0	4.0	7.0	7.8	9.0	7.6		
B-10					¹³⁷ Cs 0.53 ⁶⁰ Co 0.50	390	438	129.9	3.9	9.4	9.3	8.0	6.2		
B-11					¹⁴ C 1.21	390	436	130.2	*	*	*	*	*	*	
B-12					¹⁴ C 1.21	390	436	131.4	*	*	*	*	*	*	

Table 6 (cont'd)

Test Piece Number	Waste Form	Type of Liner	Mortar Filling	Inner Basket	Radionuclide Added to Waste Form (mCi)	Diameter (mm)	Height (mm)	Weight (kg)	Dose Rate (area/h)						
									Upper	Side (°)					
										0	90	180	270		
B-13	Simulated Metal Waste (Disassembled Steel Pipe) Content: 16 Pipes Material: Carbon Steel	SFPIC	Filling Mortar Type 1	(Without Inner Basket)	¹³⁷ Cs 0.53	390	427	111.4	4.8	7.0	9.4	11.0	14.0		
B-14					⁶⁰ Co 0.50	390	425	112.4	4.6	5.8	12.0	10.0	10.0		
B-15			Filling Mortar Type 3		¹⁴ C 1.21	390	429	126.0	*	*	*	*	*	*	
B-16					¹⁴ C 1.21	390	424	122.2	*	*	*	*	*	*	
B-17					¹³⁷ Cs 0.53 ⁶⁰ Co 0.50	390	424	127.4	4.4	7.8	8.6	6.8	7.8		
B-18	JPDR Metal Waste (Disassembled Steel Pipe) Weight: 150 kg Material: Stainless Steel and Carbon Steel	Resin Mortar SFPIC	Filling Mortar Type 2	(Without Inner Basket)	¹³⁷ Cs 0.53 ⁶⁰ Co 0.50	390	424	127.4	4.8	7.2	6.5	7.8	8.0		
B-19					¹⁴ C 1.21	390	425	132.0	*	*	*	*	*	*	
B-20					¹⁴ C 1.21	390	425	129.0	*	*	*	*	*	*	*
B-21					⁶⁰ Co	570	826	572.4	0.05	0.05	0.07	0.08	0.05		
B-22					⁶⁰ Co 7.41 × 10 ⁻²	570	828	574.2	0.06	0.05	0.06	0.07	0.05		
B-23					⁶⁰ Co	570	831	577.2	0.04	0.05	0.04	0.06	0.06	0.07	
B-24					⁶⁰ Co	570	832	578.6	0.04	0.05	0.15	0.15	0.06		
C-1	Simulated Compacted Waste (Metal Waste in 200 g Drum) Content: 3 Compacted Drums/Drum, 38 Pipes for each drum before compaction Material: Carbon Steel	Resin Mortar SFPIC	Filling Mortar Type 2	(Without Inner Basket)	¹³⁷ Cs 0.79 ⁶⁰ Co 0.36	568	837	726.0	0.3	0.8	1.0	0.3	0.6		
C-2					¹³⁷ Cs 0.79 ⁶⁰ Co 0.36	568	840	731.0	0.2	0.2	0.7	2.0	0.7		
C-3					¹⁴ C 1.52	569	842	732.5	*	*	*	*	*	*	*
C-4					¹⁴ C 1.52	568	840	730.5	*	*	*	*	*	*	*
C-5 (Cold)					Tracer (SrI ₂) 180g (CsI) 180g (KI) 180g	569	841	724.0	—	—	—	—	—		

(Note 1) Solidified piece type 1 : Type of settlement of non-compacted metal pipes as waste into drum without liner placed in metal basket
 (Note 2) Solidified piece type 2 : Type of settlement of compacted metal pipes as waste into drum with liner
 (Note 3) Solidified piece type 3 : Type of settlement of compacted metal waste (compacted drum containing metal pipes) into drum with liner
 (Note 4) Tracer used for test piece number C-5 is non-radioactive dye, "Sea Marker" for maritime use
 (Note 5) SFPIC : Steel Fiber Polymer Impregnated Concrete
 (Note 6) JPDR : Japan Power Demonstration Reactor
 (Note 7) * : Less than detectable limit

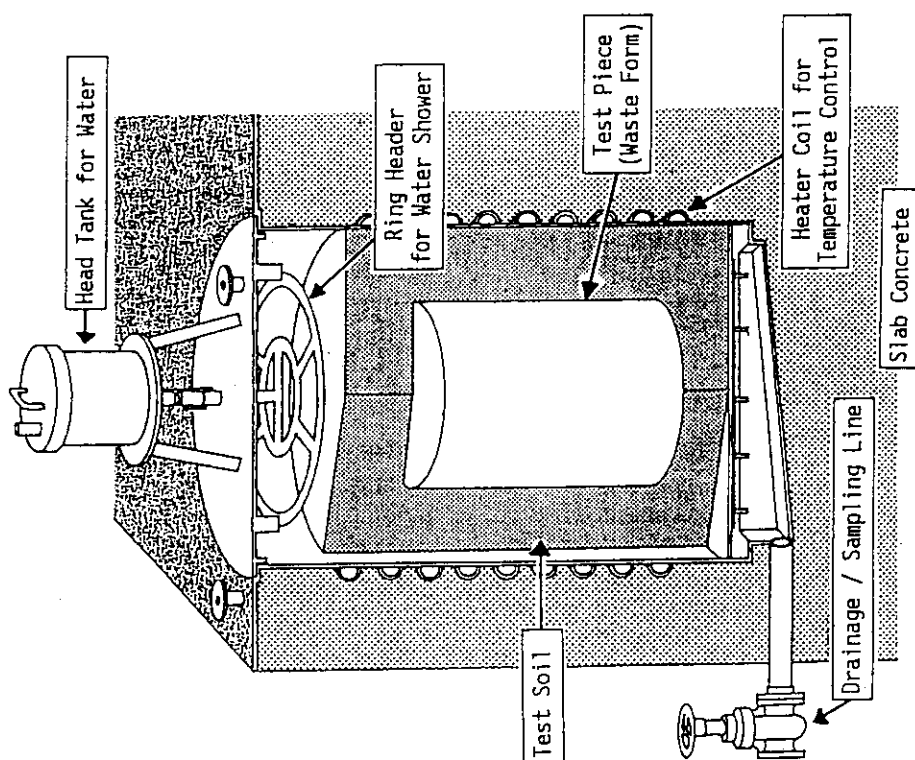


Fig. 2 Outlined structure of test unit for actual size waste in soil

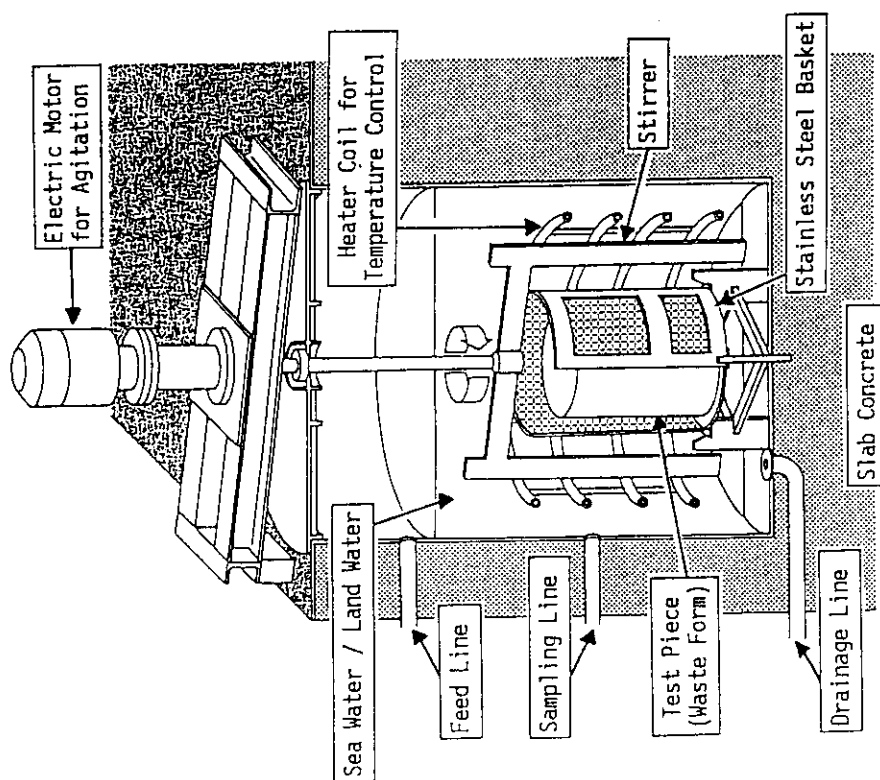


Fig. 1 Outlined structure of test unit for actual size waste in sea water/land water

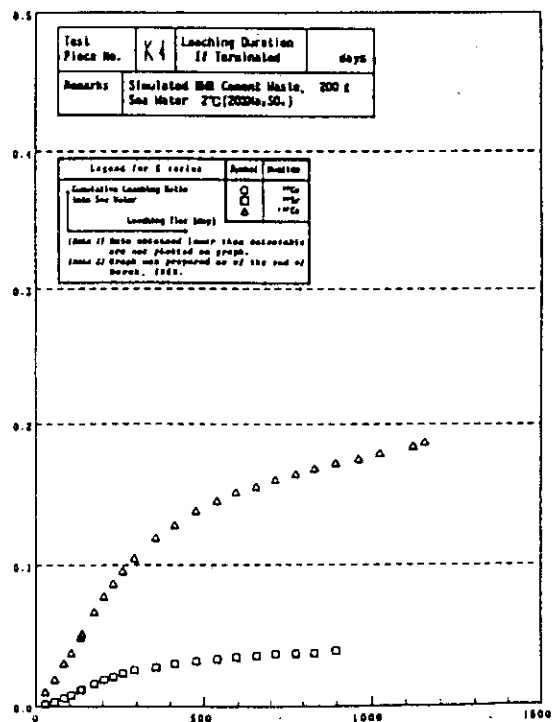
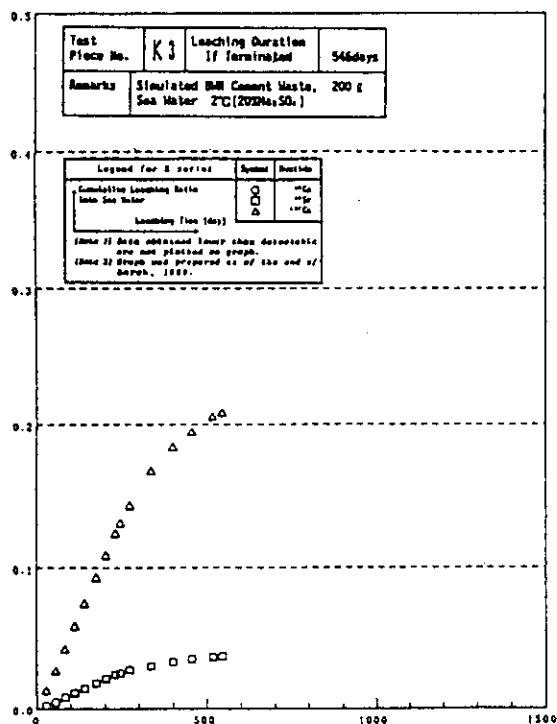
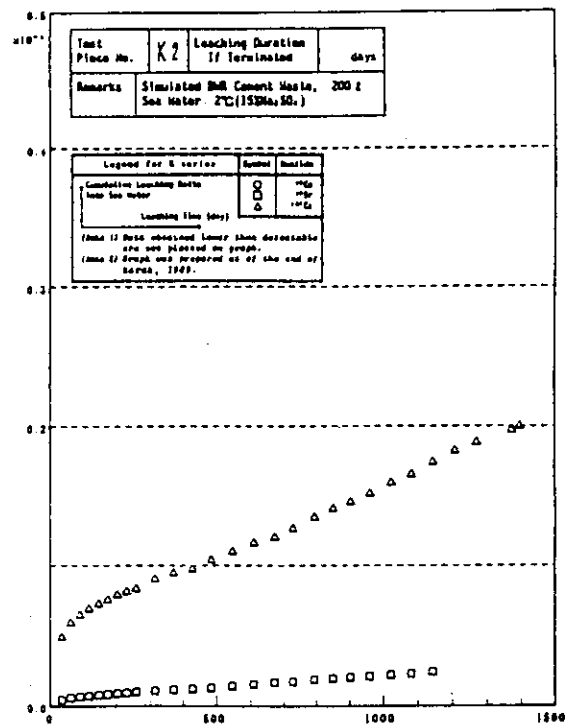
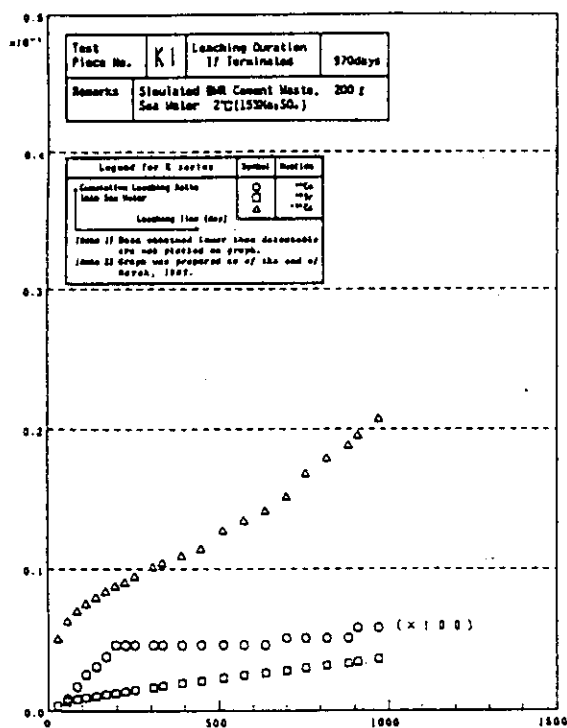


Fig. 3 K-series (Sea Water)

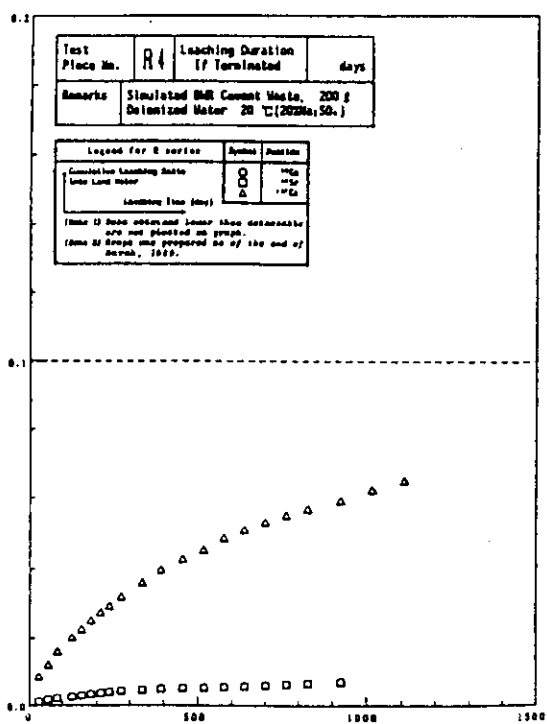
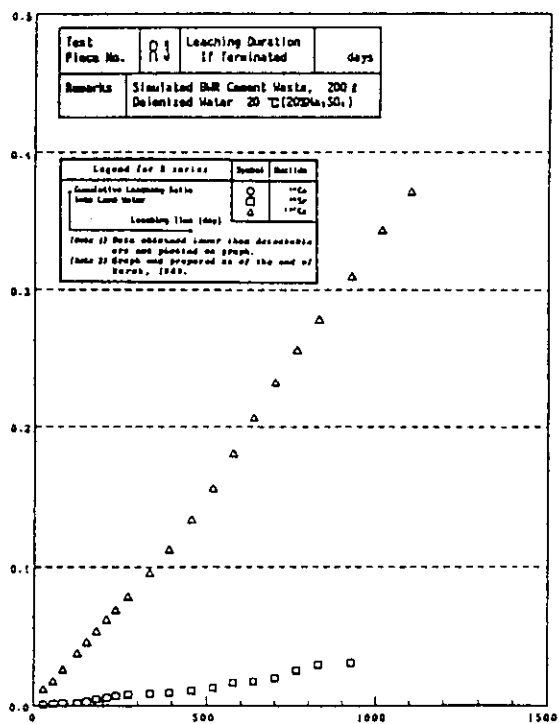
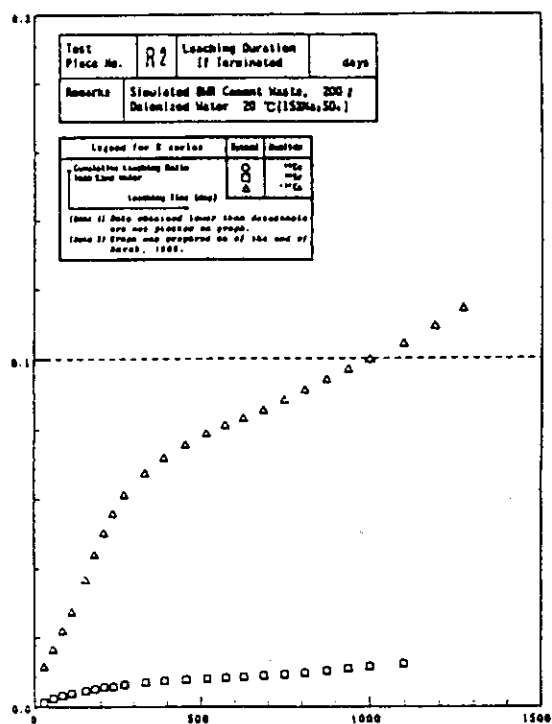
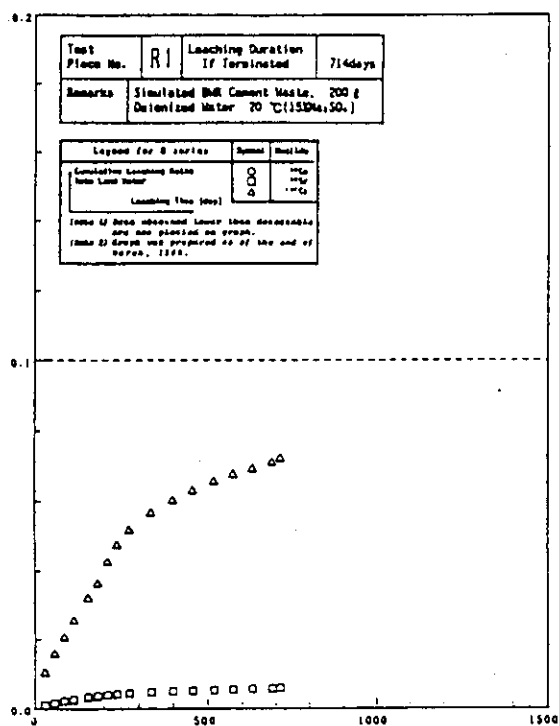


Fig. 4 R-series (Land Water)

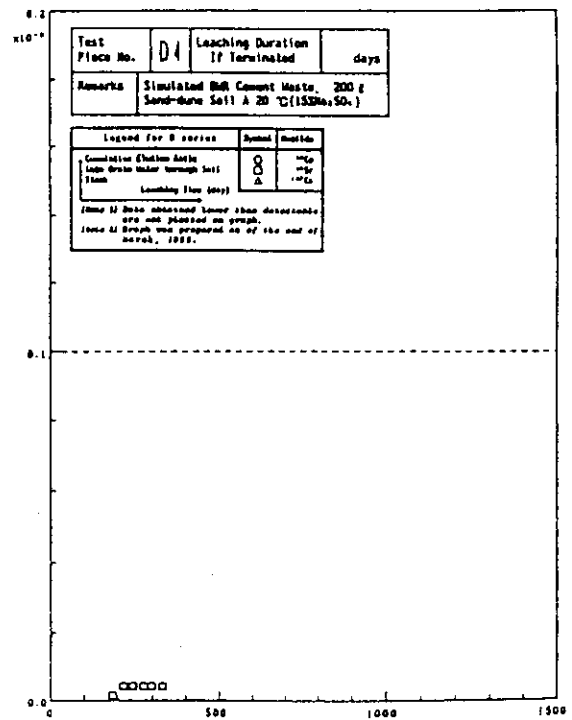
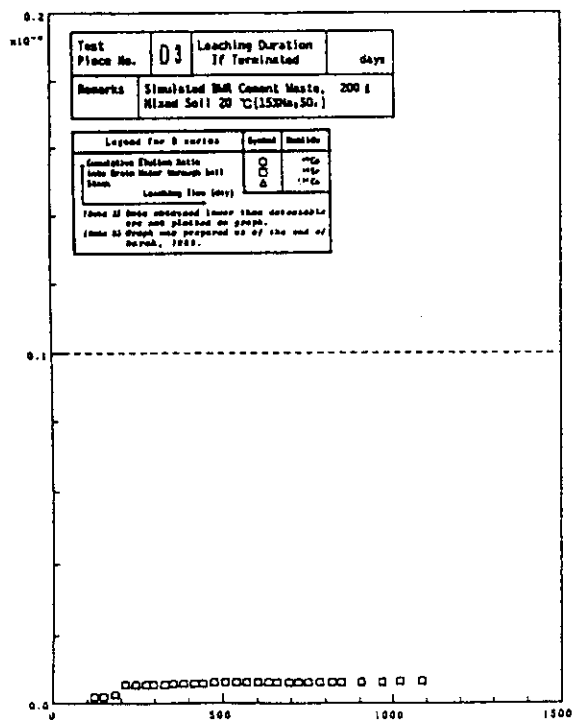
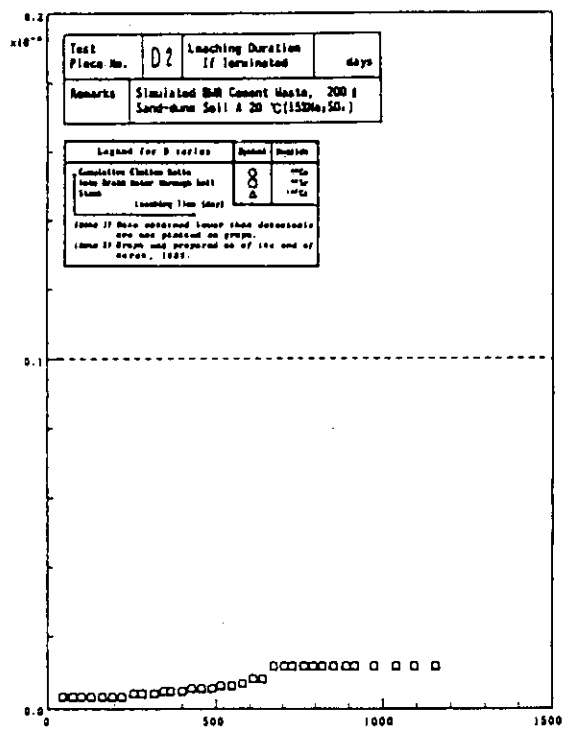
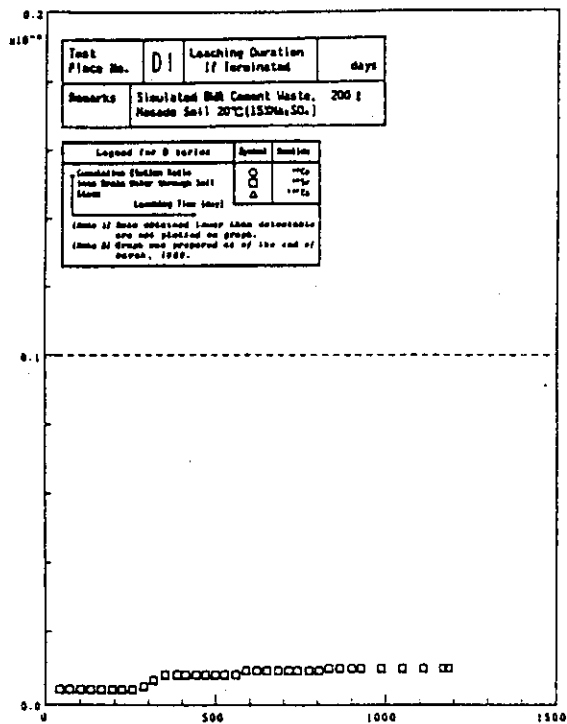


Fig. 5 D-series (Soil)

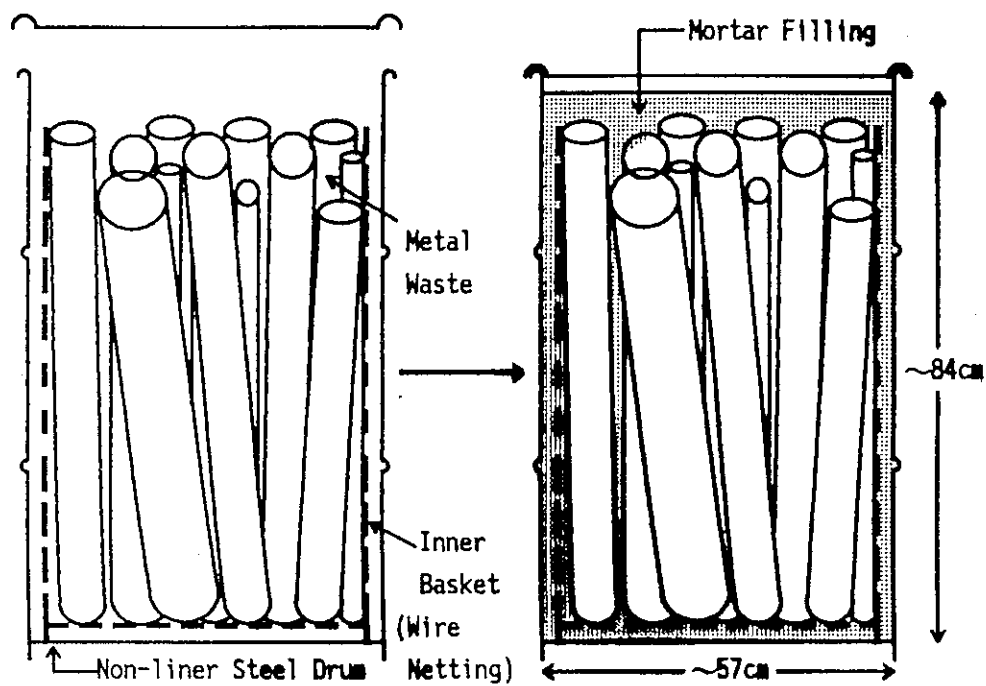


Fig. 6 Type A test piece

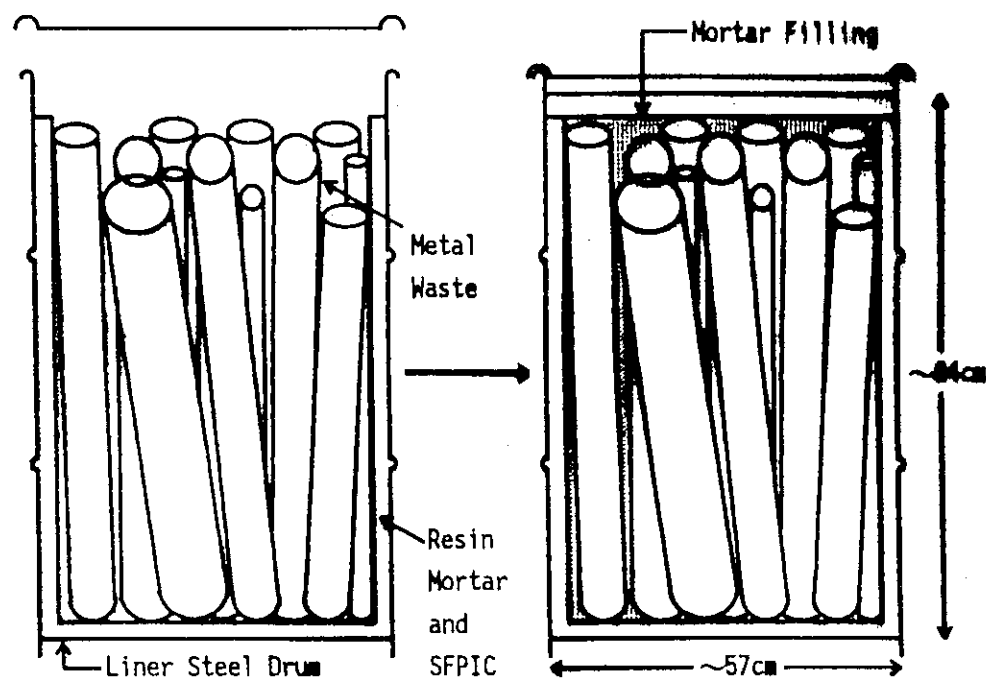


Fig. 7 Type B test piece

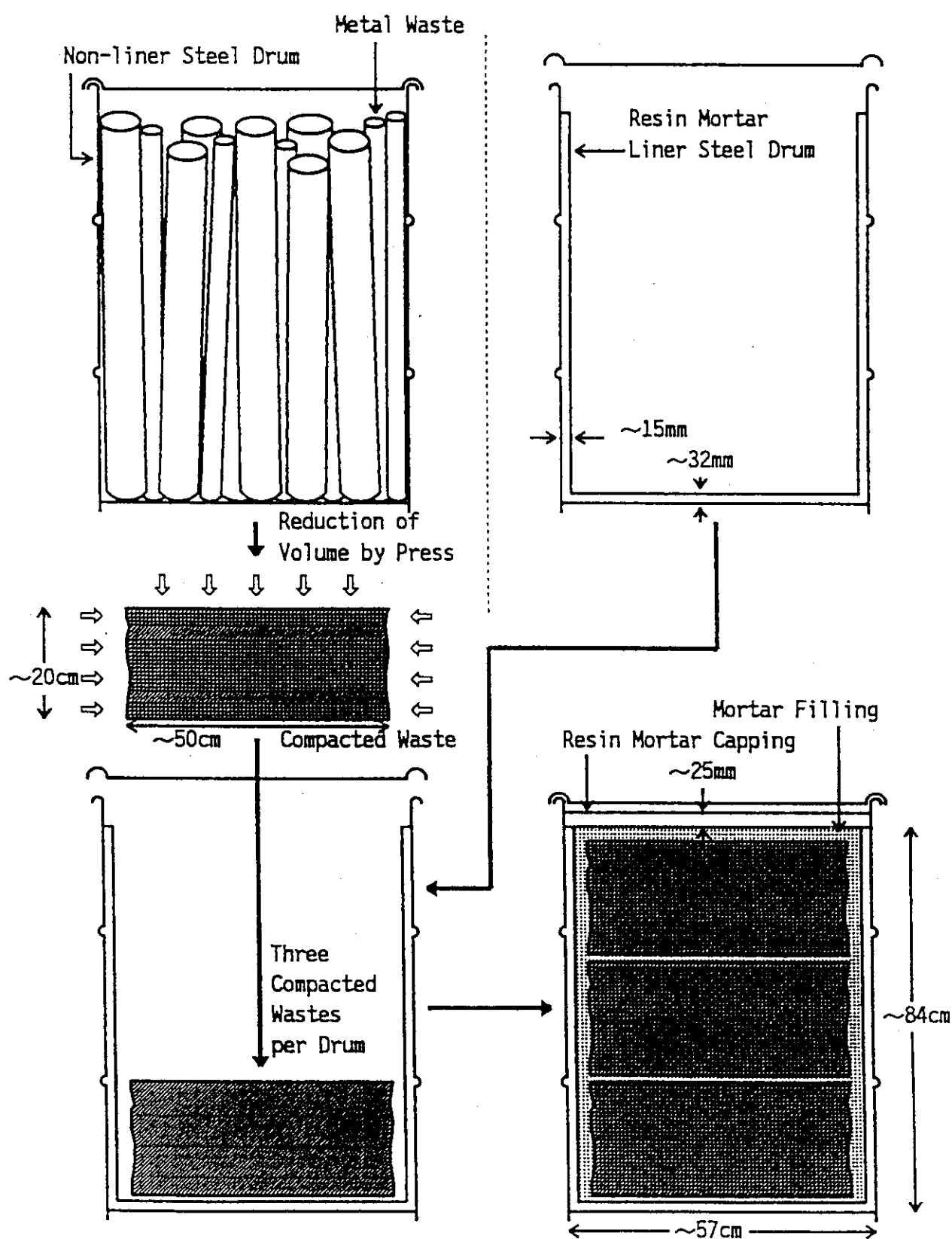


Fig. 8

1.2 Performance of Ceramic Waste Forms

1.2.1 Preparation of Cm-doped Perovskite Material

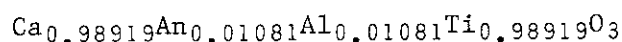
H. Mitamura and K. Matsumoto

1. Introduction

In Synroc, actinide nuclides are to be incorporated in perovskite and zirconolite phases. In the previous studies⁽¹⁾, Synroc was doped with ^{244}Cm (half-life, 18.1 years), and alpha-decay damage effects on Synroc were totally measured. Single phase material is, however, useful for study of its own deterioration due to alpha-decay damage. In the present study, Cm-doped perovskite sample was made to reveal change in its own properties.

2. Experimental Procedure

Figure 1 shows preparation process. Curium source of 0.8165 g was dissolved in 40 g of concentrated nitric acid with 0.1 cm³ of hydrofluoric acid, and then 20 cm³ of 0.1 N nitric acid was added to increase the volume of curium stock solution as larger solution volume decreases loss of the curium source in the subsequent process. This curium stock solution of 0.1 cm³ was collected for alpha radioanalysis of curium-244 concentration. After correction of this quantity, the curium source of 0.8140 g was actually mixed with the precursor material. On 31 March 1993, the curium source included 39 mole% of ^{244}Cm , and 56 mole% of ^{240}Pu that was a daughter nuclide of ^{244}Cm . When actinide nuclides in the curium source are assumed to be trivalent and to be incorporated in the calcium site via an Al^{3+} substitution on a Ti^{4+} site, and excess aluminum is supposed to become alumina, the present nominal composition of the slurry mixture should make the following perovskite material:



together with 0.02 wt% of alumina. This amount of alumina formation would be practically negligible.

The pH of slurry mixture was adjusted to be 9 with ammonium hydrox-

ide. After the slurry mixture was poured into an in-cell calciner pot, it was dried at 80°C in a stream of N₂ gas, and then calcined at 750°C for 2 hours in a stream of Ar-4%H₂ gas. The calcined powder of 36.7089 g was collected from the calciner pot with a spatula. The recovery of this powder was 97%. The calcined powder (22.2574 g) was poured into a graduated polyethylene cylinder to measure the pour density. The cylinder was then tapped (~3-cm drops) until no further change in powder volume was observed (300 taps).

The calcined powder was divided into three portions of 12.2616, 12.2462, and 12.2432 g. Each portion was hot-pressed using a graphite die at 1250°C and 29MPa for 2 hours in a stream of N₂ gas. Three as-cast cylinder samples weighed 12.1002, 12.0930, and 12.0760 g, respectively. This means that the calcined powder showed 1.3-1.4% of weight loss during hot-pressing. Decay heat of each as-cast cylinder sample was measured using a twin-type conduction calorimeter.

After the periphery of each cylinder sample was polished with No. 600 grit abrasive paper, its flat faces were lapped with 6-micron diamond paste. Densities of the polished cylinder samples were measured by water displacement method. The water was kept at 30°C.

3. Results and Discussion

Pour and tap densities of the calcined products were 0.53 and 1.09 g.cm⁻³. Since the powder surface in the polyethylene cylinder was wavy, the surface was roughly averaged by eye estimation in reading the volume scale.

Densities of polished cylinder samples were 4.084, 4.085 and 4.081 g.cm⁻³ one month after hot pressing (Table 1). In that one month, these samples had a cumulative dose of 7×10^{16} alpha decays.g⁻¹. The average density of the three cylinder samples is 4.083 g.cm⁻³. As the amount of scatter of the three densities is <0.05% of the mean, the reproducibility of hot pressing is considered to be acceptable.

The three as-cast cylinders generated the decay heat of 0.251, 0.252 and 0.244 W. If the heat generation is assumed to be due to the alpha decay of ²⁴⁴Cm alone (a Q value of 5.902 MeV), the average decay heat of the cylinder samples corresponds to specific alpha activity of 21.88 GBq.g⁻¹ (0.5914 Ci.g⁻¹) on 31 March 1993. This value is smaller than the

specific alpha activity calculated from mass assay by 2.3%. On the other hand, the ^{244}Cm activity of the curium stock solution was 0.904 TBq (24.42 Ci) if it was assumed that specific gravity of the curium stock solution was the same as that of 41 wt% of nitric acid (1.25 g.cm^{-3}), which was estimated from the weight ratio of concentrated and 0.1 N nitric acids added in dissolution of the curium source. This ^{244}Cm activity is higher than the value calculated from mass assay by 6.5%. Both the activities obtained from the calorimetry and the alpha radioanalysis were similar to the value calculated from mass assay. Therefore, the value of 22.40 GBq.g^{-1} (0.6053 Ci.g^{-1}) and 22.29 GBq.g^{-1} (0.6024 Ci.g^{-1}) on 31 March 1993, which was deduced from the mass assay, was adopted as the specific alpha and ^{244}Cm activities of the hot-pressed material, respectively. This latter specific activity was used for calculation of cumulative alpha decays in the present samples as 99.5 % of alpha activity comes from ^{244}Cm .

4. Conclusion

Curium-doped perovskite slurry, which had the nominal composition of $\text{Ca}_{0.98919}\text{An}_{0.01081}\text{Al}_{0.01081}\text{Ti}_{0.98919}\text{O}_3$, was calcined at 750°C for 2 hours in a stream of Ar-4% H_2 gas. Calcined powder had pour and tap densities of 0.53 and 1.09 g.cm^{-3} . This powder showed 1.3-1.4% of weight loss during hot-pressing at 1250°C and 29MPa for 2 hours. The hot-pressed cylinder samples had the specific ^{244}Cm activity of 22.3 GBq.g^{-1} on 31 March 1993. After these samples got a cumulative dose of 7×10^{16} , their density was 4.083 g.cm^{-3} . The polished samples will be cut in the near future to make leaching and XRD specimens.

Reference

- (1) H. Mitamura, S. Matsumoto, K.P. Hart, T. Miyazaki, E.R. Vance, Y. Tamura, Y. Togashi, and T.J. White, "Aging Effects on Curium-Doped Titanate Ceramic Containing Sodium-Bearing High-Level Nuclear Waste", J. Am. Ceram. Soc., 75[2], 392-400 (1992).

Table 1 Density of Cm-doped Perovskite Cylinder Samples

Sample No.	Density (g/cm ³)	Sigma (g/cm ³)
93001	4.084	0.002
93002	4.085	0.004
93003	4.081	0.002
Average	4.083	
Sigma	0.002	

Measurement was carried out about one month after hot-pressing.

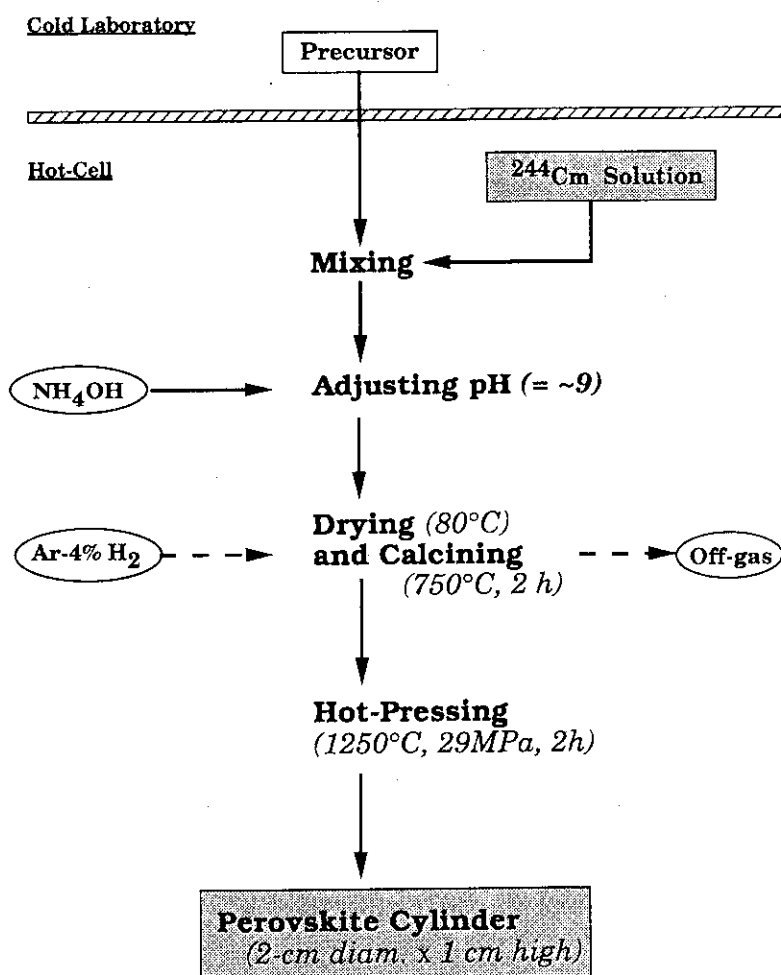


Fig. 1 Preparation process for curium-doped perovskite

1.2.2 Durability of an $\text{La}_2\text{Zr}_2\text{O}_7$ Waste Form Containing Various Amounts of Simulated HLW Elements

I. Hayakawa and H. Kamizono

1. Introduction

In our studies⁽¹⁻³⁾, $\text{La}_2\text{Zr}_2\text{O}_7$ is found to be a superior host for nuclear waste elements. The actinide and lanthanide elements are assumed to occupy the La sites of $\text{La}_2\text{Zr}_2\text{O}_7$ because their ionic radii are close to that of La^{3+} .

Leachability of waste elements confined in $\text{La}_2\text{Zr}_2\text{O}_7$ is generally presumed to depend on the intrinsic chemical reactivity of the waste elements, the matrix crystal structure and the coordination number to oxygen. It is considered that the formation of solid solution of waste elements affects the leachability of La and Zr because the addition of waste elements alters the metal-oxygen bond lengths and the vacancy concentration in the $\text{La}_2\text{Zr}_2\text{O}_7$ waste form.

In the present work, the effects of simulated HLW constituents on the leach rates of the $\text{La}_2\text{Zr}_2\text{O}_7$ waste form are examined in three kinds of solutions with different pH values. Ce, Nd and Sr were used as simulated constituents for various kinds of actinide, lanthanide and alkaline earth metal elements.

2. Experimental

The nitrates of La, Zr, Nd, Ce and Sr were mixed and dissolved in 0.5 M HNO_3 solution and calcined at 700°C in air. The calcined powder was ground in an Al_2O_3 mortar and pressed into pellets of 20 mm in diameter under a pressure of 500 kg/cm^2 . Preliminary experiments revealed that enhanced reaction and crystal growth occurred at 1400°C . Therefore the firing temperature was fixed at 1400°C . The pellets fired at 1400°C for 16 hr in air were ground in an Al_2O_3 mortar, pressed into pellets, and refired at 1400°C for 16 hr in air. The refired product was ground to powders in an Al_2O_3 mortar and used for measuring the lattice parameters and leach rates.

3. Results

3.1 Leaching Behavior in HCl Solution

Figure 1(A) shows the change of the lattice parameters in the system $\text{La}_2\text{Zr}_2\text{O}_7$ - $\text{Nd}_2\text{Zr}_2\text{O}_7$. Only a pyrochlore phase appears in this system. The lattice parameter of the pyrochlore phase decreases in proportion to the decrease of Nd. It is thought that Nd tends to be substituted for La in the solid solution, because the ionic radius of Nd^{3+} is smaller than that of La^{3+} and is larger than that of Zr^{4+} . Figure 1(B) shows that the leach rates of La and Nd decrease with the increase of Nd mol%. When a small amount of Nd is added to $\text{La}_2\text{Zr}_2\text{O}_7$, the leach rate is greatly reduced. In contrast to this, when a small amount of La is added to $\text{Nd}_2\text{Zr}_2\text{O}_7$, the change of leach rate is negligible. The leach rate of Zr was almost constant at about $2 \times 10^{-6} \text{ g m}^{-2}\text{d}^{-1}$ in this system. The same kind of phenomenon was also observed in the systems $\text{La}_2\text{Zr}_2\text{O}_7$ - $2\text{CeO}_2\cdot 2\text{ZrO}_2$ and $\text{La}_2\text{Zr}_2\text{O}_7$ - $2(\text{CeO}_2\cdot\text{SrO})\cdot 2\text{ZrO}_2$.

3.2 Leaching Behavior in Deionized Water and in NaOH Solution

Figure 2 shows the leach rates of La, Nd and Zr in deionized water in the system $\text{La}_2\text{Zr}_2\text{O}_7$ - $\text{Nd}_2\text{Zr}_2\text{O}_7$. The leach rate of La slightly increases with the increase of Nd in the deionized water, although it decreases in the HCl solution. The leach rate of Nd once decreases with the increase of La and then slightly increases. The leach rates of Nd and La in the deionized water are smaller than those in the HCl solution, but the difference was within one order of magnitude. The leach rate of Zr is almost constant as observed in the HCl solution and is smaller than that in the HCl solution by 1-2 orders of magnitude. In the NaOH solution, the leach rates of La and Nd were $1-3 \times 10^{-7} \text{ g m}^{-2}\text{d}^{-1}$ and were smaller than those in the deionized water by 2 orders of magnitude. The leach rates of Zr were smaller than those in the deionized water by one order of magnitude.

4. Discussion

The effect of the chemical composition on the leach rates of each constituent, La, Nd, Ce and Sr, is clearly observed in the HCl solution

in our work. In the HCl solution of a pH=1, all constituents dissolve as ions simultaneously. Hence, the dissolution of the waste elements depends on the dissolution of the matrix crystal lattice. On the other hand, in the deionized water, Zr, La, Nd and Ce ions in the crystal structure are hydrolyzed by water, and the insoluble hydroxides or carbonates are formed on the surface of the waste form. Since the hydroxides or carbonates retard the dissolution, the effect of the crystal structure on the leach rates of each constituent is not clearly observed in deionized water.

Figure 3 shows the relationship between the leach rate of the metal ions confined in $\text{La}_2\text{Zr}_2\text{O}_7$ and the metal-oxygen(M-O) bond energies. This figure also shows the relationship between the M-O bond energy and the ionicity of M-O bond which is conveniently expressed by the difference between the electronegativities of the metal and oxygen atoms (The figures in parentheses show the coordination numbers to oxygen). The more the difference of electronegativities between metal and oxygen becomes, the less its covalency is. The leach rates of constituents tend to decrease with increasing bond energy. Generally leachable alkali metal elements have a low metal-oxygen bond energy of about 15 kcal/mol. In contrast, Al, Ti and Zr which form insoluble oxides have higher M-O bond energies. As for these elements, the element with higher M-O bond energy tends to have stronger covalency. Hence, the leach rate of some metal may be affected by both M-O bond energy and its covalency. In our experiments, the leaching behavior of La, Nd and Ce in the solid solution range is considered to be mainly a function of the M-O bond energy alone because the electronegativities of La, Nd and Ce are almost the same.

5. Conclusion

In HCl solution of a pH=1, the leach rate of La from the pyrochlore phase in the system $\text{La}_2\text{Zr}_2\text{O}_7\text{-Nd}_2\text{Zr}_2\text{O}_7$ decreased as the ratio of $\text{Nd}_2\text{Zr}_2\text{O}_7$ in this system increased from 0 to 100 mol%. In the system $\text{La}_2\text{Zr}_2\text{O}_7\text{-2CeO}_2\text{2ZrO}_2$, the leach rate of La from the pyrochlore phase decreased as observed in the system $\text{La}_2\text{Zr}_2\text{O}_7\text{-Nd}_2\text{Zr}_2\text{O}_7$, although the solid solution range of Ce in this phase was limited up to 27 mol% $2\text{CeO}_2\text{2ZrO}_2$.

In deionized water of a pH=5.6 and NaOH solution of a pH=10, however,

such a compositional effect on leach rates was not observed because of the formation of hydroxides or carbonates on the surface of the solid.

References

- (1) H. Kamizono, I. Hayakawa and S. Muraoka, J. Am. Ceram. Soc., 74, 863 (1991).
- (2) I. Hayakawa and H. Kamizono, presented at XV International Symposium on the Scientific Basis for Nuclear Waste Management, Strasbourg, Nov. 4-7, 1991.
- (3) I. Hayakawa and H. Kamizono, J. Nucl. Mater., 202, 163 (1993).

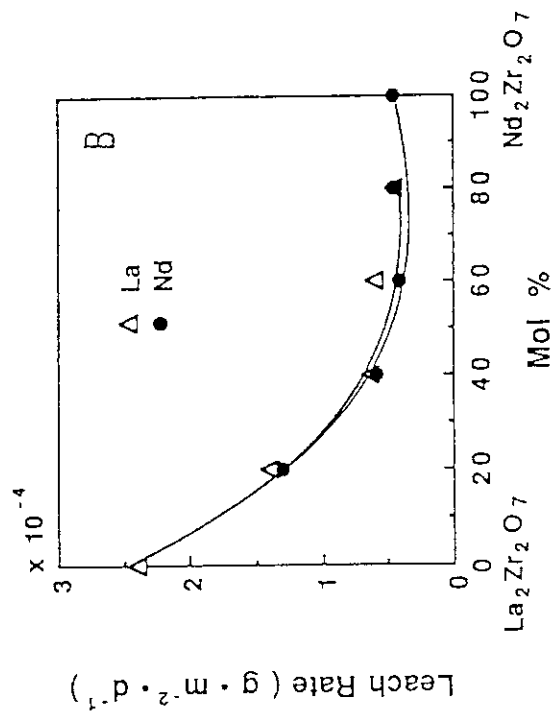
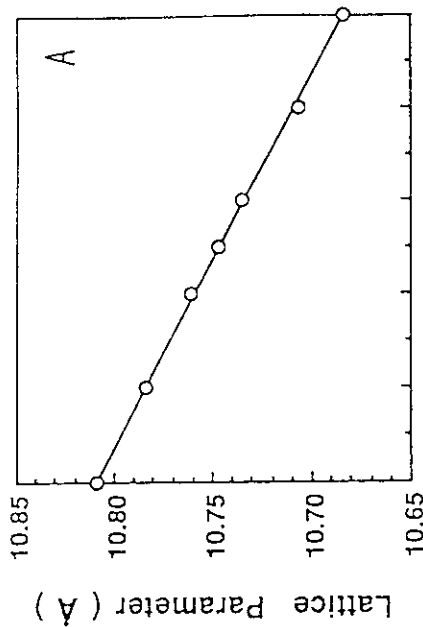


Fig. 1 Lattice parameters of a pyrochlore structure (a) and leach rates of La and Nd in HCl solution of pH=1 at 90°C (b), in the system $\text{La}_2\text{Zr}_2\text{O}_7\text{-Nd}_2\text{Zr}_2\text{O}_7$.

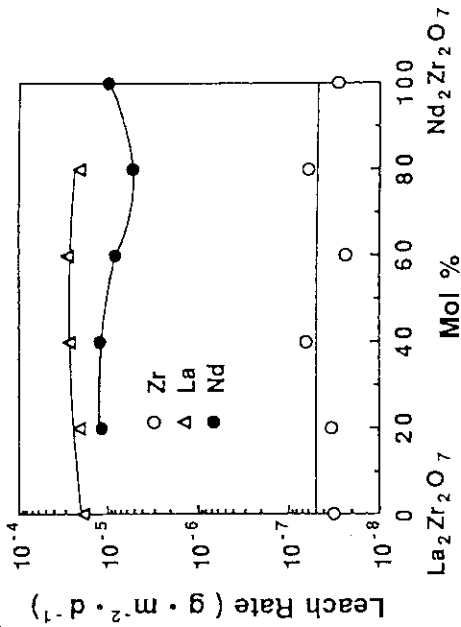


Fig. 2 Leach rates of Zr, La and Nd in deionized water at 90°C in the system $\text{La}_2\text{Zr}_2\text{O}_7\text{-Nd}_2\text{Zr}_2\text{O}_7$.

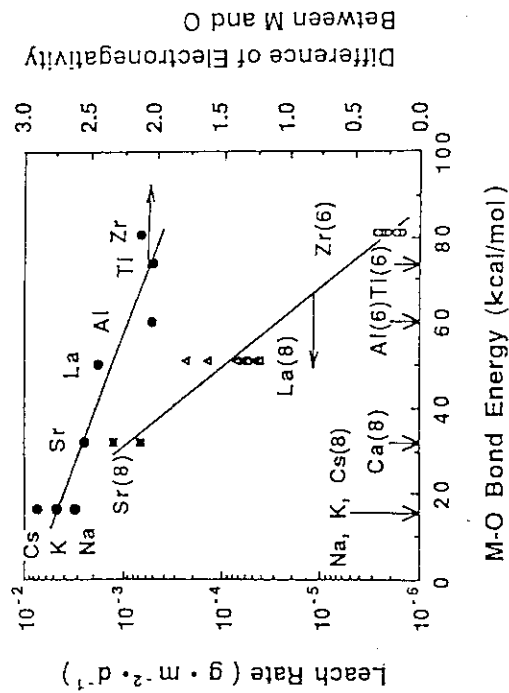


Fig. 3 Relationship between M-O bond energy and leach rate or difference between electronegativities of M and O. The coordination numbers of oxygen around the metal are given in the parentheses.

1.2.3 8 mol% Yttria-Stabilized Zirconia (YSZ) and Alumina-based Ceramic Waste Forms Containing Ce and Nd

K. Kuramoto

1. Introduction

This report is a fundamental study for the development of a new ceramic waste form to immobilize the selected elements such as actinides with TRU and lanthanides with long half lives. Yttria-stabilized zirconia (YSZ) with fluorite type structure and alumina based ceramics were selected as matrix¹⁻³). Ce and Nd were used as the simulated wastes, which substituted for radioactive TRU and represented other lanthanide elements. The properties of samples sintered at 1400°C in air or at 1500°C in reduced atmosphere were investigated with emphasis upon X-ray diffractometer (XRD) and scanning electron microscope (SEM). The accelerated leach tests were carried out using crushed powder samples in nitric acid solution and in deionized water at 150°C for designed periods. The relation between the leach rates and the crystalline phases is discussed.

A. Examination Using YSZ

A.2 Experimental procedure

TZ-8Y ($\text{Zr}_{0.86}\text{Y}_{0.14}\text{O}_{1.93}$), the commercial sub-micron powder of YSZ and designed amounts of CeO_2 and Nd_2O_3 powders were mixed simultaneously in a ball-mill, pelletized uniaxially at 360 kg/cm², and sintered at 1400°C for 80 hr and cooled in air. On the other side, TZ-8Y and designed amounts of $\text{Ce}(\text{NO}_3)_3$ or $\text{Nd}(\text{NO}_3)_3$ solution were mixed individually, and denitrated. Using the same technique, the pellet samples were sintered at 1400°C for 16 hr and cooled in air. The powder samples adjusted under 75 μm in size were used for the leachability and XRD measurements.

XRD measurements were carried out to identify the crystalline phases, to evaluate accurate lattice parameters of fluorite type structure and to investigate macro strain caused by dissolution with nitric acid solution. Si was used as the internal standard.

Density measurements were carried out using pellet samples contain-

ing only Ce or Nd. The bulk densities in g/cm^3 were compared with the theoretical densities⁴⁾ in g/cm^3 . SEM observations were carried out to measure the average grain size of a YSZ pellet and to observe the grain boundary using electron probe micro analyzer (EPMA).

The accelerated leach tests were carried out at 150°C for 3, 7, 16 and 34 days in nitric acid solution of pH 1. In these tests, the acid was used as the leachate to accelerate the leaching behavior and to remove the effect of segregated layers on the concentrations of leachates, such as hydroxides and carbonates⁵⁾. As to remove the effect of the dependence on each sample, the same powder samples were used through the time schedule of leach tests in accordance with the technique of MCC-2⁶⁾. The samples in the acid were heated in an oven at 150°C for 3 days. After that, the leachate and the powders were separated by the ultra-filtration. The powders were washed and again put into a teflon crucible with fresh nitric acid solution, and heated at 150°C for next 4 days. The leach tests for following 9 and 18 days were also carried out using the same technique. Finally, the powders were dried in an vacuum desiccator, and measured the macro strain by XRD. On the other side, the concentration of the leachates were analyzed by an inductively coupled plasma atomic emission spectroscopy (ICP) (Seiko Co. Ltd.). The leach rates (Lr_i , in $\text{g/cm}^2\cdot\text{day}$) for the element i were given by the following equation (1).

$$Lr_i = A_i \cdot V / (F_i \cdot SA \cdot T) \quad (1)$$

Where A_i is the concentration of the element i in the leachate, V is the volume of the leachate, F_i is mass fraction of the element i in the sample, SA is the initial surface area of the sample and T is the leaching time.

A.3 Results and Discussion

A.3.1 XRD measurements

For the samples containing only Ce, fluorite type structure was stable in the region from 0 to 48.1 mol% of Ce. For the samples containing only Nd, fluorite type structure was stable in the region from 0 to 19.4 mol% of Nd. The fluorite type structure was stable in all samples containing Ce and Nd simultaneously from 4.7 to 24.1 mol% in Ce and Nd, respectively.

Figure A-1 shows the observed lattice parameters of fluorite type structure for the samples containing only Ce or Nd, respectively. Each lattice parameter ($A_{\text{Ceobs.}}$ and $A_{\text{Ndobs.}}$, in nm) increased linearly with Ce or Nd contents according to the equations (2) and (3).

$$A_{\text{Ceobs.}} = 0.51391 + 0.00029 \times C \quad (2)$$

$$A_{\text{Ndobs.}} = 0.51385 + 0.00040 \times N \quad (3)$$

Where C or N is the contents of Ce or Nd in mol%, respectively. It is recognized that the gradient of the lattice parameter for Ce is smaller than that for Nd. These results were compared with the theoretical ones⁴⁾. Based on the results of Catlow et al.⁷⁾ and Uehara et al.⁸⁾, it was adopted in the theoretical equation that Zr^{4+} and Ce^{4+} selectively occupy in the sites of four nearest-neighbors of an oxygen vacancy, where these elements turn into 7-coordination⁹⁾. For O^{2-} , or Y^{3+} and Nd^{3+} , the value of ionic radii of 4- or 8-coordination were also adopted. Judging from the results in good agreements with those lattice parameters as shown in Fig. A-2, it is confirmed on the points of lattice parameters that some of Zr^{4+} and Ce^{4+} ions exist in the selective cation sites. Nd^{3+} , Y^{3+} and the other tetra-valent ions with 8-coordination, on the other side, dispersed in the other sites in YSZ.

A.3.2 SEM observations and density measurements

From the results of EPMA, all elements were recognized to be dispersed homogeneously, and no grain boundaries were observed. The average grain size was about 8.7 μm in diameter for the sample of TZ-8Y. It was cleared that the grains grew considerably during sintering.

The samples containing only Ce have little open pores and a good sinterability, especially up to 96.7% of relative density. The samples containing only Nd had low sinterability as the contents of Nd increased. This will be due to the hard particles of Nd_2O_3 which made up during calcination and remained even after the ball mill crushing.

A.3.3 Leachability

From the results of the time dependence of leach rates, it was revealed that leach rates for initial periods showed quite large values. This will be the reason that the parts with high activation energy dissolve selectively into leachates.

Figure A-2 shows the leach rates of 16-34 days in nitric acid solution at 150°C of each element. For the samples containing only Ce, Lr_{Ce}

and Lr_Y decreased as the contents of Ce increased. The minimum value of Lr_{Ce} or Lr_Y was 3.4×10^{-9} g/cm²·day and 1.1×10^{-8} g/cm²·day, respectively. On the contrary, for the samples containing only Nd, Lr_{Nd} and Lr_Y increased as the contents of Nd increased. For the samples containing Ce and Nd simultaneously, each leach rate became similar values of $2-4 \times 10^{-8}$ g/cm²·day in the case that the sum of Ce and Nd were under 20 mol%. A tendency was revealed that Lr_{Ce} in 9C-9N increased threefold than that in 11C with similar contents for Ce, and Lr_{Nd} in 9C-9N decreased one-fifth than that in 10N. In the case that the sum of Ce and Nd were 28.5 mol%, each leach rate increased linearly as Ce were replaced by Nd. The same tendency was observed, in words, Lr_{Nd} and Lr_Y decreased as the contents of Ce increased such as in 19N, 10C-19N and up to 24C-24N. These tendencies will be due to the decrease of Ce-O distance with lower bonding energy and the increase of Nd-O distance with higher bonding energy surrounding oxygen vacancies.

A new secondary phase was identified in the after leached sample of 19N. For 10N and 19N, decreases of about 0.05% of lattice parameters were also observed. It is considerable that the selective dissolution of Nd and Y cause the breadth of the full widths at half maximum (FWHMs), further the creation of the secondary phase. No obvious change of FWHMs and lattice parameters were observed in the other samples.

A.4 Conclusion

The following results were obtained through these experiments.

- (1) Fluorite type structure was stable in the range of $0 < Ce < 48.2$ or $0 < Nd < 19.4$ in mol% at 1400°C for 16 hr, and in the range of $4.7 < Ce, Nd < 24.1$ in mol% at 1400°C for 80 hr.
- (2) No grain boundary was identified and each element was distributed homogeneously in YSZ samples. The average grain size of TZ-8Y was 8.7 μ m in diameter after a sintering at 1400°C for 16 hr in air. A high dense pellet sample of 96.7% could be made.
- (3) For leach tests in nitric acid solution at 150°C, Lr_{Ce} decrease as the contents of Ce increased up to 3.4×10^{-9} g/cm²·day. Lr_{Nd} and Lr_Y increased as the contents of Nd increased in the samples containing only Nd. Lr_{Ce} , Lr_{Nd} and Lr_Y turned into the similar values of $2 - 4 \times 10^{-8}$ g/cm²·day in the samples containing Ce and Nd simultaneously. Because of the change of Ce-O or Nd-O distance, Lr_{Ce} or Lr_{Nd} increased threefold or decreased one-fifth, respectively.

B. Examination Using Alumina Based Ceramics

B.2 Experimental Procedure

Table B-1 (A) shows the composition of the samples used in this experiments. The sub-micron α -alumina powder, designed amounts of Ce and Nd nitric solution and silica ethoxide were mixed and calcined at 250°C. After pelletized at 360 kg/cm², the pellets were sintered at 1500°C for 25 hr in 3%H₂ + Ar reduced atmosphere. XRD measurements were carried out to identify crystalline phases. The densities were measured using pellet samples. The accelerating leach tests were carried out at 150°C for 3, 7, 14 and 28 days in nitric acid solution of pH 1 and in deionized water.

B.3 Results and Discussion

B.3.1 Formation of crystalline phases

Magnetoplumbite [CeAl₁₁O₁₈] (M) phase and a little amounts of α -Al₂O₃ (α) were observed in ACS, and perovskite [NdAlO₃] (P) and α phase were detected in ANS as shown in Fig. B-1. In ACNS-1 and ACNS-2, these three phases co-existed. Judging from the change of lattice parameters as shown in Table B-1 (B), it was cleared that Ce was included in M and P phases and Nd was only in P phase.

Table B-1 (C) and (D) show the relative amounts of the phases and the apparent densities of each sample, respectively. It was cleared that the sample density tended to increase with the exchange of Ce for Nd. Judging from these results, the restraint of formations of M phase is required to make high dense alumina ceramics forms under the condition used in this experiment.

B.3.2 Leachability in nitric acid solution and in deionized water

Leach rates of each element in the acid at 150°C are listed in Table B-1 (E). L_{rAl} , L_{rCe} and L_{rNd} in the water were lower than 10⁻⁷ g/cm²·day, while in the acid, they were of the order of 10⁻⁶ g/cm²·day. However no measurable peaks from P phase was detected, except faint traces in ANS, M phase showed little changes in peak intensity after leaching in the acid. This indicates that P phase is more prone to leaching in the acid than M phase.

Leach rates in the water were fairly low compared with that of the currently investigated borosilicate waste glasses, especially those for

Al and Ce were such as less than detection limits in this work. Lr_{Nd} was influenced to some extent by the P phase contents of ceramics, as in Table B-1 (F), but still kept below nearly 10^{-7} g/cm²·day. This suggests P phase is practically not a serious problem in the dissolution of ceramics in water. Given the fact further that the pH of natural groundwater ranges from 6 to 9, it can be concluded that the alumina-based ceramics consolidating some rare earth oxides have crystalline phases with sufficient chemical durability in candidate repository environments.

B.4 Conclusion

The following results were obtained through these experiments for alumina based ceramics accommodating some rare earth oxides.

- (1) For making ceramic waste forms with higher density, it seems important to suppress the formation of magnetoplumbite phases.
- (2) Perovskite (REAlO_3) are more prone to leaching in an acid solution than the magnetoplumbite phases.
- (3) Leachability of samples in water is low enough for incorporating some rare earth oxides into alumina matrix.

References

- 1) K. Kuramoto et al., JAERI-M 91-097.
- 2) T. Muromura and Y. Hinatsu, J. Nucl. Mater., 137, 227(1986).
- 3) T. Muromura and Y. Hinatsu, J. Nucl. Mater., 151, 52(1987).
- 4) R.P. Ingel and Lewis III, J. Am. Ceram. Soc., 69, 325(1986).
- 5) D.G. Brookins, "Eh-pH Diagrams for Geochemistry", Springer-Verlag, 1988.
- 6) D.M. Strachan et al., "Scientific basis for nuclear waste management", Vol.21, 424(1980).
- 7) C.R.A. Catlow et al., 69, 272(1986).
- 8) T. Uehara et al., Solid State Ionics, 23 331(1987).
- 9) R.D. Shannon, Acta. Cryst., A32, 751(1976).

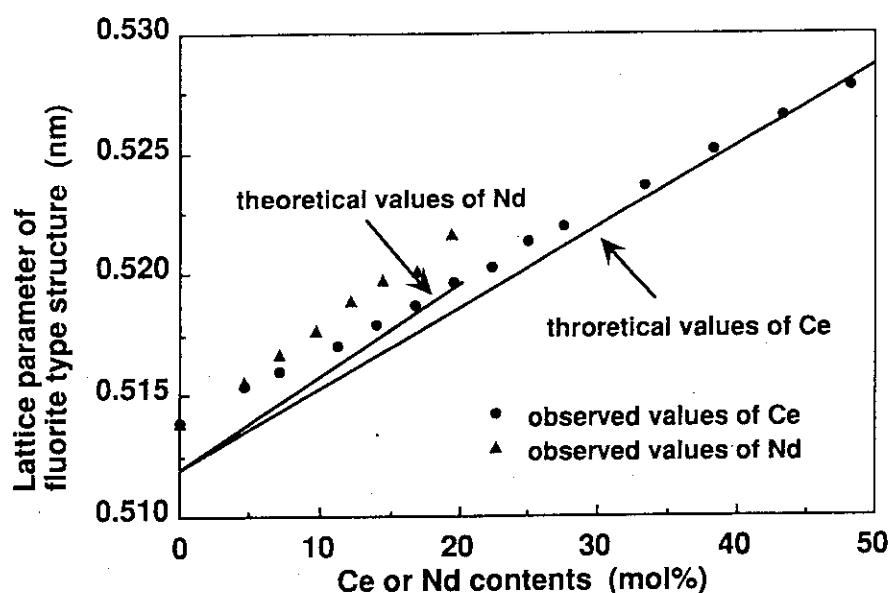


Fig. A-1 The observed and theoretical values of lattice parameters of fluorite type structure for samples containing Ce or Nd.

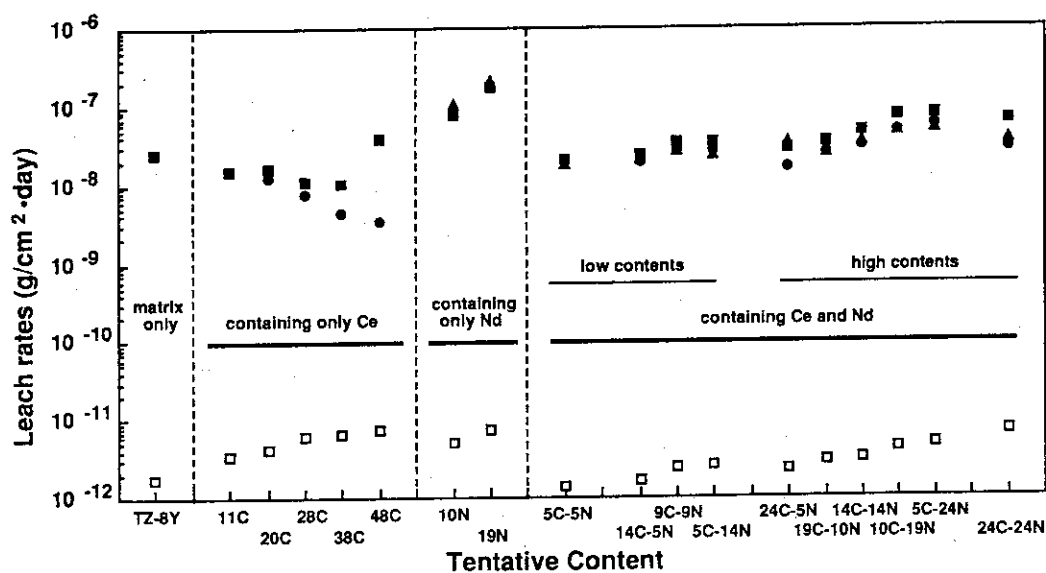


Fig. A-2 Leach rates of 16-34 days in nitric acid solution at 150°C. Powder samples of YSZ containing Ce and/or Nd were used in this tests. Sample names indicate contents of Ce and Nd.
 □ Leach rates of Zr, ● Leach rates of Ce,
 ▲ Leach rates of Nd, ■ Leach rates of Y

Table B-1 (A) Compositions of samples based on alumina based ceramics. (B) Lattice parameters of a and c axes of perovskite and magnetoplumbite phases, (C) relative amounts of the phases and (D) densities. (E) Leach rates of each element from ceramic in 0.1M HNO₃ and (F) in deionized water at 150°C for 28 days.

Sample	ACS	ACNS-1	ACNS-2	ANS
(A) Composition (mol%)				
Al	83.6	85.5	87.1	90.7
Nd	----	1.9	3.9	8.3
Ce	15.3	11.6	8.0	----
Si	0.9	1.0	1.0	1.1
(B) Lattice parameters (nm)				
Perovskite				
a axis	----	0.5332	0.5329	0.5321
c axis	----	1.3094	1.2982	1.2928
Magnetoplumbite				
a axis	0.5558	0.5554	0.5555	----
c axis	2.1999	2.2004	2.1985	----
(C) Relative amounts (%)				
α-alumina	0.0	15.9	34.6	45.2
Perovskite	0.0	13.9	34.2	54.8
Magnetoplumbite	100.0	70.2	31.2	0.0
(D) Apparent densities (g/cm ³)				
	2.21	2.47	3.02	3.41
(E) Leach rates in nitric acid solution (g/cm ² ·day)				
Al	6.12×10^{-6}	5.35×10^{-6}	3.41×10^{-6}	2.10×10^{-6}
Ce	8.43×10^{-6}	6.32×10^{-6}	3.52×10^{-6}	-----
Nd	-----	5.45×10^{-6}	2.72×10^{-6}	2.21×10^{-7}
(F) Leach rates in deionized water (g/cm ² ·day)				
Al	$<2.20 \times 10^{-9}$	$<2.19 \times 10^{-9}$	$<2.20 \times 10^{-9}$	$<2.21 \times 10^{-9}$
Ce	$<7.45 \times 10^{-9}$	1.00×10^{-8}	1.49×10^{-8}	-----
Nd	-----	1.01×10^{-7}	5.90×10^{-9}	5.29×10^{-8}

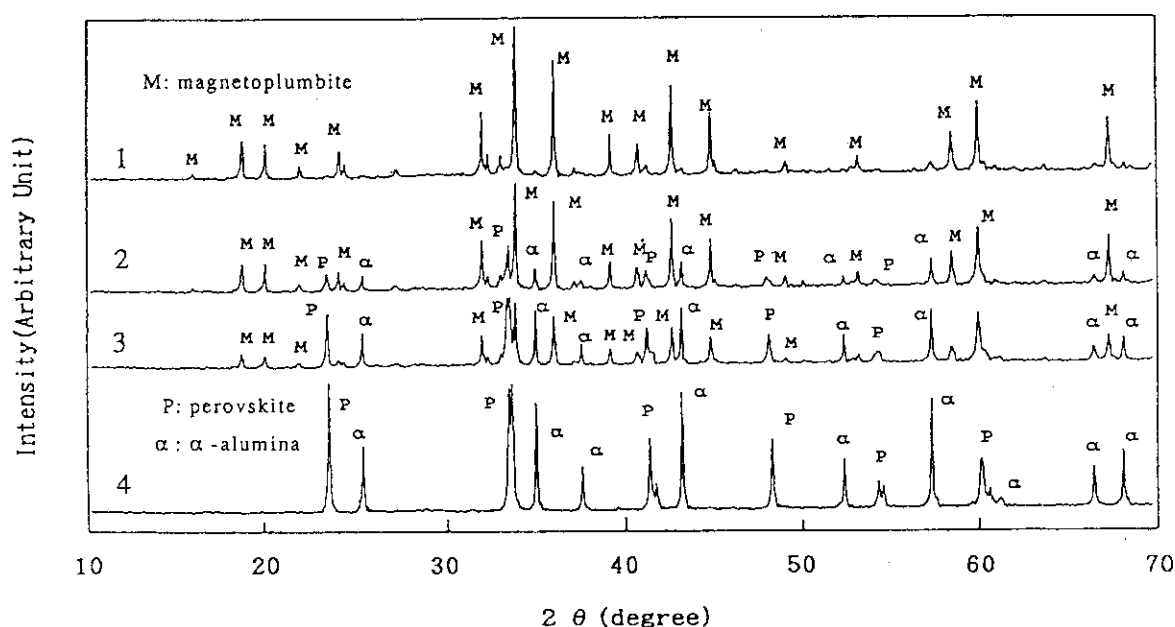


Fig. B-1 XRD patterns for alumina based ceramic samples containing Ce and Nd. 1: ACS, 2: ACNS-1, 3: ACNS-2, 4: ANS

1.3 Performance of Engineered Barrier Materials

1.3.1 Sorption Characteristics of Neptunium by Smectite

N. Kozai

Introduction

Sorption characteristics of neptunium by smectite (montmorillonite) which is one of the major clay minerals contained in bentonite (buffer material) have been studied by batch type sorption-desorption experiment.

Sodium type smectite (Na-smectite) which has sodium ions (Na^+) as interlayer cations is considered to be used as buffer material. After contact with underground water, the interlayer cation Na^+ of Na-smectite is supposed to be substituted with cations such as Ca^{2+} contained in underground water. Characteristics of smectite depend on cations sorbed as interlayer cations. Sorption characteristics of neptunium by smectite is, therefore, different between before and after the contact with underground water.

Effect of calcium ion on sorption of neptunium by smectite was studied because calcium ion is one of the most important cations contained in the underground water.

Experimental

Sorption experiments were carried out to discuss the relationship between pH of the neptunium solution and the amount of neptunium sorbed by smectite. Na-smectite (S_{Na}) and Ca-smectite (S_{Ca}) were prepared by substituting Na^+ and Ca^{2+} for interlayer cation of smectite respectively. Each smectite was added to the neptunium solution in polycarbonate centrifugation at 12000 rpm for 1 hr, and the pH and concentration of neptunium of the supernatant were measured. The same experiments with Na-smectite and the neptunium solution which contains $5 \times 10^{-4} \text{ mol} \cdot \text{l}^{-1}$ CaCl_2 ($S_{\text{Na,Ca}}$) were carried out.

Subsequently, desorption experiments using the sequential extraction procedure were carried out to clarify the association of neptunium with smectite. The smectite by which neptunium was sorbed was firstly treated with a 1M KCl at 20°C for 2 days. After another treatment with a 1M KCl,

the treatment with a 1M HCl was carried out for 2 or 3 times. At the end of each extraction step, the suspended solution was separated by centrifugation mentioned above.

Results

The K_d values of neptunium for smectite are shown in Fig. 1. At around pH 7.5, all samples had almost the same K_d value about $20 \text{ ml} \cdot \text{g}^{-1}$. Below pH 7.5, K_d s of $S_{\text{Na,Ca}}$ and S_{Ca} were smaller than S_{Na} . Below pH 5, K_d s for all samples show tendencies to increase with decreasing pH. However, those tendencies are different between S_{Na} and others, and increases of K_d s for S_{Ca} and $S_{\text{Na,Ca}}$ are seemed to be suppressed by the existence of calcium ion.

Percent fractions of neptunium desorbed from smectite by 1 M KCl solutions (P_{KCl}) are shown in Fig. 2. At around pH 7.5, P_{KCl} s for all samples became almost the same value of about 15. That for S_{Ca} decreased with pH until 7, and became constant below pH 7. Those for $S_{\text{Na,Ca}}$ and for S_{Na} slightly decreased with pH of the solution and both values were quite similar in this experimental pH region.

Percent fractions of neptunium desorbed from smectite by 1 M HCl solutions (P_{HCl}) are shown in Fig. 3. Above pH 5, P_{HCl} s for all samples were constant less than 5. Below pH 5, P_{HCl} s for all samples increased with decreasing pH. Although those for $S_{\text{Na,Ca}}$ and S_{Ca} are similar to each other, both of them are quite smaller than for S_{Na} below pH 5.

From these results of desorption experiments, calcium ion is considered to suppress the sorption of neptunium by smectite and in especial the sorption can be desorbed by 1 M HCl.

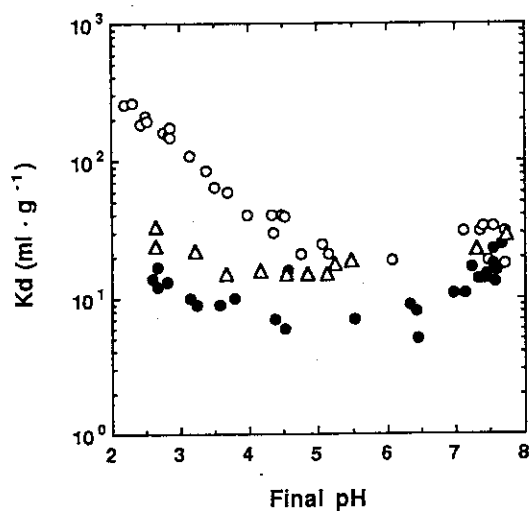


Fig. 1 Distribution coefficient (K_d) for smectite in different pH solution
○: S_{Na} , ●: S_{Ca} , △: $S_{Na,Ca}$

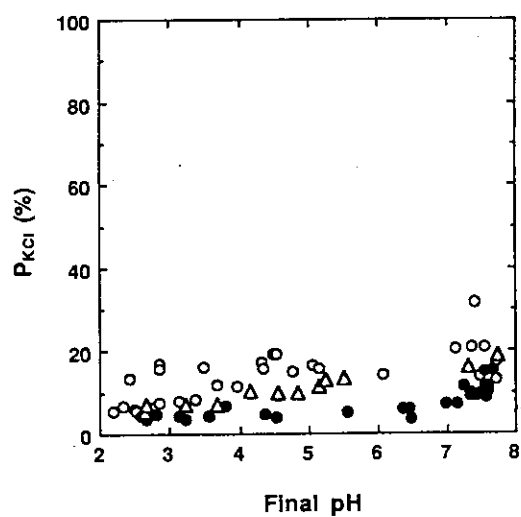


Fig. 2 Percent fraction of neptunium desorbed by 1 M KCl solution

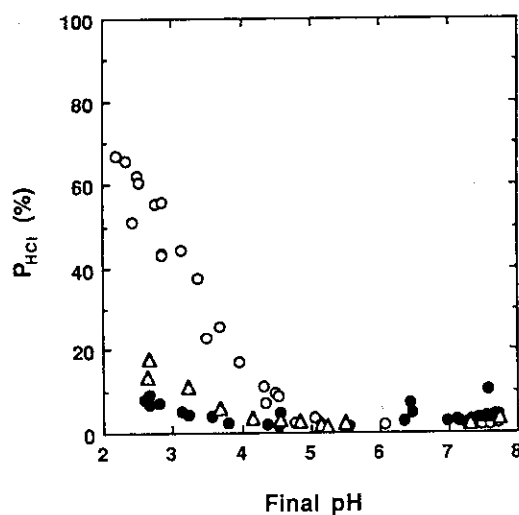


Fig. 3 Percent fraction of neptunium desorbed by 1 M HCl solution

1.3.2 Sorption Behavior of ^{14}C by Mortar

J. Matsumoto

Sorption of ^{14}C in mortar was determined by the batch method at 15°C . The batch test was carried out for the safety evaluation of shallow land disposal of low level radioactive waste.

Two chemicals, $\text{Na}_2^{14}\text{CO}_3$ (inorganic form) and $\text{CH}_3\text{CH}_2^{14}\text{CH}_2\text{OH}$ (hydrocarbon), were used as the source of ^{14}C . The solid materials used in this study were crushed mortar (grain size 0.50-1.0 mm) which was the mixture of ordinary portland cement, fine aggregates and water with a mass ratio of 1:2:0.55. The crushed mortars 0.30 g were contacted with 9.0 ml of pure water for 4 days. Then two chemicals isotopes leachates were added. The initial concentrations of ^{14}C were respectively 7.4×10^{-8} - 1×10^{-3} and 4.3×10^{-7} mol/l in Na_2CO_3 and $\text{CH}_3\text{CH}_2\text{CH}_2\text{OH}$. The Rd were calculated from the ^{14}C concentrations of leachates as follows:

$$\text{Rd} = \frac{(\text{amount of radionuclide sorbed} / \text{mass of solid})}{(\text{amount of radionuclide in solution} / \text{solution volume})} \quad [\text{ml/g}]$$

In the case of $\text{Na}_2^{14}\text{CO}_3$, each Rd-value increased rapidly with decreasing ^{14}C concentration, however, after 70 days Rd-value seemed to achieve an equilibrium state, except the Rd-value of D was scattered (Fig. 1). All Rd-values were high and constant at about 1×10^3 ml/g before centrifugation. The reason why the Rd-value of D was scattered, is seemed that much $\text{CO}_2(\text{aq})$ produced precipitate to combine with some cation of mortar contents because of CO_2 concentration was the highest. The carbonates formed by the reaction was seemed that was floating in the leachate. This precipitate was separated and the Rd-value was calculated (after centrifugation). The Rd-value before centrifugation was lower than that after centrifugation (Fig. 2). This difference between the Rd-values before and after centrifugation was attributed to the precipitate in the leachate. This precipitate was identified as calcite (CaCO_3) by the X-ray diffraction analyses (Fig. 3). Calcite was formed by the reaction between $\text{CO}_2(\text{aq})$ and Ca^{2+} leached from the mortar. The Rd-value will be high until mortar has been completely carbonated. This is because Ca^{2+} is rich in the mortar and the solubility of calcite is low.

In the case of $\text{CH}_3\text{CH}_2^{14}\text{CH}_2\text{OH}$, the Rd-value didn't change with time and was constant at about 1 ml/g after centrifugation (Fig. 4).

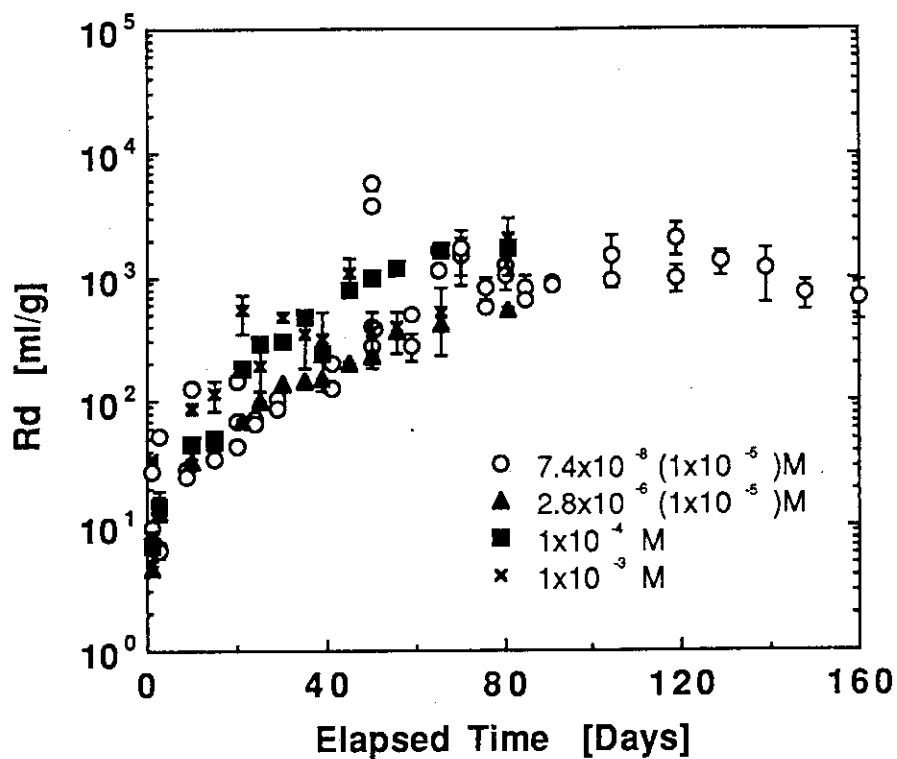


Fig. 1 R_d -values versus elapsed time at 15°C

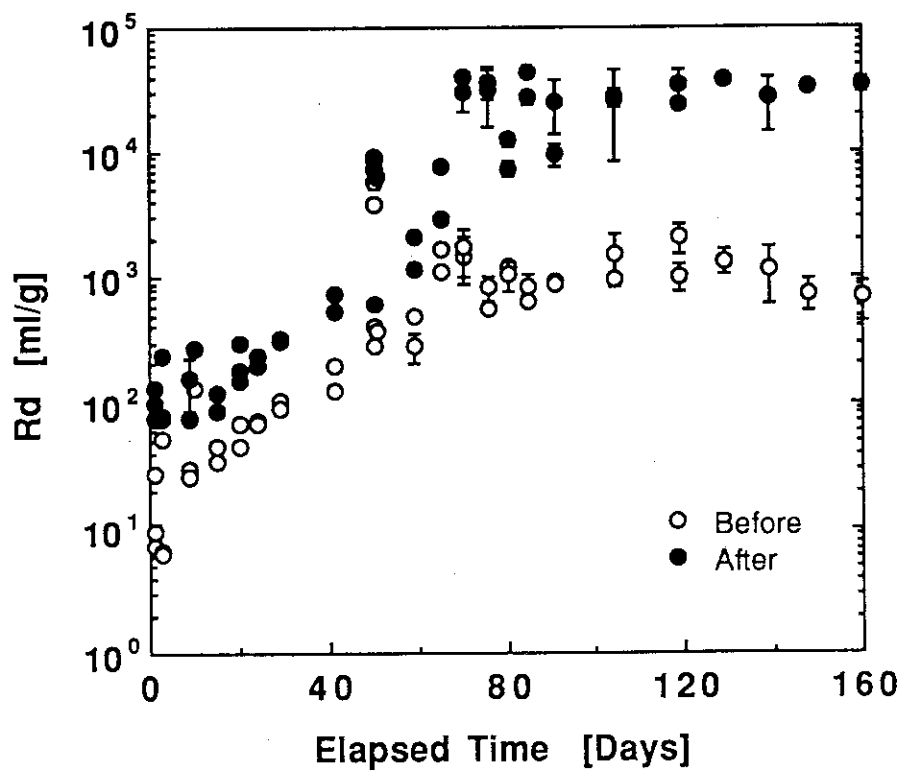


Fig. 2 R_d -values versus elapsed time at 15°C
(initial concentration of C-14; 7.4×10^{-8} M)

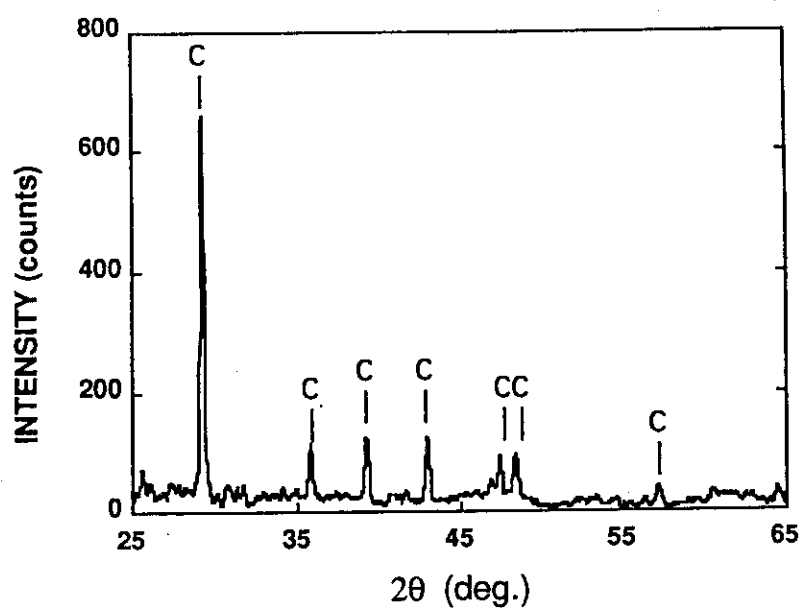


Fig. 3 Parts of X-ray diffraction pattern from the precipitate in the leachate

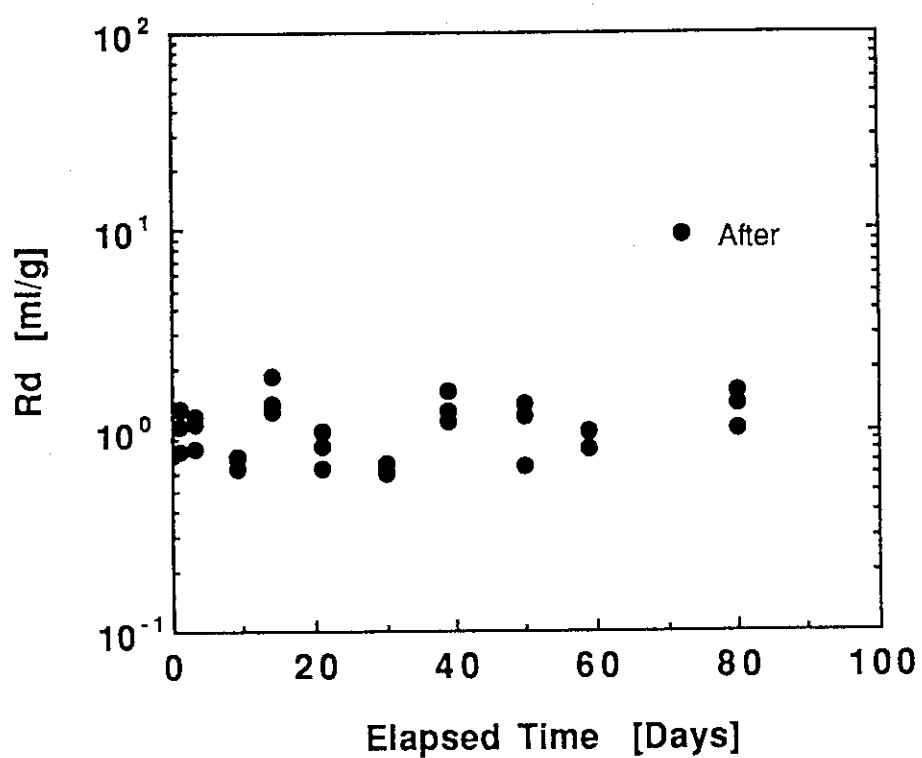


Fig. 4 Rd-values versus elapsed time at 15°C

1.3.3 Changes in the Properties of Mortar Containing Durability Improving Agent under Gamma-ray Irradiation

M. Mochizuki

Abstract

Concrete used in facilities for LLW is required to be highly durable. The authors evaluated an ordinary concrete and concretes containing a glycol ether derivative and silica fume as admixtures.

Compressive strength, depth of accelerated carbonation, diffusion coefficient of ^{137}Cs were investigated using mortar specimens before and after irradiation of gamma rays. Results showed that using glycol ether derivatives and silica fume was effective in improving the durability.

Experimental

Changes in the properties of mortar by irradiation of gamma rays were investigated. The proportioning of the specimens is presented in Table 1. The evaluations were made regarding compressive strength, accelerated carbonation, total pore volume and ^{137}Cs diffusion. ^{60}Co was used as the radiation source, and a dose of 10^9 R was irradiated to simulate exposure for 300 years, which is the term of control of LLW facilities.

Compression test: Cylindres 5 cm in diameter and 10 cm in length were made, and were tested after being cured in water at 20°C for 4 weeks.

Accelerated carbonation test: Prisms $4 \times 4 \times 16$ cm in size were made and cured in water at 20°C for 4 weeks, and were then dried in the atmosphere. The ends and the top and bottom surfaces with respect to the position as molded were coated with epoxy resin. The specimens were then placed in a room with a temperature of 30°C, a relative humidity of 60% and a carbon dioxide gas concentration of 5% for 4 weeks. After being removed from the room, the specimens were split at the center and the split surface was sprayed with an alcoholic solution of phenolphthalein. The depth of the uncolored portion was measured as the depth of carbonation.

Total pore volume: After compression test each specimen was crashed under

5mm in diameter, and was dried for a day after being immersed in acetone for a day. Then the total pore volume of each specimen was determined by means of mercury intrusion porosimetry. The superpressure was from 0.1 to 200 Pa, so the measured pore size was from 3.75 to 7500 nm.

^{137}Cs diffusion test: Cylinders 5 cm in diameter and 10 cm in length were made, and were cured in water at 20°C for 4 weeks. A slice 5 mm in thickness was sawed from the center of the specimen, and was set in a diffusion tester shown in Fig. 1. In one side, added ^{137}Cs of 830 Bq/ml into the pure water of 700 ml, with 0.1 mol/l CsCl as carrier, and another side, 700 ml of pure water, so as to measure the changes in the concentration of ^{137}Cs over time on the pure water side. The measurement was continued until the rate of concentration rise became constant, and the diffusion coefficient was calculated by Fick's law indicated as Eq. 1.

$$D_e = \frac{V_2 \times L}{A \times C_1} \times \frac{d C_2}{d t} \quad (1)$$

where D_e diffusion coefficient of ^{137}Cs (cm²/s)

V_2 volume of measured solution

L thickness of specimen

A cross-section of diffusion

C_1 initial concentration of ^{137}Cs

C_2 measured concentration of diffused ^{137}Cs

Results and Discussion

The results of the experiments are shown in Table 2 and Fig. 2. The inclination of the concentration curve when the rate of change over time became constant was obtained from Fig. 2, to calculate the diffusion coefficient. As for AEC, the compressive strength was not affected by the irradiation of gamma rays, whereas the depth of accelerated carbonation and total pore volume slightly increased, and the coefficient of ^{137}Cs diffusion substantially increased. As for GEC and HDC, the irradiation of gamma rays led to increases in the compressive strengths as well as in the depths of accelerated carbonation, although the resulting depths of carbonation were less than that of AEC. Virtually no change was observed in the total pore volume and the coefficients of ^{137}Cs diffusion in GEC and HDC after the irradiation. The resulting depths of carbonation were

similar to that of AEC before the irradiation. The losses in the effect of inhibiting carbonation resulting from the irradiation are therefore considered to cause no problem. Gamma rays are considered to chemically alter the durability improving agent contained in the mortar, increasing the content of acid substances, which led to a decrease in the alkali content in the mortar. This may be the cause of the loss in the effect of inhibiting carbonation, which depends on the alkali content. On the other hand, the effect of inhibiting ^{137}Cs ion penetration is considered to be brought about solely by the densification of the structure. Since no change in the total pore volumes were observed after the irradiation in these tests, it is considered that the irradiation led to no change in denseness of the structure.

Reference

1. Kunio Yanagihashi et al., "Concrete Containing a Durability Improving Agent for LLW Facilities", Proceedings of the International Conferences and Technology Exposition on Future Nuclear Systems: Emerging Fuel Cycles and Waste Disposal Options Global '93. September 12 - 17, 1993 Seattle, Washington, pp. 949-956 (1993)

Table 1 Mix proportion of mortar

	Water Cement	Sand Cement	Silica fume	Admixture
AEC	0.45	2	-	poly-alkyl sulfate
GEC	0.45	2	-	durability improving agent
HDC	0.45	2	10% as cement	durability improving agent

Table 2 The results of tests using mortar

Radiation	AEC		GEC		HDC	
	before	after	before	after	before	after
Compressive strength (MPa)	63.3	63.8	68.4	89.3	75.5	80.6
Accelerated carbonation depth (mm)	6.5	8.4	2.4	7.4	2.8	7.6
Total pore volume (cm ³ /g)	0.067	0.077	0.053	0.051	0.048	0.045
Diffusion coefficient of ¹³⁷ Cs ($\times 10^{-9}$ cm ² /s)	9.48	49.8	4.72	4.40	0.53	0.76

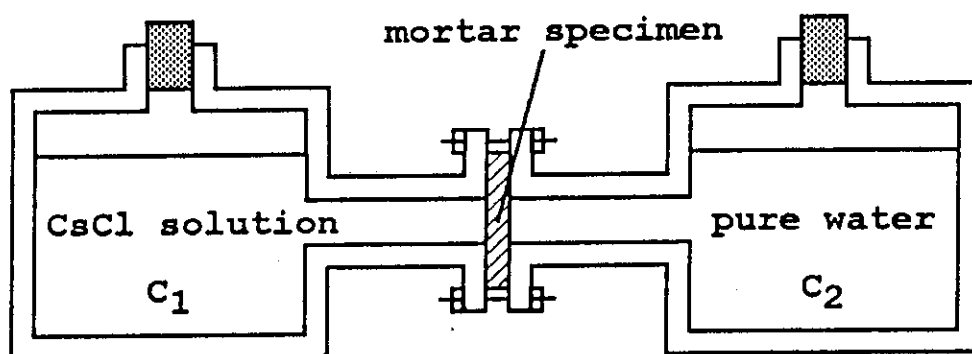


Fig. 1 The vessel of ^{137}Cs diffusion test

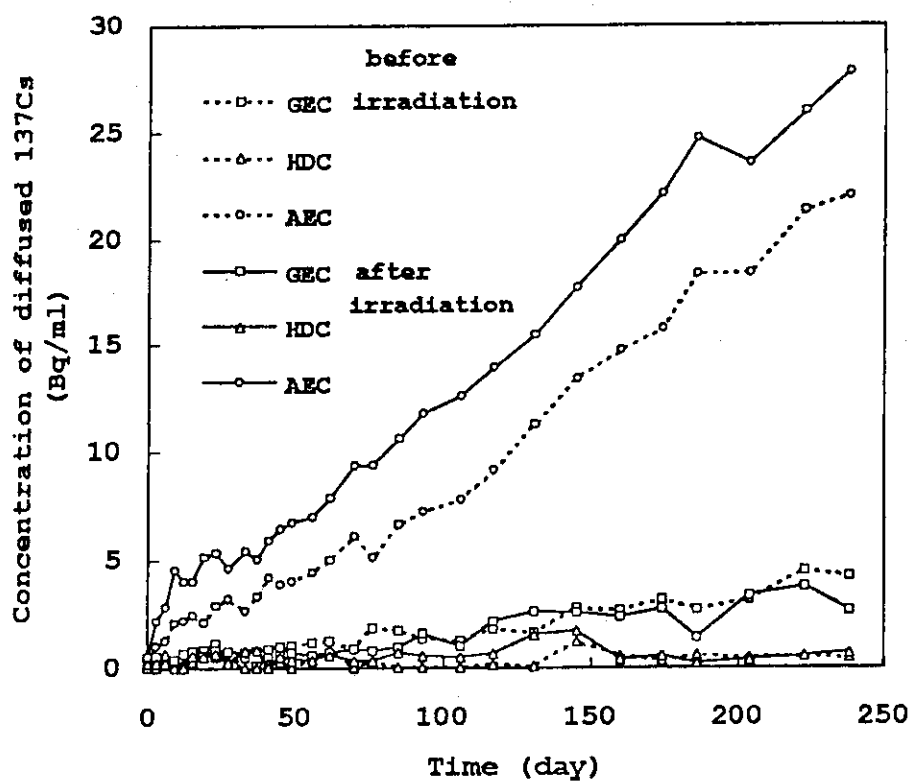


Fig. 2 The result of means of the concentration of diffused ^{137}Cs at diffusion test

2. Safety Evaluation Study on Shallow Land Disposal

2.1 Nuclide Migration Study

2.1.1 Migration Behavior of Radionuclides on the Undisturbed Soil Layer

S. Takebe, M. Mukai and T. Komiya

1. Introduction

Safety evaluation test on the shallow land disposal of Low Level Radioactive Waste (LLRW) has been performed to evaluate the migration behavior of ^{60}Co , ^{85}Sr and ^{137}Cs in the undisturbed soil layer under the natural condition. Layers of typical subsurface soil layers in Japan, including the candidate final storage site, were investigated for their radionuclide migration delaying capability in a large scale column test using undisturbed soil samples. In the large column test, the cationic species were adsorbed mainly near the surface of the soil layer^(1,2), but very small portion of radionuclides were found to be distributed at very low concentration deeper area. A low concentration of ^{60}Co was detected in the column effluent. A desorption migration test was conducted with ^{60}Co evaluate the migration behavior of the low adsorbing portion more quantitatively.

2. Experiment

The experimental apparatus as shown schematically in Fig. 1 is composed of a soil column, a pump, an autosampler, a sprinkler, a sample solution tank, etc. The column size was 30 cm in inner diameter and 120 cm in length, soil samples (30 cm ϕ \times 60 cmh) of undisturbed soil layer were taken from a candidate final storage site. The desorption migration test of the aerated subsurface soil layer was accomplished by putting a contaminated thin soil layer labeled with each 37 MBq of ^{60}Co , ^{85}Sr and ^{137}Cs on the top of an undisturbed soil layer. Artificial groundwater containing ^3H was supplied at an inflow rate of about 0.1 cm/h until ^3H was detected in the effluent. Effluent samples were periodically collected in 1,000 ml fraction by the autosampler. The effluents collected in the polyethylene vessel were subjected to the radioactivity measurement. After the column test, in the soil layer was obtained by disassem-

bling the column, sampling the soil from various parts of the soil layer. The soils sampled were finally measured the radioactivity. The concentrations of radionuclides in the effluent samples and in the soil samples were determined with a pure Ge semiconductor detector.

3. Result and Discussion

^{85}Sr and ^{137}Cs were not observed in the deeper soil layer of the column at such a low inflow volume, ^{60}Co showed a low concentration migration profile with a concentration peak in the deeper soil layer. Fig. 2 shows the results of the desorption migration test on a loamy soil and a sandy tuff soil. The distribution profile of the desorbed ^{60}Co in the loamy soil layer showed most of the ^{60}Co was retained within a depth of several cm from the surface, and that its very small portion was transported to a deeper area to form a small concentration peak of a few Bq/g. The profile for sandy tuff soil showed ^{60}Co was transported to a deeper location to form concentration peak of a few Bq/g. A very low concentration of ^{60}Co lower than 0.1 Bq/ml began to be detected in the effluent, accompanied with breakthrough of ^3H tracer in the groundwater. These two forms of migration behavior of ^{60}Co were seemed to be related to the difference in their chemical forms. Such mechanisms as a strong ion-exchange reaction for cationic species, and a weak first-order reversible reaction for non-cationic species are tentatively attributed. The behavior of the weak adsorbing species was analyzed by using a migration model where a limited fraction of noncationic species originally contained in the contaminated layer is desorbed and transported with the groundwater flow. The species weakly interacts through adsorption and desorption reactions with soil since the adsorption capacity of the soil for the species has a very low upper bound^(3,4). The distribution profile in the soil column and the concentration change in the effluent were predicted consistently for all tests using appropriate parameter values for this model, as shown in Fig. 2.

References

- (1) T. Yamamoto, S. Takebe, H. Ogawa, T. Tanaka, M. Mukai, T. Komiya, S. Yokomoto and Y. Wadachi: "Migration behavior of radionuclide in soil layer of final storage site -- Radionuclide migration test in aerated soil layer by precipitation --", JAERI-M 89-189(1989).
- (2) T. Yamamoto, S. Takebe and H. Ogawa: "Large column test for radionuclide migration in soil layer", in Proceeding of 3rd International Symposium on Advanced Nuclear Energy Research, Mito, March 1991 edited by JAERI, p420(1991).
- (3) S. Takebe, M. Mukai, T. Komiya and H. Kamiyama: "Radionuclide migration behavior at the low adsorption region on the aerated soil testing", JAERI-M 92-205(1992).
- (4) S. Takebe, M. Mukai, T. Komiya and H. Kamiyama: "Radionuclide Migration behavior at the low adsorption region on the aerated soil testing -- The Second Report; Effect of inflow volume and migration analysis --", JAERI-M 93-034(1993).

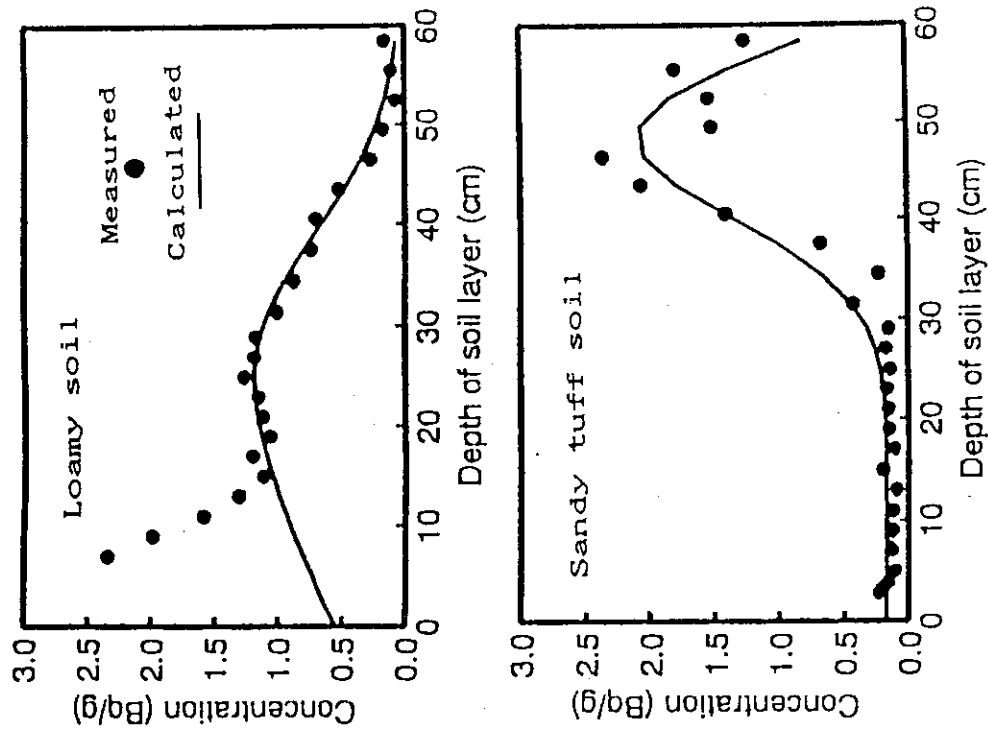


Fig. 2 Comparison of the experimental results of ^{60}Co in the desorption migration test with the calculated distribution curve of the low absorbing species using the migration model.

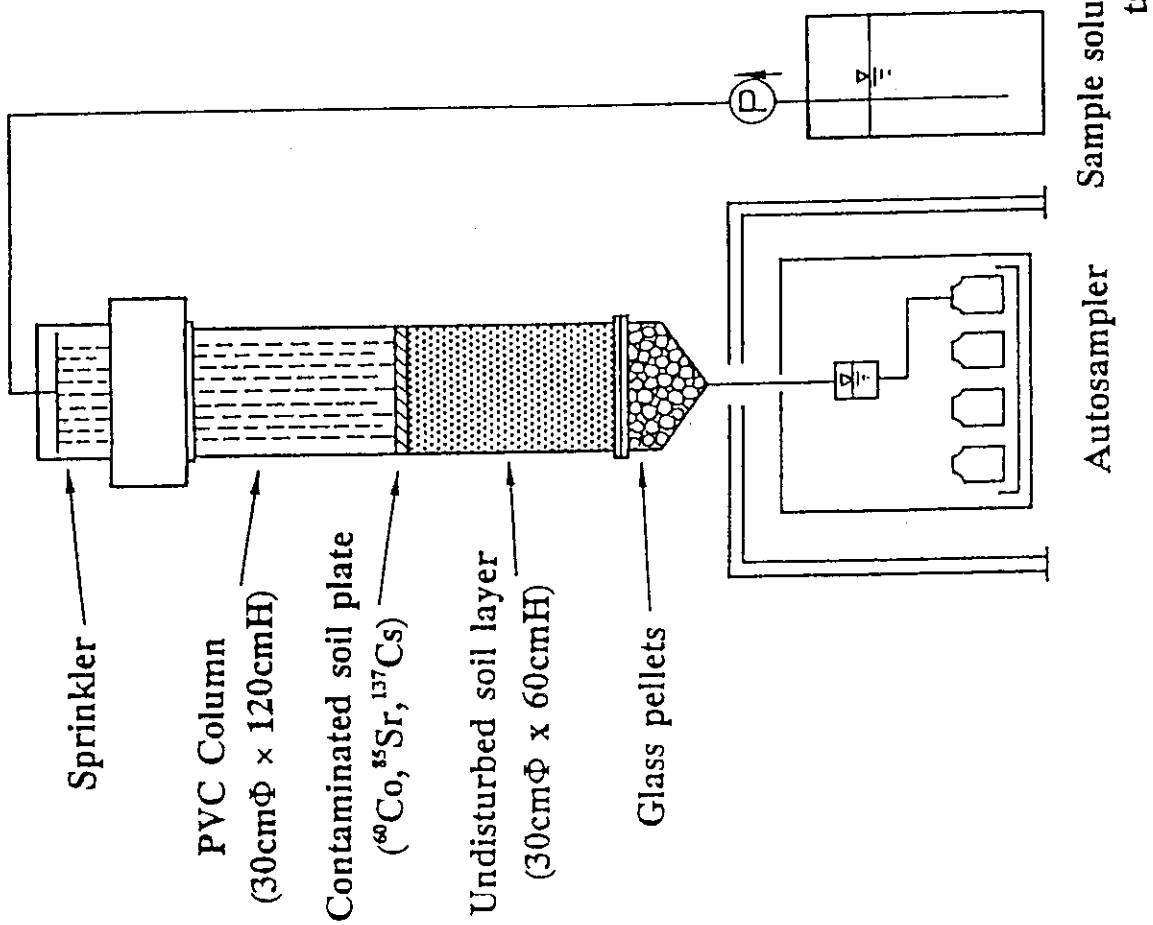


Fig. 1 Schematic diagram of the apparatus for radionuclides migration in the soil column.

2.1.2 Ground Surface Radionuclide Migration Test

M. Mukai, S. Takebe and T. Komiya

1. Introduction

Radionuclide migration by ground surface water flow is considered to be one of important path ways in the scenario for environmental migration of the radionuclide leaked from LLRW depository. At the site having shallow groundwater level, surface water is possibly generated during and after rainfall. Once the surface water flow has been generated, radionuclides in the flow are rapidly carried towards downstream and moved into lakes and/or rivers.

Ground surface radionuclide migration test has been carried out to evaluate the migration behavior of ^{60}Co , ^{85}Sr and ^{137}Cs in the flowing water on the ground surface. Loamy soil layer as a typical subsurface soil layer in Japan was investigated for their adsorbing capability against the radionuclides migration by a ground surface test using soil samples.

2. Experimental Method

The radionuclide migration test was carried out by using a loamy soil sample of 240 cm in length to investigate the interaction between the soil surface and the radionuclides. The loamy soil was taken from near the final storage site in Aomori prefecture. The apparatus for the test are consist of an inlet, soil and outlet vessels (Fig. 1).

To minimize radionuclide migration from the solution into the sample accompanied by infiltration, the soil sample was fully saturated before starting the test. To investigate radionuclide migration at various hydraulic conditions, the test was carried out under combined conditions of the flow rate of 30, 100, 200 ml/min and the duration time of 2.5, 10, 45, 200 hrs.

The radionuclides concentration change in the effluent with elapsed time and their adsorbed concentration distributions on the ground surface were obtained in the test.

3. Result and Discussion

Among the 6 conditions, the radionuclides concentration in the effluent obtained under the different flow rate is summarized in Fig. 2. From the Fig. 2, the concentration was nearly constant during each experimental period, and was reduced with lower flow rate.

The surface distribution of radionuclides concentration at the flow rate of 100 ml/min is shown in Fig. 3. Among the three radionuclides, ^{137}Cs was most adsorbed on the soil surface. The surface distribution of radionuclides concentration showed two distinctive regions. The one was near the inlet where it was promptly reduced, and the another was a region following the former where it was nearly constant.

The following equations are used to evaluate the results of migration test.

$$\frac{\partial C}{\partial t} = D_x \frac{\partial^2 C}{\partial x^2} + D_z \frac{\partial^2 C}{\partial z^2} - V_x(z) \frac{\partial C}{\partial x} \quad (1)$$

$$\frac{\partial C}{\partial t} + \frac{\partial Q}{\partial t} = D_x \frac{\partial^2 C}{\partial x^2} + D_z \frac{\partial^2 C}{\partial z^2} \quad (2)$$

$$V_x(z) = \frac{3}{2} V_m \left(1 - \left(1 - \frac{z}{H} \right)^2 \right) \quad (3)$$

$$\frac{\partial Q}{\partial t} = k_1 \cdot C \quad (4)$$

where, V_x represents vertical flow rate distribution simulating laminar flow and is zero at the bottom of the flow. The equation (4) for the radionuclides adsorption are obtained from time dependence of concentration of the sample taken from the nearest position to the inlet vessel.

Most probable values of the parameters were obtained to simulate the measured concentration distribution by fitting operation. A part of the concentration distributions calculated with the obtained values of the parameters is shown in Fig. 4. The features of measured distribution are well explained by the model.

Reduction of effluent concentration with distance was estimated by the following equation.

$$C(x) = C_0 \times 10^{-a \cdot x^b} \quad (5)$$

where, parameters a and b are determined by their values to fit to the effluent concentration calculated by the model. Figure 5 shows estimation of concentration change of ^{137}Cs with flowed distance. At the distance of 100 m, effluent concentration was reduced to 0.3% at the flow rate of 3.75 cm/min and about 20% at 25 cm/min. These are considered to be smaller for the condition of natural ground surface because of its higher roughness of the surface.

4. Conclusion

To evaluate the radionuclide migration from flowing solution on the ground surface to soil, the ground surface radionuclide migration test was conducted by using loamy soil sample. Duration change of radionuclide concentration in effluent is constant during experimental period and more reduced with lower flow rate. Distribution of surface radionuclide concentration showed promptly reduced and nearly constant regions. These characteristic features in their surface distribution could be explained by a two dimensional diffusion model with a first order adsorption reaction, based on the advection having a vertical flow rate distribution.

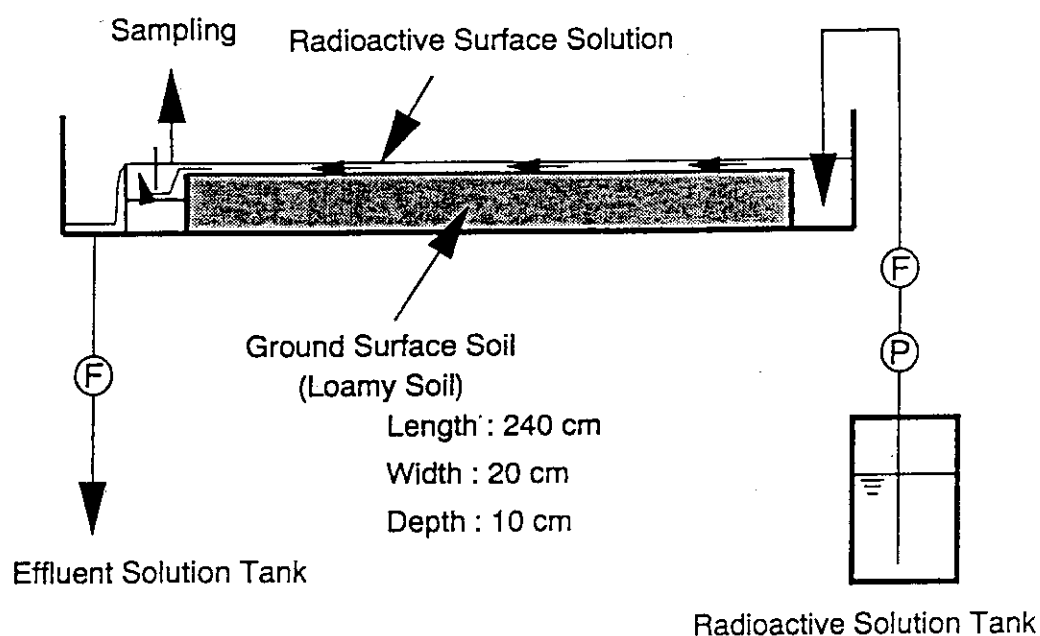


Fig. 1 Apparatus for ground surface radionuclide migration test.

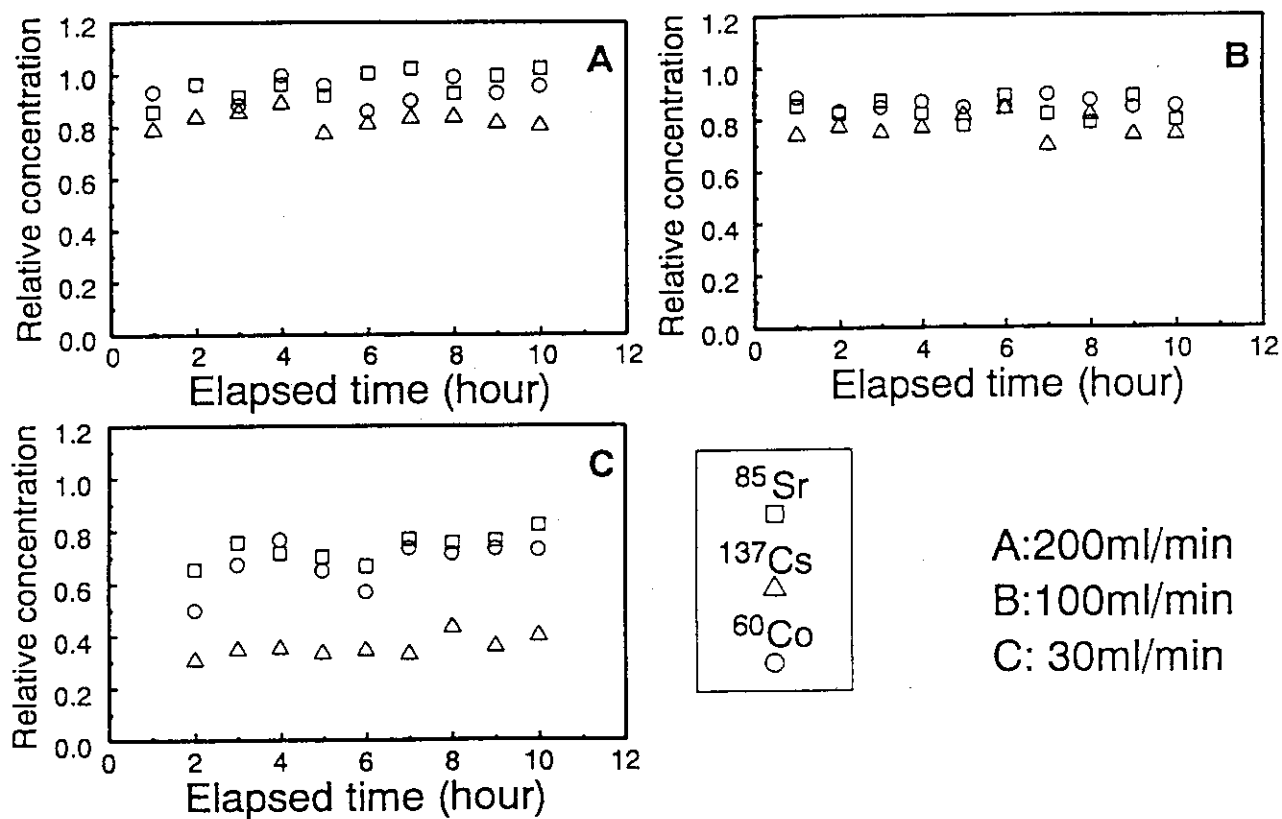


Fig. 2 Change of radionuclide concentration in effluent solution.

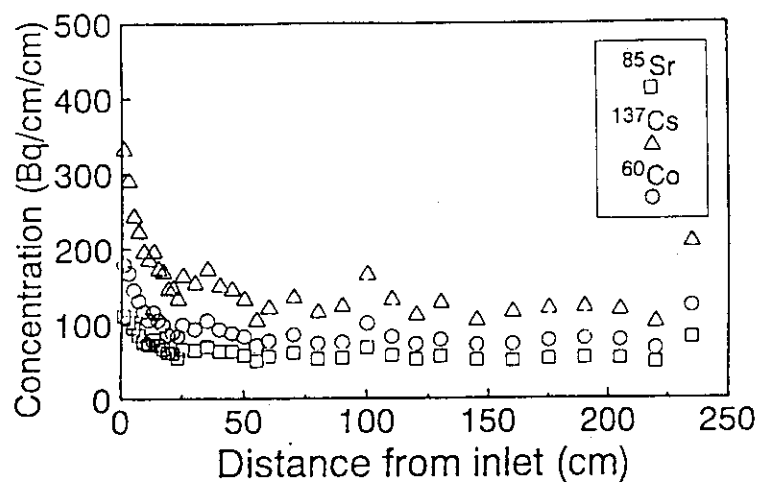


Fig. 3 Distribution of radionuclide concentration of ground surface soil (flow rate: 100 ml/min).

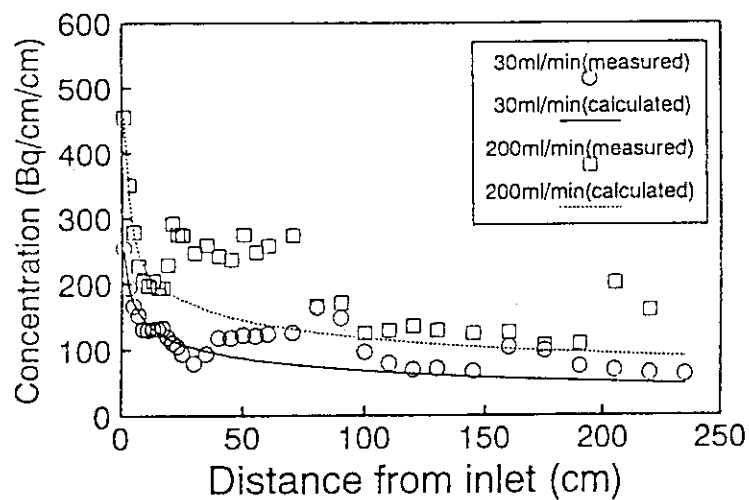


Fig. 4 Concentration distribution calculated with the most probable values of parameters.

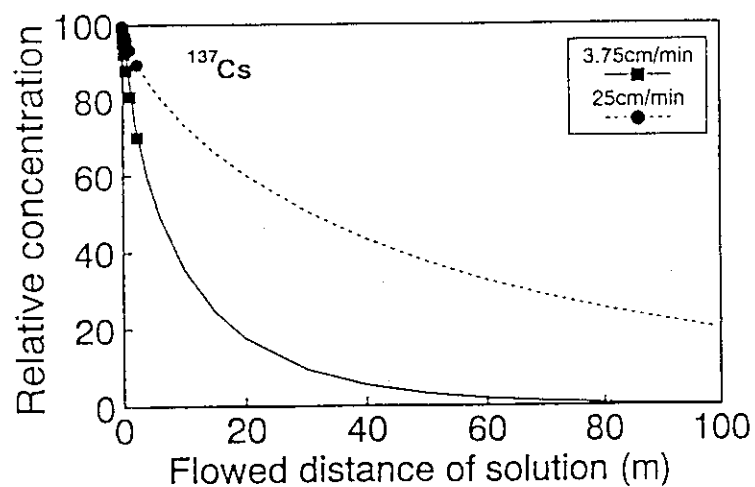


Fig. 5 Reduction of radionuclide concentration with flowed distance by estimation.

2.1.3 Influence of Humic Acid on Migration of ^{60}Co , ^{85}Sr and ^{137}Cs in Coastal Sandy Soil

T. Tanaka and Shiwei Ni

1. Introduction

The migration of radionuclide in a shallow land is controlled by both flow characteristics of interstitial water in soil layer and physico-chemical states between radionuclide and soil. Since almost of all ionic radionuclides are interacted with soils, mobility of the radionuclides in a soil layer is retarded by the interaction. This interaction is affected by environment surrounding the radionuclides, such as pH, Eh, temperature, coexistent ion, oxygen, and humic acid⁽¹⁻⁵⁾. As humic acid has substantial chelation properties for metals, especially transition metals, it considerably affects on the sorption and migration behavior of the radionuclides in soil layer. From a geochemical point of view, it is important to know reactivity of humic acid with the radionuclides released from radioactive-waste repository.

We have studied to obtain more detailed information on the influence of humic acid complexing on the mobility of ^{60}Co , ^{85}Sr and ^{137}Cs in a coastal sandy soil. The present work focuses on a correlation between molecular-weight of the dissolved humic acid and ability of the complexing with the radionuclides in liquid phase.

2. Experimental

2.1 Materials

Geological sample used in this experiment was a coastal sandy soil collected at a site of the Tokai Research Establishment, JAERI. It was air-dried and washed with deionized water, and then sieved into a range from 250 to 350 μm in diameter.

Humic acid was purchased from the Aldrich Chemical Co. and was purified by the following procedure described by Nash et al.⁽⁶⁾.

A radioactive aqueous solution containing ^{60}Co , ^{85}Sr and ^{137}Cs was prepared into ca. 3.7×10^3 or 3.7×10^4 Bq/ml in concentration of each radionuclide.

2.2 Sorption experiment by batch method

After 2.5 g of the soil sample and 50 ml of the humic acid solution were transferred into 200 ml glass Erlenmeyer flasks, the radioactive solution (3.7×10^4 Bq/ml) mentioned above was added. It was kept constant at 0.01 for ion strength, 7 for pH and 25°C for temperature respectively. The solutions with the soil were gently agitated on a reciprocal shaker for 7 d. Supernatant was sampled and the concentration of the humic acid and the radionuclides was analyzed. Blank tests were also carried out to examine the concentration of them in the solution before and after the mixing with the soil.

Molecular-weight of the aquatic humic acid and the radionuclides species in the solution was classified into 6 ranges by ultrafiltration technique with Millipore filters of 5,000, 10,000, 30,000, 100,000 and 300,000 in cutoff molecular weight.

Humic acid concentration in solution were measured with spectrophotometer.

2.3 Migration experiment by column method

A sandy soil layer was prepared by packing the sandy soil into a column (25 ϕ ×5 cm) to make a bed of 5 cm thickness. The radioactive solution (3.7×10^3 Bq/mol) of 500 ml was inflow into the sandy soil layer from the bottom, at a flow rate of 1 ml/min. The radioactive solution was prepared to 0.01 for ion strength, 7 for pH, and 10 ppm-C for humic acid concentration. After the inflowing procedure, the sandy soil layer was cut into sections of 0.5 cm thick. Activity of the radionuclides in the soil section samples was measured.

3. Results and Discussion

3.1 Sorption behavior of radionuclides

The relation between sorption ratio of the radionuclides and the concentration of dissolved humic acid is shown in Fig. 1. The sorption ratio of ^{60}Co decreased with increasing concentration of coexistent humic acid. Those of ^{85}Sr and ^{137}Cs were not affected by the coexistence of humic acid.

Figure 2(a)~(d) show the molecular-weight distribution of dissolved

humic acid, and of dissolved ^{60}Co , ^{85}Sr and ^{137}Cs species, before and after the sorption experiments, under the condition with 35.0 ppm-C of humic acid. According to the blank test of humic acid, the rapid decrease of the concentration of humic acid was seen in the range of 100,000 ~ 30,000 of molecular-weight. This means that the bulk of dissolved humic acid was present in molecular-weight range from 30,000 to 100,000, as shown in Fig. 2(a). The concentration of dissolved humic acid in each fraction and the distribution profile of molecular-weight were not varied before and after the sorption experiments. This result reveals that all fractions of humic acid are hardly sorbed by the sandy soil.

Figure 2(b) shows the molecular-weight distribution of ^{60}Co species in the solution before and after mixing with a suspension of the sand. The ^{60}Co concentration in each fraction decreased after the sorption experiment, due to the sorption of ^{60}Co onto the sandy soil. Profile of the molecular-weight distribution of ^{60}Co was very similar to that of humic acid shown in Fig. 2(a). Similar profiles of molecular-weight distribution of ^{60}Co and humic acid indicate that the dissolved humic acid contributes a forming of humic-complex of ^{60}Co and the forming ability is independent of molecular-weight of humic acid.

The reduction ratio of the ^{60}Co concentration in the sorption experiment to that in the blank test was nearly constant in each fraction of molecular-weight, though the concentration of ^{60}Co in each fraction of molecular-weight decreased in the sorption experiment compared with that of ^{60}Co in the blank test. There are humic acid, humic-complex of ^{60}Co , and cationic ^{60}Co and its hydroxides in the solution. Appeared sorption of ^{60}Co is seemed to be based on a reaction with cationic ^{60}Co species, because humic acid is not sorbed onto the sandy soil as observed in Fig. 2(a). The concentration of ^{60}Co in the all six fractions was constantly decreased by the sorption experiment, despite only the cationic ^{60}Co species existing in <5,000 fraction was removed from the solution. These results are explained in the following.

There are two equilibrium processes in the static sorption experiment; one is a sorption process of the cationic ^{60}Co and the other is a complexation process with humic acid. When the cationic ^{60}Co is removed from the solution, it will be supplied by reverse reaction of the complexation process. In addition, kinetics of the complexation is attained more immediately than kinetics of the sorption. It is reported that the sorption process have been proceeding over 7 d in experimental period^(1,4),

while the complexation process is completely achieved within 2 h⁽⁷⁾. Equilibrium of the complexation process is completed during the experimental period, so the proportion of each ⁶⁰Co species is to be kept at a constant in the solution.

Figure 2(c) shows the molecular-weight distribution of ⁸⁵Sr species in the solution before and after mixing with the sandy soil. The molecular-weight distribution profile before the sorption experiment was rather similar to that of ⁶⁰Co and humic acid. This reveals that ⁸⁵Sr is also interacted with humic acid. Concentration of ⁸⁵Sr in each fraction was decreased by the sorption experiment, as is seen in the experiments of ⁶⁰Co. The reduction ratio of the ⁶⁰Co concentration in the sorption experiment to that in the blank test was nearly constant over the entire molecular-weight range as seen in Fig. 2(b), however, different reduction ratio of ⁸⁵Sr was observed between over and under 30,000 of molecular-weight in both experiments: blank test and sorption experiment of ⁸⁵Sr. The reduction ratio of ⁸⁵Sr concentration was calculated between over and under 30,000. The reduction ratio for the range over than 30,000 was 70% and that for the range under than 30,000 was 40%, respectively. Such results suggest that the interaction of ⁸⁵Sr with humic acid is dependent on the molecular-weight of dissolved humic acid.

Molecular-weight distribution of ¹³⁷Cs species which remained in the solution before and after the sorption experiments shows a different profiles from those of ⁶⁰Co and ⁸⁵Sr, as shown in Fig. 2(d). The ¹³⁷Cs concentration in each fraction was significantly decreased by the sorption experiment. This indicates that the ¹³⁷Cs species did not form humic-complexes and those molecular-weights were under 5,000.

3.2 Migration behavior of radionuclides

Concentration profiles of the three radionuclides in the sandy soil layer are shown in Fig. 3(a)~(c). The mobility of ⁶⁰Co and ⁸⁵Sr under the condition with coexistence of humic acid was larger than that under the condition with absence. On the other hand, the ¹³⁷Cs was not affected by the coexistence. Such tendency suggests that the complexed ⁶⁰Co and ⁸⁵Sr with humic acid move to the deeper and come out through the column. In the case of the coexistence of humic acid, concentration of ⁶⁰Co decreased little with increasing depth of the soil layer but that of ⁸⁵Sr decreased rapidly compared with the ⁶⁰Co. Both profiles of ⁶⁰Co and

^{85}Sr without humic acid look similar each other. This means that the coexistence of humic acid affects strongly on the mobility of ^{60}Co than that of ^{85}Sr .

Increase of the ^{60}Co mobility under the condition with coexistence of humic acid agreed with an estimation from the decrease of sorption ratio with increasing humic acid concentration as seen in Fig. 1. No change was seen in the mobility of ^{137}Cs between the absence and coexistence of humic acid. No change was also seen in the sorption ratio of ^{137}Cs . It was kept constant. However, the mobility of ^{85}Sr increased under the condition with coexistence of humic acid, in spite of the sorption ratio of ^{85}Sr was not affected by the coexistence. Such contradiction for ^{85}Sr might be caused by different kinetics between static state by batch method and dynamic state by column method.

4. Conclusion

Dissolved humic acid was complexed with ^{60}Co and ^{85}Sr . The complexation ability of ^{60}Co was independent of molecular-weight of humic acid, while that of ^{85}Sr depended on. The mobility of ^{60}Co and ^{85}Sr increased in the sandy soil layer under the condition with coexistence of humic acid. The sorption ability and mobility of ^{137}Cs were not affected by the coexistence of the humic acid.

References

- (1) B. Torstenfelt, K. Andersson and B. Allard: Chem. Geol, 36, 123 (1982).
- (2) T. Tanaka, T. Yamamoto, S. Kato and H. Kazama: J. At. Energy Soc. Japan, 33[4], 373 (1991), (in Japanese).
- (3) P.M. Jardine, N.L. Weber and J.F. McCarthy: Soil Sci. Soc. Am. J., 53, 1378 (1989).
- (4) D.M. Nelson, W.R. Penrose, J.O. Karttunen and P. Mehlhaff: Environ. Sci. Technol., 19, 127 (1985).
- (5) T. Tanaka and T. Yamamoto: J. At. Energy Soc. Japan, 30[10], 933 (1988), (in Japanese).

- (6) K. Nash, S. Fried, A.M. Friendman and J.C. Sullivan: Environ. Sci. Technol., 15, 843 (1981).
- (7) H. Kerndorff and M. Schnitzer: Geochim. Cosmochim. Acta, 44, 1701 (1980).

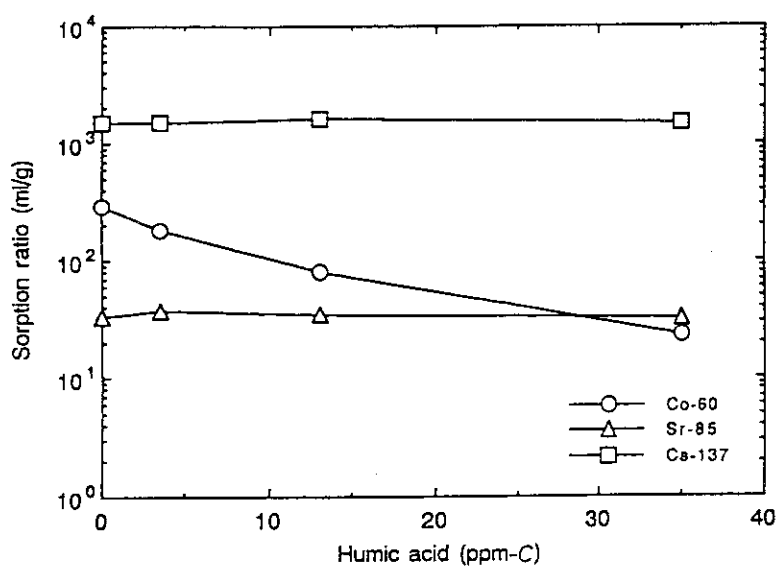


Fig. 1 Relation between sorption ratio and dissolved humic acid concentration.

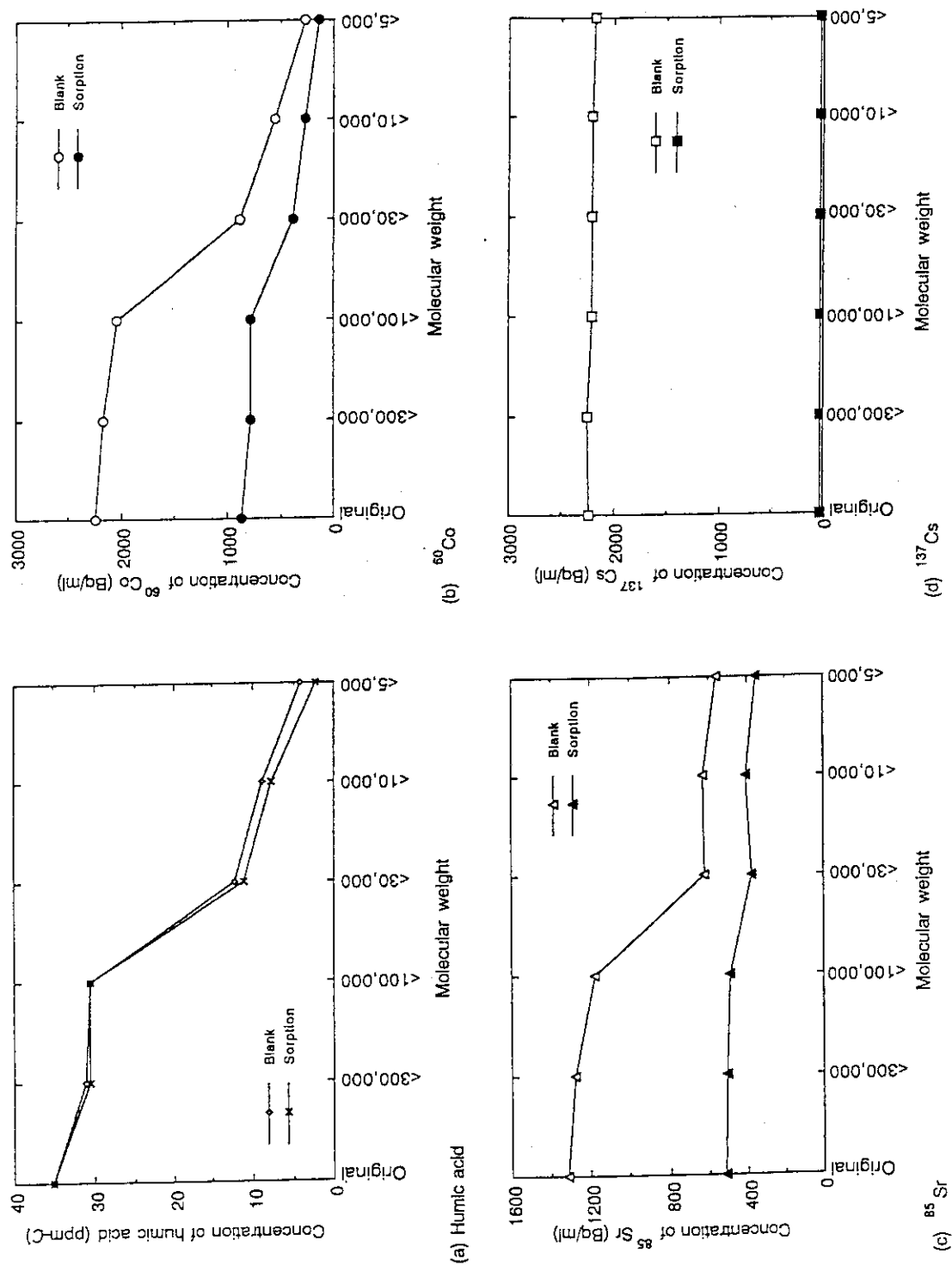


Fig. 2 Molecular-weight distribution of dissolved humic acid, and of dissolved ^{60}Co , ^{85}Sr and ^{137}Cs species.

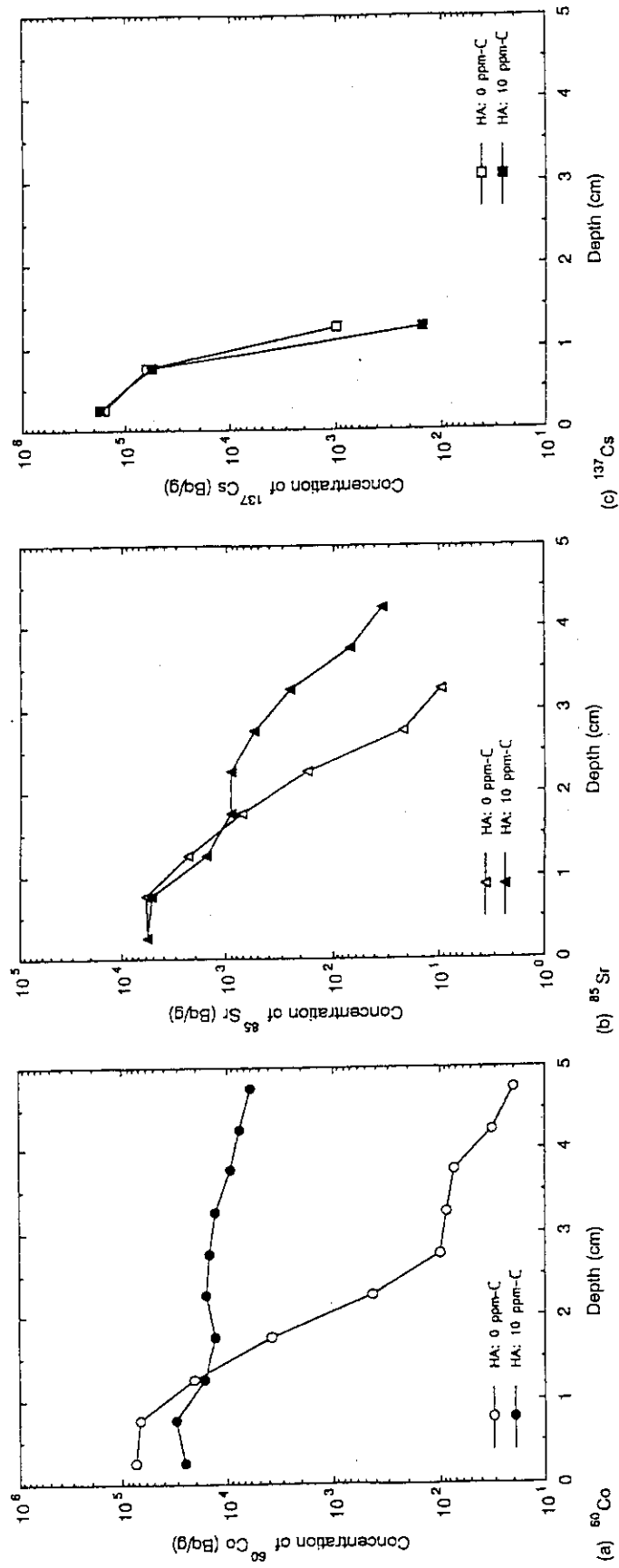


Fig. 3 Concentration profile of radionuclides in sandy soil layer.

2.1.4 Migration Behavior of Bicarbonate- ^{14}C in Underground Soil Layer

S. Nagao

1. Introduction

Carbon-14(^{14}C) occurs in nature, but is also formed at nuclear reactors. Because of its long half-life (5730 yr) and biological significance of carbon, releases from nuclear facilities could have a significant radiological impact. Low level radioactive waste management strategies for ^{14}C are therefore of current concern. The most likely mode of release of ^{14}C from a geologic repository is by aqueous leaching. Study on migration of ^{14}C in underground layer is important to evaluate feasibility of underground storage of radioactive wastes.

Column experiment is one of the analytical methods to study migration behavior of radionuclides in soil layer. This method can evaluate retardation ability of soil layer samples for radionuclides. The soil column experimental data of ^{14}C , however, was few reports (Allard et al., 1980, Igarashi et al., 1992). In many cases involving ^{14}C , considerable loss of ^{14}C in sample solutions takes place at acidic and neutral pH. Purpose of this study is to establish a simple closed column system for ^{14}C column experiments and applied to soil migration study of bicarbonate- ^{14}C , which its chemical form is major in low level radioactive waste.

2. Materials and Method

Glass beads with diameter range from 500~590 μm were used to check release from the column system during experiments because of low adsorption of bicarbonate- ^{14}C (distribution coefficient 0.4 ml/g). A tuffaceous sandy soil sample was collected at northwest part of Aomori Prefecture, Japan. Grain size distribution of the soil sample was 2.3% gravel, 81.2% sand, 11.2% silt, and 5.3% clay fractions.

A simple column system is shown in Fig. 1. Column is 2.5 cm in diameter and 5 cm in height. Gas bag is connected to the reservoir bottle to prevent release of ^{14}C from solution to atmosphere. Syringe is fitted with the reservoir bottle, and used to check variation of pH and radioactivity of ^{14}C in reservoir solution during column experiment.

Migration experiment was carried out as follows. The ^{14}C radioactive solution (about 60 Bq/ml) with pH 8.0 was continuously introduced to top of the column by a micro tube pump at constant flow rate (2 ml/min). The effluent was automatically collected into glass test tubes for 12.5 min with a fraction collector. The reservoir solution was collected with the syringe at regular intervals. The pH and ^{14}C radioactivity in effluent and reservoir solution samples were measured with a glass electrode and liquid scintillation counter, respectively. Tritiated water was also introduced into the soil column.

3. Results and Discussion

3.1 Glass beads column experiment

Radioactivity of ^{14}C and pH in reservoir solution are almost constant with time (Fig. 2). Radioactivity of ^{14}C in effluent from the column agrees with that of reservoir solutions above 23 ml effluent volume. The result indicates that ^{14}C column experiment can be performed without release of ^{14}C from radioactive solution by this simple column system. Increase of the effluent pH is considered to be release of alkali elements from glass beads.

3.2 Soil column experiment

^{14}C and pH in the effluent and reservoir solution are shown in Fig. 3. Decrease of radioactivity of ^{14}C in reservoir solution after the experiment is only 2.5% of initial value. Variation of pH of the reservoir ranges from 8.4 to 8.2. Bicarbonate- ^{14}C in reservoir solution is not released out to atmosphere. The radioactivity of ^{14}C in the effluent increases sharply with increasing outflow volume (until 200 ml), and gradually increases to 51 Bq/ml. This value is 12% lower than that of reservoir solutions. The effluent pH decreases from 7.6 to 7.2, and then increases to 7.6. Those values are lower than that of reservoir solutions.

Breakthrough curves of ^3H and ^{14}C are shown in Fig. 4. The C/Co estimate that the effluent concentration (C) is multiplied by average value (Co) of the reservoir solution. The ^{14}C is delayed to tritiated water, and exhibits retardation by the soil sample. The curves of ^{14}C by

the soil column experiments under same experimental condition are similar to each other (○ and □ in Fig. 4). The result indicates good reproducibility of the experiment at influent pH 8 by this column system. Difference in ^{14}C radioactivity between influent and effluent is observed for tuffaceous sandy soil samples. It is difficult to explain by release of ^{14}C for the experiment because of the result from the column experiment for the glass beads. The distribution coefficient (K_d value) of the soil sample, obtained by batch experiment, is about 100 ml/g. The lower ^{14}C value of the effluent, therefore, is considered to be due to adsorption of ^{14}C on the soil sample packed in the column.

References

- (1) B. Allard, B. Torstenfelt, K. Andersson: Sci. Basis Nucl. Waste Manage., III (1990) 465.
- (2) T. Igarashi, Y. Mahara, N. Matsuoka, E. Hirai, K. Nakai: 1992 Fall Meeting of the Atomic Energy Society of Japan (1992) 347.

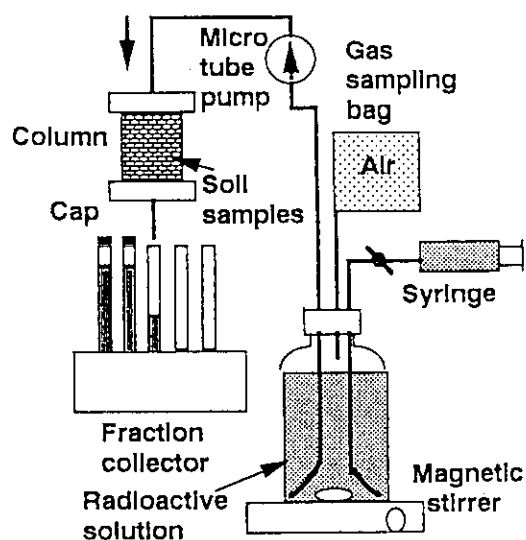


Fig. 1 Illustration of a simple column system.

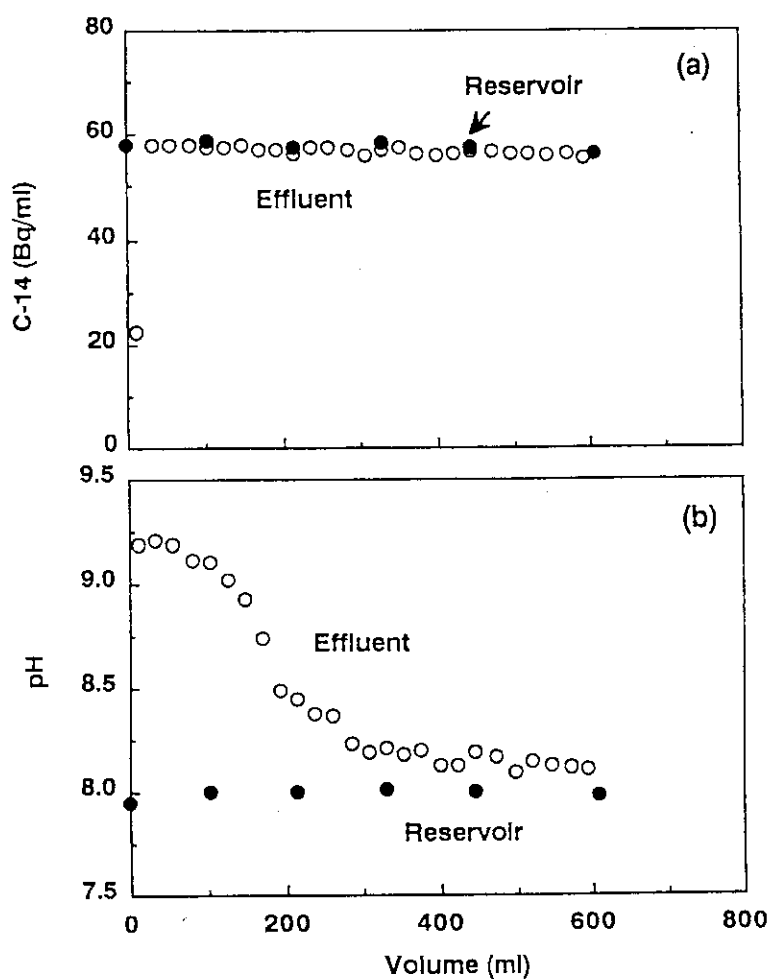


Fig. 2 The radioactivity of ^{14}C (a) and pH(b) in effluent from the column packed with glass beads. Open and closed circles indicate data for effluent and reservoir solution, respectively. Porosity of the column is 0.40.

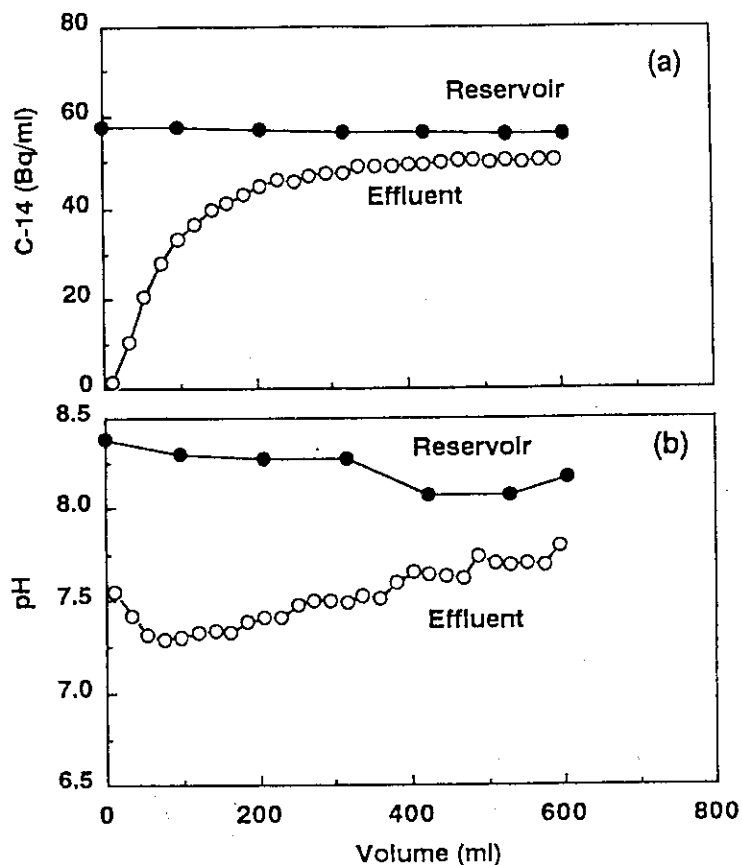


Fig. 3 The radioactivity of ^{14}C (a) and pH(b) in effluent from the column packed with the tuffaceous sandy soil. Open and closed circles indicate data for effluent and reservoir solution, respectively. Porosity of the column is 0.49.

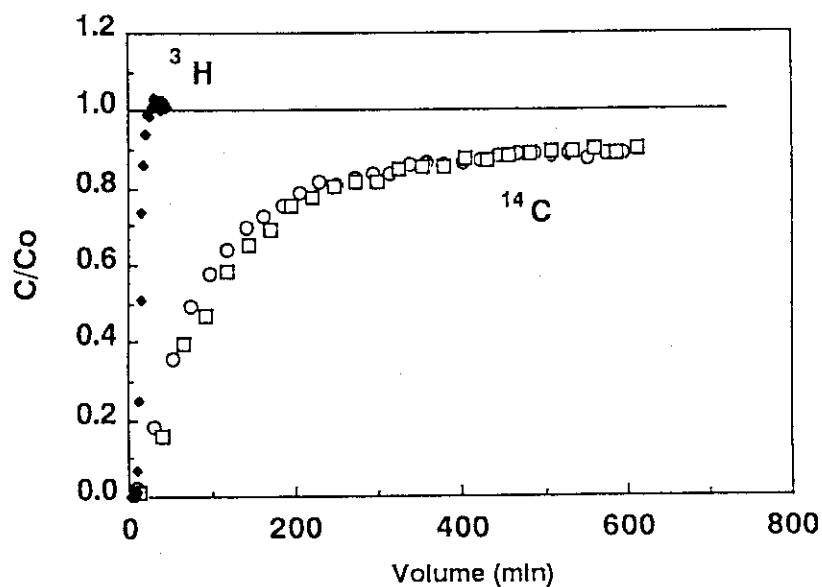


Fig. 4 The breakthrough curves of ^3H (\blacklozenge) and ^{14}C (\circ , \square) from soil

3. Safety Evaluation Study on Geological Disposal

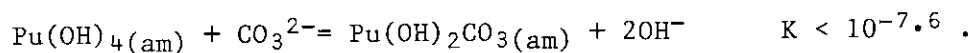
3.1 Chemical Behavior of Radionuclides in Water

3.1.1 Effect of Complexation on Solubility of Pu(IV) in Aqueous Carbonate System

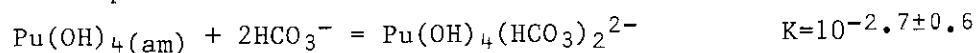
T. Yamaguchi and Y. Sakamoto

Abstract

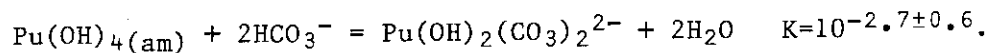
Solubility of Pu(IV) was measured under the total carbonate concentration range of $10^{-4} \sim 1 \times 10^{-1}$ M. Since carbonate was not detected from the solid phase, the solubility controlling solid was concluded to be a hydroxide, $\text{Pu(OH)}_4(\text{am})$. The equilibrium constant of the exchange reaction between $\text{Pu(OH)}_4(\text{am})$ and another possible solid phase, $\text{Pu(OH)}_2\text{CO}_3(\text{am})$ was estimated as:



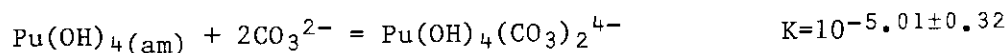
The solubility was proportional to the square of the bicarbonate concentration at pHs 9.4, 9.7 and 10.1. This result was interpreted by either



or



At pHs 12 and 13 where carbonate ion is dominant,



is the predominant reaction.

1. Introduction

The solubility of radionuclides is one of the important parameters controlling their release from deep underground radioactive waste repository. Prediction of the solubility requires the knowledge of all relevant species present in solution. Complexation of metal ions with ligands often stabilizes some of them in natural water, and thus complexation

This article was presented at Fourth International Conference on the Chemistry and Migration Behavior of Actinides and Fission Products in the Geosphere (MIGRATION '93) at Charleston, SC, USA December 12-17, 1993, and will be published in Radiochim. Acta.

could largely control the speciation and solubility of radionuclides of interest. Because of the strong tendency of complexation, carbonate or bicarbonate ions appear the most significant ligand to be considered for complexation^(1,2). Clearer understanding of the effect of carbonate complexation on solubility is needed.

The complexation of Pu(IV) by carbonate has been discussed in a few papers^(3,4,5). Moskvina and Gel'man⁽³⁾ have shown that the carbonate complex species, $\text{Pu}(\text{CO}_3)_2^{2+}$, was present in 0.36 ~ 3.6 M K_2CO_3 solutions. Their work, however, has been reviewed critically^(5,6), and some misunderstandings have been pointed out. Kim et al.⁽⁴⁾ suggested that $\text{Pu}(\text{CO}_3)_x^{4-2x}$ ($x = 1 \sim 5$) are the dominant aqueous species with the solubility-controlling solid of $\text{Pu}(\text{OH})_2\text{CO}_3(\text{s})$ in NaClO_4 / NaHCO_3 / Na_2CO_3 solution at $\text{pH} > 8$ and $I = 1.0$. Recently, Pratopo et al.⁽⁷⁾ studied the carbonate complexation of Np(IV) by a solubility method and suggested the presence of $\text{Np}(\text{OH})_2(\text{CO}_3)_2^{2-}$ (or $\text{Np}(\text{OH})_4(\text{HCO}_3)_2^{2-}$) and $\text{Np}(\text{OH})_4(\text{CO}_3)_2^{4-}$. They also analyzed the concentration of U(IV) in Swedish ground-water by taking into account of the presence of $\text{U}(\text{OH})_2(\text{CO}_3)_2^{2-}$.

Despite that the chemical properties of tetravalent actinides are expected to be similar, there are certain discrepancies among the data on their complexation. Considering the critical role of the complex species in safety assessment of radioactive waste disposal, much more reliable information is necessary. In the present study, the Pu(IV) solid phase was characterized and the carbonate-bicarbonate concentration dependence of Pu(IV) solubility was studied at the pH range of 9.4 ~ 13.

2. Experimental

2.1 Preparations

Sample solutions were prepared from reagent grade chemicals (Wako Pure Chemical Ind., Ltd., Tokyo) and deionized water (Milli-Q System, Millipore). The isotopic composition of used plutonium was 0.0031% ^{238}Pu , 97.41% ^{239}Pu , 2.56% ^{240}Pu and 0.026% ^{241}Pu . Plutonium was chemically purified by anion exchange. The eluted Pu in hydrochloric acid was converted to nitrate. The Pu concentration in 10 M HNO_3 stock solution was 1.8×10^{-4} M.

2.2 Procedures

An aliquot of Pu(IV) stock solution was spiked into a 20 ml KCl / K_2CO_3 / KOH solution in a polypropylene tube. The initial concentration of Pu(IV), K^+ and total carbonate (C_t) in the sample solution were 1.3×10^{-6} , 0.1 and $10^{-4} \sim 2 \times 10^{-2}$ M, respectively. A small amount of 0.1 M NaNO_2 was added to control the redox condition. The pH was adjusted between 9.4 and 13.0 by a dilute KOH solution. The samples were sealed and stored for 2 weeks in the aerated atmosphere.

After two-week storage, the pH and Eh of the sample solutions were measured with AgCl electrodes. An aliquot (2 ml) of the sample solution was pipetted to measure the total carbonate concentration with CO_2 electrode (TOA Electronics Ltd. Japan, type CE-235, detection limit: 4.0×10^{-5} M). A 0.5 ml aliquot of the sample solution was filtered to separate the aqueous solution from any solid phase. Filters of two different pore sizes, 0.45 μm and 10,000 NMWL (nominal molecular weight limit), were used. The average pore size was estimated to be about 450nm and 3nm, respectively. The concentration of Pu was measured with α spectroscopy after evaporating 50 μl of final filtrate on a stainless steel planchet. Oxidation state of Pu was determined by applying TTA extraction technique⁽⁷⁻⁹⁾ to a 100 μl aliquot of the final filtrate.

Plutonium solid formed in a few samples were provided for characterization. The initial concentration of Pu(IV), pH and C_t in these samples were 1.0×10^{-4} M, 9.65 ~ 9.85, and 0.01 ~ 0.1 M, respectively. The solid phase was trapped on the 0.45 μm filter and rinsed 3 times with 1 ml of deionized water. The solid phase was then dissolved in 2 ml of 1 M H_2SO_4 . The concentration of carbonate and plutonium dissolved from the solid was measured with the CO_2 electrode and α spectrometer, respectively. To prevent the disturbance on the carbonate measurement by acidic gas, fixed acid (H_2SO_4) was used to dissolve the solid. In the case that 1M H_2SO_4 was used for acidification, the detection limit was 6×10^{-5} M.

To justify this method, a preliminary test was carried out using cobalt (Co^{2+}) in place of plutonium. Cobalt was chosen because both hydroxide and carbonate precipitates can be easily prepared. A cobalt precipitate was prepared from CoCl_2 solution with an addition of NaHCO_3 at pH = 8.0 and C_t = 0.1 M. The amount of cobalt was varied from 24 to 120 μg . Precipitates were also prepared in 0.1 M Na_2CO_3 at pH = 11.0 and 0.1 M NaClO_4 at pH = 11.0 for comparison.

3. Results and Discussion

3.1 Cobalt test

Cobalt forms $\text{Co(OH)}_2(\text{s})$ ($\log K_{\text{sp}} = -15.2^{(10)}$) in alkaline solutions and $\text{CoCO}_3(\text{s})$ ($\log K_{\text{sp}} = -9.98^{(11)}$) in carbonate solutions. A purple precipitate was formed in NaHCO_3 solution ($\text{pH} = 8.0$). Cobalt carbonate may be formed by the following reaction



A blue-green colored precipitate was formed in Na_2CO_3 solutions ($\text{pH} = 11.0$) and 0.1 M NaClO_4 solution ($\text{pH} = 11.0$). Cobalt hydroxide may be formed by the following reaction

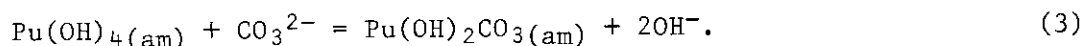


The result of carbonate content measurements for the cobalt precipitates is shown in Table 1. The measured carbonate morality at $\text{pH} = 8$ is almost equal to that of cobalt. At $\text{pH} = 11$, on the other hand, the measured carbonate morality is much less than that of cobalt. This result indicates that carbonate in precipitates can be successfully determined; whether the plutonium precipitate is carbonate or not can be determined in this method. About 10% error in measurements is accompanied, which possibly results from incomplete separation and rinse of the solid. Detection limit of this determination is considered to be 0.1 mM .

3.2 Characterization of plutonium solid phase

In carbonate solutions, the formation of $\text{Pu(OH)}_2\text{CO}_3(\text{am})$ as well as $\text{Pu(OH)}_4(\text{am})$ is inferred. Table 2 shows the results of carbonate content measurements of Pu(IV) solid phase. Even in the 0.1 M KHCO_3 solution, the carbonate content was under the detection limit (0.1 mM). The dominant solid phase was not hydroxycarbonate. The formation of hydroxide precipitation is most probable.

Our results do not agree with the previous predictions^(4,5) in which the formation of solid phase of $\text{Pu(OH)}_2\text{CO}_3(\text{am})$ in place of $\text{Pu(OH)}_4(\text{am})$ was suggested in a solution of $> 10^{-4} \text{ M}$ carbonate:

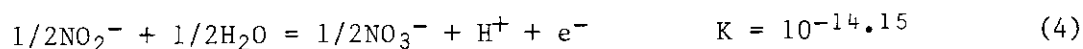


In the present study, the mole fraction of $\text{Pu(OH)}_4(\text{am})$ and $\text{Pu(OH)}_2\text{CO}_3(\text{am})$ were > 0.9 and < 0.1 , respectively. The equilibrium constant of eq. (3) was estimated to be $K < 10^{-7.6}$ by using the ratio of the mole fraction between the solid phases in place of their activity ratio. With the reported solubility product of $\text{Pu(OH)}_4(\text{am})$, $\log K_{\text{sp}} = -56.85^{(12)}$, K_{sp} of $\text{Pu(OH)}_2\text{CO}_3(\text{am})$ can be estimated to be $> 10^{-49.2}$.

3.3 Stability constant of Pu(IV) hydroxycarbonate complexes

Carbonate concentrations in the range of $10^{-4} \sim 0.5$ M were kept approximately constant for about 100 days under the employed experimental condition as seen in Fig. 1. A sample of the concentration as low as 10^{-5} M was affected by the atmospheric CO_2 .

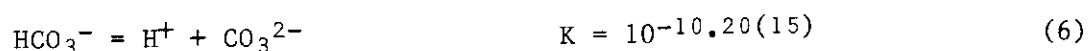
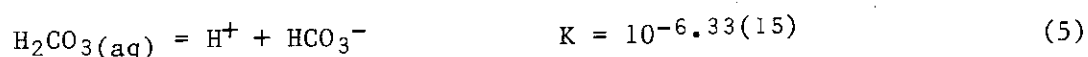
Figure 2 shows the redox potential of the sample solutions for the different pHs. The following reaction is likely to control the redox condition of the sample solutions.



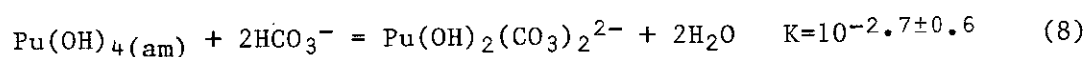
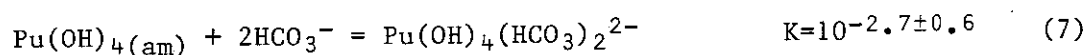
Under the condition, it was confirmed by TTA extraction that plutonium was mainly in the tetravalent state. Because Pu fraction remained on a filter was less by one order than that in the final filtrate, colloidal plutonium was less significant.

A series of solubility measurements was carried out at pHs 9.4, 10.1, 13 from oversaturation direction to determine the time required for equilibrium. As shown in Fig. 3, the Pu concentrations reach equilibrium within the first 14 days through oversaturation direction. Total carbonate concentration of a sample of pH 10.1 was increased at the 14th day with additions of KHCO_3 and K_2CO_3 . The solid phase began dissolving and it took 100 days to reach a different equilibrium concentration. This result implies that longer equilibration time is necessary through undersaturation direction than through oversaturation direction. An equilibration period of 14 days and the oversaturation direction were chosen for the present study. Considering that the solid phase will proceed to crystallize, the equilibrium state discussed here may be a pseudo equilibrium state.

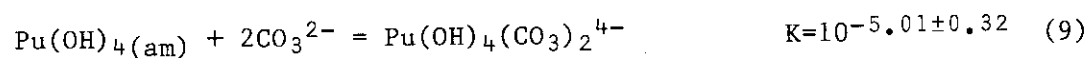
The measured solubility of Pu(IV) is shown in Fig. 4. In low carbonate solutions, an aqueous neutral species of $\text{Pu}(\text{OH})_4^0$ is dominant, whose solubility was reported by Ewart et al.⁽¹³⁾. The solubility measured at $C_t > 10^{-4}$ M is far higher than that of $\text{Pu}(\text{OH})_4^0$, which is due to complexation. Although chloride anion is the main anionic species in sample solutions, the complex formation of Pu(IV) by Cl^- is negligible according to the predicted formation constant⁽¹⁴⁾. Carbonate and bicarbonate concentrations were calculated from C_t and the dissociation constants reported as follows:



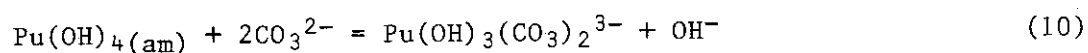
Because bicarbonate ion is dominant in our pH range of 9.4 ~ 10.1, the measured Pu concentrations are plotted versus $[\text{HCO}_3^-]$. The Pu solubility depends on bicarbonate concentration in this pH range; $\log[\text{Pu(IV)}]$ is proportional to $\log[\text{HCO}_3^-]$ with the slope of 2. Hence we considered that either of the reaction (7) or (8).



Carbonate ion dominates in the higher pH range, in place of bicarbonate. At pH = 12 and 13, the solubility is proportional to the square of the carbonate concentrations and interpreted by reaction (9).



Since the data at pH 12 are almost the same as those at pH 13, the following reaction that depends on pH can be ruled out.



Together with the solubility products of Rai et al.⁽¹²⁾, the stability constants of $\text{Pu}(\text{OH})_2(\text{CO}_3)_2^{2-}$ and $\text{Pu}(\text{OH})_4(\text{CO}_3)_2^{4-}$ are calculated to be $10^{46.4 \pm 0.7}$ and $10^{51.85 \pm 0.48}$, respectively. The stability constants of

hydroxycarbonate complex species are tabulated in Table 3.

It is noticeable that the present interpretation for Pu(IV) carbonates is similar to that for Np(IV) carbonates⁽⁷⁾. The formation of $\text{Pu}(\text{CO}_3)_x^{4-2x}$ ($x = 1 \sim 5$) and $\text{Pu}(\text{OH})_2\text{CO}_3(\text{s})$, both of which have been predicted by Kim et al.⁽⁴⁾ and Lierse⁽⁵⁾, were not consistent with implications from our experimental results. The previous solubility data^(4,5) can be interpreted by reactions (7), (8) and (9). The Eh-pH diagram calculated by using the present data and data compiled in a reference⁽¹⁷⁾ is shown in Fig. 5. The diagram is different from the previous ones^(18,19), in which the formation of hydroxycarbonate species have not been taken into account.

4. Conclusion

The Pu solid phase formed in the present solubility experiments is likely to be $\text{Pu}(\text{OH})_4(\text{am})$. Carbonate and bicarbonate have significant effect on the solubility of Pu(IV). Species of $\text{Pu}(\text{OH})_2(\text{CO}_3)_2^{2-}$ or $\text{Pu}(\text{OH})_4(\text{HCO}_3)_2^{2-}$ is predominant in bicarbonate solutions, while species of $\text{Pu}(\text{OH})_4(\text{CO}_3)_2^{4-}$ is responsible for the solubility in carbonate solutions.

Acknowledgement

The authors would like to express our appreciation to Dr. S. Nakayama for helpful discussions. Dr. N. Kohno is also acknowledged for the Pu preparation.

References

- (1) Kim, J.I., in: *Handbook on the Physics and Chemistry of the Actinides* (Freeman, A.J. and Keller, C., eds.) Vol.4, North Holland, Amsterdam 1986, p.413.
- (2) Newton, T.W., Sullivan, J.C., *Handbook on the Physics and Chemistry of the Actinides* (Freeman, A.J. and Keller, C., eds.) Vol.3, North Holland, Amsterdam 1985, p.387.

- (3) Moskvín, A.I., Gel'man, A.D.: Determination of the Composition and Instability Constants of Oxalate and Carbonate Complexes of Plutonium(IV), *Russ. Jour. Inorg. Chem. (Engl. Transl.)* 3, 198 (1958).
- (4) Kim, J.I., Lierse, Ch., Baumgärtner, F.: Complexation of the Plutonium(IV) Ion in Carbonate-Bicarbonate Solutions, Chapter 21, in: *Plutonium Chemistry* (Carnall, W.T., Choppin, G.R. eds.) ACS Symp. Ser. 216, Amer. Chem. Soc., Washington, D.C. 1983, p.317.
- (5) Lierse, Ch.: *Chemical Behavior of Plutonium in Natural Aquatic System: Hydrolysis, Carbonate Complexation and Redox Reaction*, Ph. D. Thesis, Technische Universität München, München, (in Germany) 1985.
- (6) Pulgdomènech, I., Bruno J.: Plutonium Solubility, SKB-TR--91-04, SKBF/KBS, Stockholm 1991.
- (7) Pratopo, M.I., Moriyama, H., Higashi, K.: Carbonate Complexation of Neptunium(IV) and Analogous Complexation of Ground-Water Uranium, *Radiochim. Acta* 51, 27 (1990).
- (8) Foti, S.C., Freiling, E.C.: The Determination of the Oxidation States of Tracer Uranium, Neptunium and Plutonium in Aqueous Media, *Talanta* 11, 385 (1964).
- (9) Nitsche, H., Lee, S.C., Gatti, R.C.: Determination of Plutonium Oxidation States at Trace Levels Pertinent to Nuclear Waste Disposal, *J. Radioanal. Chem.* 124, 171 (1988).
- (10) *Stability Constants of Metal-Ion Complexes, Supplement No.1 (Chemical Soc. Special Publication, No.25)*, Chemical Soc., London 1971, p.12.
- (11) Bjerrum, J.: *Stability Constants of Metal-Ion Complexes, with Solubility Products of Inorganic Substances, PART 2 (Special Publication)* Chemical Soc., London 1958, p.77.
- (12) Rai, D.: Solubility Product of Pu(IV) Hydrous Oxide and Equilibrium Constants of Pu(IV)/Pu(V), Pu(IV)/Pu(VI) and Pu(V)/Pu(VI) Couples, *Radiochim. Acta* 35, 97 (1984).
- (13) Ewart, F.T., Howse, R.M., Thomason, H.P., Williams, S.J., Cross, J.E.: The Solubility of Actinides in the Near-Field., in: *Sci. Basis Nucl. Waste Manag. IX* (Werme. L.O., ed), Mater. Res. Soc., Pittsburgh, Pennsylvania, 1985, p.701.
- (14) Brown, P.L., Wanner, H., in: *Predicted Formation Constants Using the Unified Theory of Metal Ion Complexation*, OECD-NEA, Paris 1986, p.60.
- (15) MacInnes, D.A., Belcher, D.: The Thermodynamic Ionization Constants of Carbonic Acid, *J. Am. Chem. Soc.* 55, 2630 (1933).

- (16) Pratopo, M.I., Moriyama, H., Higashi, K.: The Behavior of Neptunium under Reducing Conditions, Proceedings of the 1989 Joint International Waste Management Conference, Vol.2, p.309 (1989).
- (17) Yamaguchi, T., Pratopo, M.I., Moriyama, H., Higashi, K.: Adsorption of Cesium and Neptunium(V) on Bentonite, Proceedings of the Third International Conference on Nuclear Fuel Reprocessing and Waste Management (RECOD'91), Sendai, Japan, Vol.2, p.999 (1991).
- (18) Skytte Jensen, B.: The Geochemistry of Radionuclides with Long Half-Lives, Risø-R-430 (Risø Nat. Lab.) 1980.
- (19) Bennett, D.A.: *Stability Constants Important to the Understanding of Plutonium in Environmental Waters-Hydroxy and Carbonate Complexation of PuO_2^+* , Ph. D. Thesis, University of California, Berkeley 1990.

Table 1 Carbonate content analysis for cobalt precipitates

Co μg	condition of precipitation	solid	[Co] ^(a) mM	$\Sigma [\text{CO}_2]$ ^(b) mM
24	0.1M NaHCO ₃ (pH=8)	CoCO ₃	0.2	0.23
48	0.1M NaHCO ₃ (pH=8)	CoCO ₃	0.4	0.40
72	0.1M NaHCO ₃ (pH=8)	CoCO ₃	0.6	0.66
96	0.1M NaHCO ₃ (pH=8)	CoCO ₃	0.8	0.84
120	0.1M NaHCO ₃ (pH=8)	CoCO ₃	1.0	0.98
120	0.1M Na ₂ CO ₃ (pH=11)	Co(OH) ₂	1.0	0.09
120	0.1M Na ₂ CO ₃ (pH=11)	Co(OH) ₂	1.0	0.11
120	0.1M Na ₂ CO ₃ (pH=11)	Co(OH) ₂	1.0	0.11
120	0.1M NaClO ₄ (pH=11)	Co(OH) ₂	1.0	< 0.06
120	0.1M NaClO ₄ (pH=11)	Co(OH) ₂	1.0	< 0.06
120	0.1M NaClO ₄ (pH=11)	Co(OH) ₂	1.0	< 0.06

(a) assuming that all the cobalt was dissolved in 1 M H₂SO₄(b) carbonate concentration measured in 1 M H₂SO₄

Table 2 Carbonate content in Pu solid phase

Pu μg	condition of precipitation	[Pu] mM	$\Sigma [\text{CO}_2]$ mM
500	0.01M KHCO ₃ (pH=9.65)	1.0	< 0.1
500	0.03M KHCO ₃ (pH=9.82)	1.0	< 0.1
500	0.1M KHCO ₃ (pH=9.85)	1.0	< 0.1

Table 3 Equilibrium constant of An(IV) hydrolysis and carbonate species

reaction	log K	log stability constant of product ^(a)
$\text{Pu}(\text{OH})_4(\text{am}) + 2\text{HCO}_3^- = \text{Pu}(\text{OH})_2(\text{CO}_3)_2^{2-} + 2\text{H}_2\text{O}$	-2.7 ± 0.6	46.4 ± 0.7
$\text{Pu}(\text{OH})_4(\text{am}) + 2\text{HCO}_3^- = \text{Pu}(\text{OH})_4(\text{HCO}_3)_2^{2-}$	-2.7 ± 0.6	53.43 ± 0.7
$\text{Pu}(\text{OH})_4(\text{am}) + 2\text{CO}_3^{2-} = \text{Pu}(\text{OH})_4(\text{CO}_3)_2^{4-}$	-5.01 ± 0.32	51.84 ± 0.48
$\text{Pu}(\text{OH})_4(\text{am}) = \text{Pu}(\text{OH})_4^0$	-10.14 ± 0.28 [13]	46.71 ± 0.46
$\text{Pu}^{4+} + 4\text{OH}^- = \text{Pu}(\text{OH})_4(\text{am})$	56.85 ± 0.36 [12]	-
$\text{Pu}^{4+} + 2\text{OH}^- + \text{CO}_3^{2-} = \text{Pu}(\text{OH})_2(\text{CO}_3)(\text{am})$	<49.2	-
$\text{Np}(\text{OH})_4(\text{am}) + 2\text{HCO}_3^- = \text{Np}(\text{OH})_2(\text{CO}_3)_2^{2-} + 2\text{H}_2\text{O}$	-0.35 ± 0.33 [7]	45.69 ± 0.44 [7]
$\text{Np}(\text{OH})_4(\text{am}) + 2\text{HCO}_3^- = \text{Np}(\text{OH})_4(\text{HCO}_3)_2^{2-}$	-0.35 ± 0.33 [7]	54.14 ± 0.44 [7]
$\text{Np}(\text{OH})_4(\text{am}) + 2\text{CO}_3^{2-} = \text{Np}(\text{OH})_4(\text{CO}_3)_2^{4-}$	-1.43 ± 0.33 [7]	53.07 ± 0.44 [7]
$\text{Np}(\text{OH})_4(\text{am}) = \text{Np}(\text{OH})_4^0$	-8.5 ± 0.1 [16]	46.0 ± 0.3
$\text{Np}^{4+} + 4\text{OH}^- = \text{Np}(\text{OH})_4(\text{am})$	54.5 ± 0.3 [12]	-
$\text{U}(\text{OH})_4(\text{am}) + 2\text{HCO}_3^- = \text{U}(\text{OH})_2(\text{CO}_3)_2^{2-} + 2\text{H}_2\text{O}$	>-2.44 [7]	>41.7 [7]

(a) Solubility products of $[\text{An}^{4+}][\text{OH}^-]^4$ taken from ref. [12] were used for calculation.

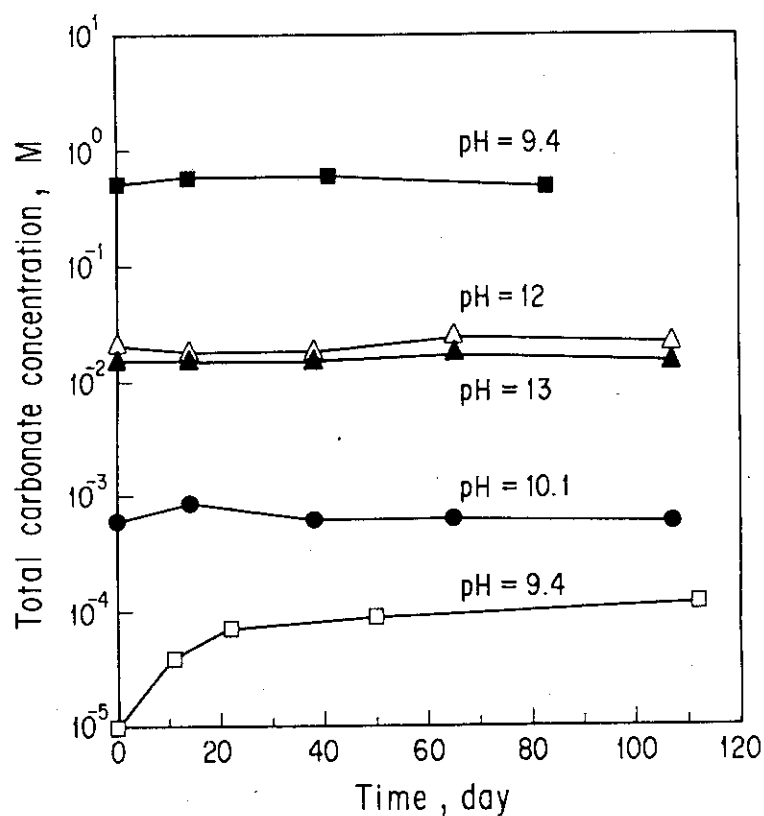


Fig. 1 Time dependence of total carbonate concentrations for $10^{-5} \sim 0.5$ M $\text{KHCO}_3/\text{K}_2\text{CO}_3$ solutions in the pH range of 9.4 ~ 13.

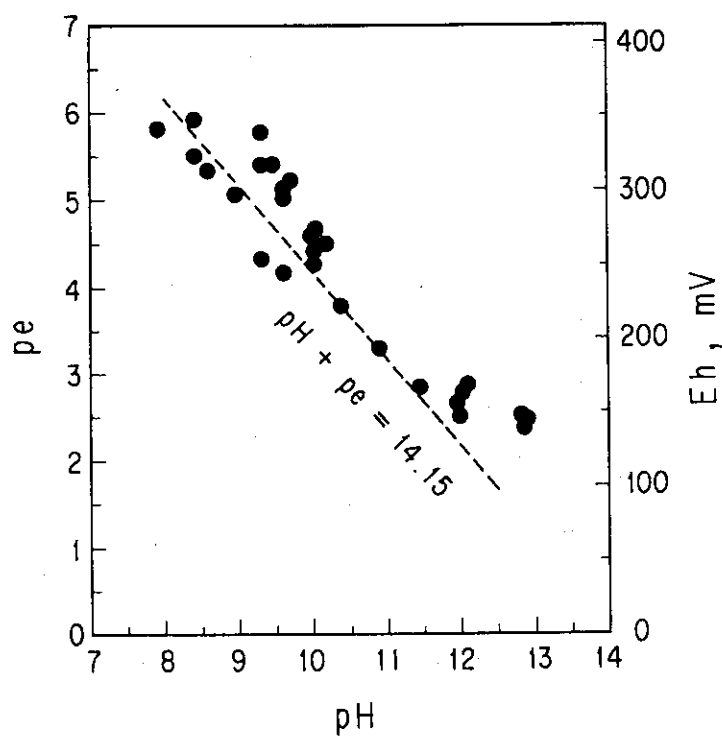


Fig. 2 Measured redox potential versus pH values for the Pu(IV) carbonate-bicarbonate solutions with NaNO_2 . The line corresponds to eq. (4).

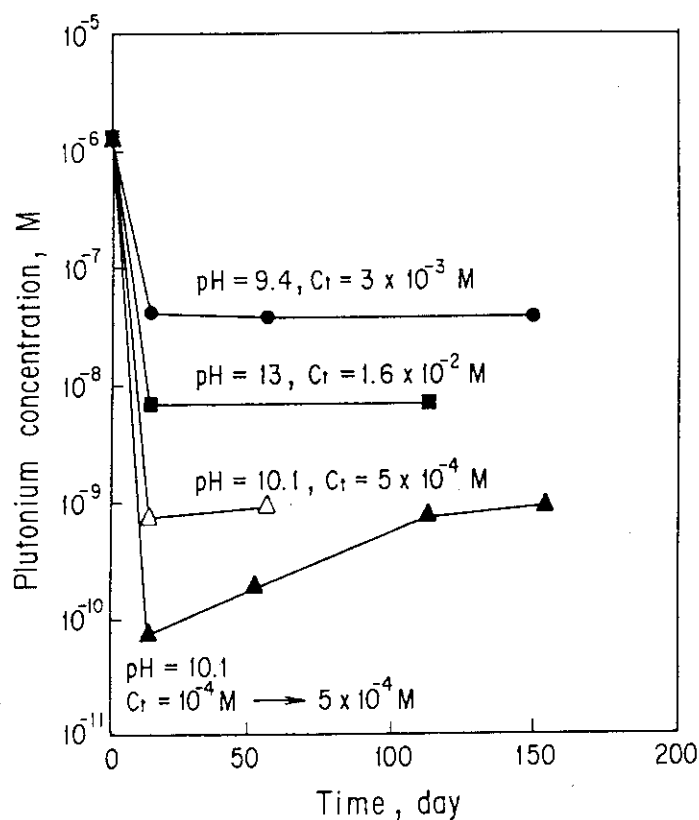


Fig. 3 Equilibration of plutonium(IV) concentrations for $10^{-4} \sim 1.6 \times 10^{-2}$ M $\text{KHCO}_3/\text{K}_2\text{CO}_3$ solutions in the pH range of 9.4 ~ 13; \bullet , \blacksquare , \triangle : oversaturation, \blacktriangle : undersaturation.

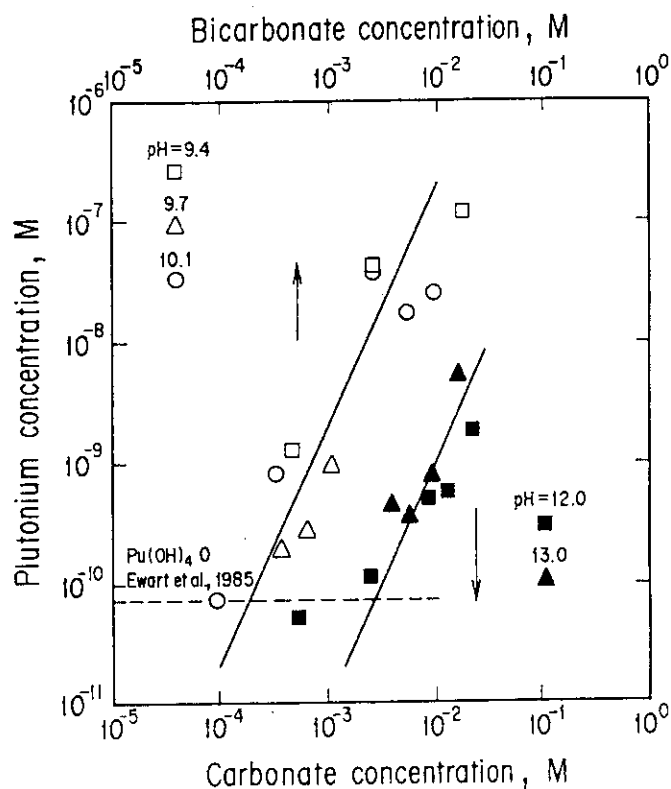


Fig. 4 Effect of bicarbonate concentration on solubility of Pu(IV) at pH=9.4, 9.7 and 10.1, and effect of carbonate concentration at pH 11 and 12.

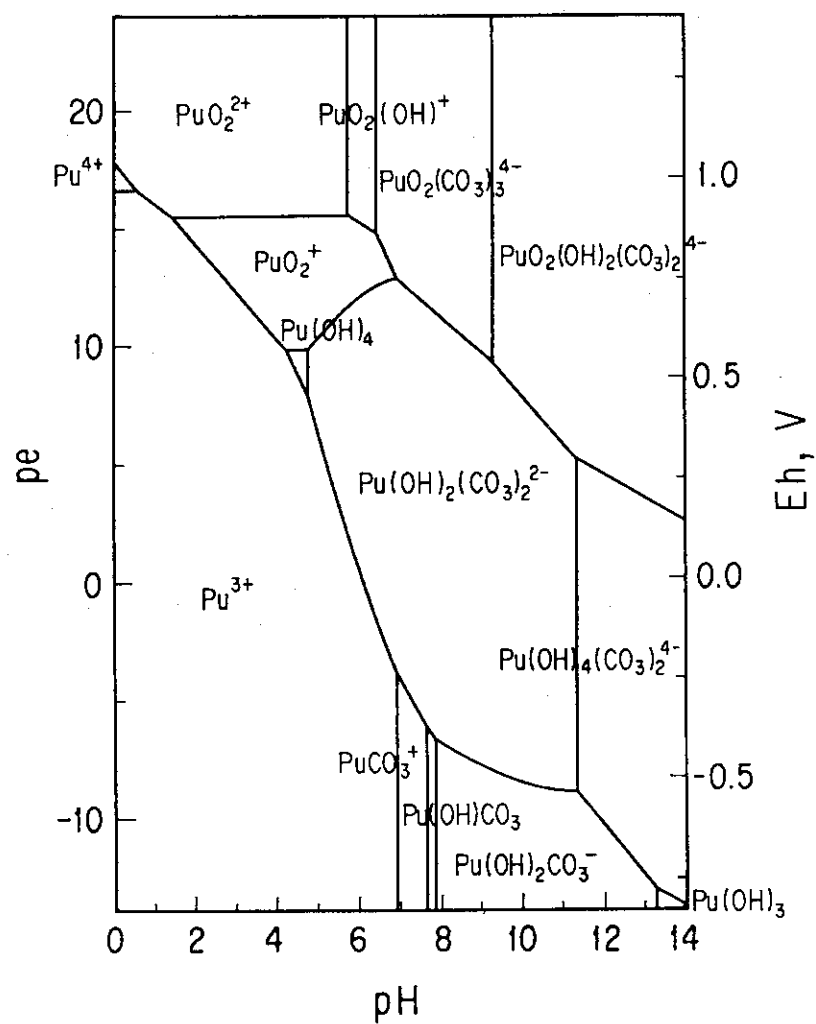


Fig. 5 Eh-pH diagram of Pu; total carbonate concentration: 4×10^{-3} M.

3.2 Nuclide Migration and Retardation

3.2.1 Redistribution of Neptunium(V) during the Crystallization of Amorphous Ferrihydrite

Y. Sakamoto

Introduction

In an engineered barrier for high level radioactive waste, a large amount of iron corrosion products will be produced by a canister and overpack after long term emplacement of the waste glass. Radionuclides released from waste glass will be sorbed on amorphous or crystalline iron compounds in the engineered barrier. If amorphous iron compounds are transferred into crystalline one after radionuclides are sorbed on them, the radionuclides will be redistributed on the crystalline one. Consequently, it is important to study the redistribution behavior of radionuclides during the alteration of iron compounds.

The neptunium(V) sorption experiment was conducted under the crystallization from amorphous iron ferrihydrite to a mixture of crystalline goethite and hematite. After sorption experiment, a sequential extraction was applied to study a degree of association between neptunium and iron compounds.

Experimental

Solution of iron(III) nitrate with the concentration of 0.2 M was prepared in a beaker. The solution pH was adjusted to 7.7 with 5 M and 1 M sodium hydroxide solutions to make the amorphous iron(III) hydroxide precipitates. Each 10 ml of the suspensions was transferred to polyethylene centrifugation tubes. The iron(III) precipitates were centrifuge-washed three times with deionized water.

^{237}Np sorption experiment was conducted under the coexistence of the crystallization of amorphous ferrihydrite(dynamic condition). Neptunium nitrate solution with 5×10^{-6} mol/L was made in 0.03 M sodium perchlorate solution. The solution pH was adjusted to 7.7 as same condition of the above iron(III) precipitation. The neptunium(V) solutions of 10 ml were subdivided into each above centrifugation tubes including the amorphous

precipitates. They were kept at 90°C in a thermostatic oven for prescribed time. After the aging them, the supernatant was filtrated with 0.45 µm Millipore Millex filter. The ^{237}Np radioactivity concentration in the solution was measured with a liquid scintillation counter. A percentage sorption fraction of neptunium(V) onto iron precipitates was calculated from a difference in the concentrations before and after sorption experiment.

The ^{237}Np sorbed on the iron precipitates was sequentially extracted with following four steps;

(1) MgCl fraction

The precipitate was extracted at room temperature for 1 hour with 10 ml of magnesium chloride solution (1M MgCl_2 , pH 7).

(2) NH_2OH fraction

The precipitate from fraction (1) was extracted with 10 ml of 0.04 M $\text{NH}_2\text{OH}\cdot\text{HCl}$ in 25% acetic acid solution at 90°C for 5 hours.

(3) 1N HCl fraction

The precipitate from fraction (2) was extracted with 10 ml of 1N HCl solution for 24 hours.

(4) 6N HCl fraction

The residue from fraction (3) was digested with 10 ml of 6N HCl solution.

To determine a crystallinity of the iron(III) precipitate, a "cold" experiment without neptunium(V) was carried out in parallel with above "hot" sorption experiment. The iron(III) precipitates aged for the prescribed time were washed with deionized water and dried with a freeze dryer. The dried solid products were crashed with an agate mortar. The content of crystalline hematite/goethite in the precipitate was measured by an X-ray analysis. A crystallinity in percentage for each precipitate was determined from relative value for saturated peak height that was defined as 100% crystallinity.

The static sorption experiment(static condition) without coexistence of the crystallization was also performed with the iron(III) precipitates of the 0 and 100% crystallinity, to compare the sorption behavior of neptunium(V) with one of the dynamic condition.

Results and Discussion

Time dependence of the crystallization of the amorphous ferrihydrite to the crystalline hematite/goethite was shown in Fig. 1(a). The crystallinity was achieved 100% for about 50 hours. The solution pH during the sorption experiment is also illustrated in Fig. 1(b). The pH was constant as 7.7 during the experiment. The neptunium(V) sorption behavior is closely related to the solution pH because a chemical form of neptunium(V) and a surface charge of solid are obeyed by the solution pH. At pH 7.7, a chemical form of neptunium(V) is estimated as NpO_2^+ under this condition (pH 7.7 at 90°C)⁽¹⁾. Then, the apparent sorption fraction during the crystallization changes with a difference in the sorption fraction of neptunium(V) on amorphous ferrihydrite and hematite/goethite. Under the static condition, the sorption fraction of neptunium(V) on the iron(III) precipitates with 0 and 100% crystallinity was about 100%. From this result, it is expected that the sorption fraction of neptunium(V) is constant during the crystallization. The sorption fraction under the dynamic condition is illustrated in Fig. 1(a). It was apparently constant during the sorption experiment as expected from the result under the static condition.

Figure 2 shows also the time dependence of a relative distribution for neptunium(V) in the sequential extraction. Under the dynamic condition, the MgCl fraction decreased with the crystallization, on the contrary, the 6N HCl fraction increased. Figure 3 shows the relative distributions for the sample with the 100% crystallinity under the static and dynamic condition. In the static condition, most of the fraction was 1N HCl and NH₂OH fraction. A treatment in the 1N HCl and NH₂OH fraction dissolves the amorphous ferrihydrite and extracts the sorbed, complexed elements on the iron compounds⁽²⁾. Then, it is likely that neptunium(V) sorption is controlled by relatively strong force like specific adsorption under the static condition. On the other hand, main fraction under the dynamic condition is the one of 6N HCl and it increased with the crystallization. Then, from the results in Fig. 2 and 3, the crystallization of the amorphous ferrihydrite yielded the 6N HCl fraction in the distribution of neptunium(V). Because the sorbed and complexed neptunium(V) on the surface of the hematite/goethite had been eliminated in the NH₂OH and 1N HCl fraction, it is supposed that neptunium(V) in the 6N HCl fraction was produced by an incorporation of neptunium(V) once sorbed on

the amorphous ferrihydrite into the crystalline hematite/goethite during the crystallization.

Conclusion

Under the dynamic condition with coexistence of the crystallization, the apparent sorption fraction was constant during the crystallization, but the sorption form of neptunium(V) was transferred into the incorporated one into the crystalline iron(III) compounds.

References

- (1) J.C. Sullivan, Calorimetric studies of NpO_2^+ hydrolysis, *Radiochimica Acta*, Vol.54, 17(1991).
- (2) H. Agemian and A.S.Y. Chau, Evaluation of extraction techniques for the determination of metals in aquatic sediments, *The Analyst*, Vol.101, No.1207, 761(1976).

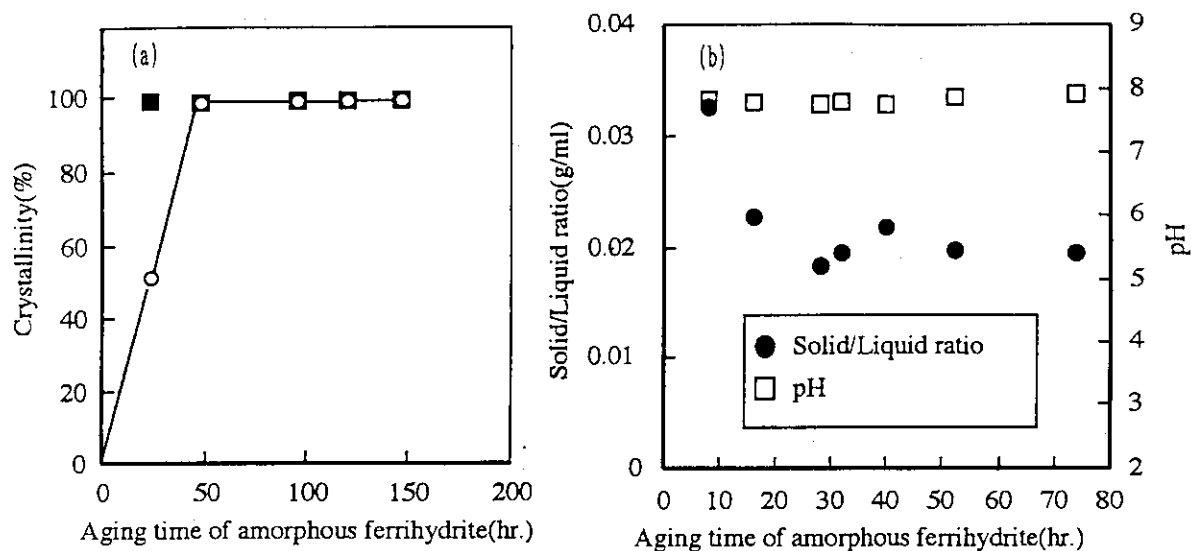


Fig. 1 (a) Time dependence of the crystallinity of the iron(III) precipitate and sorption fraction of Np during the crystallization.

(b) Time dependence of the solution pH and the solid to liquid ratio during the crystallization

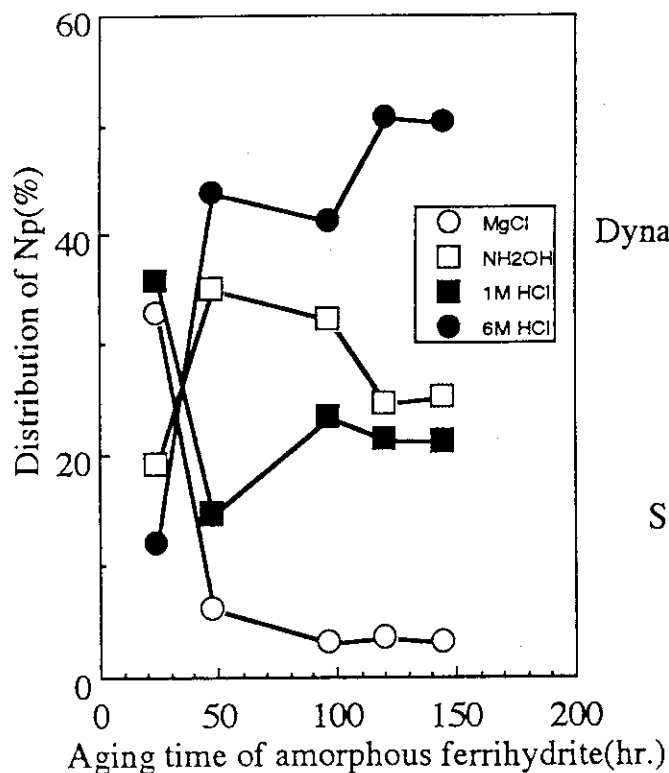


Fig. 2 Distribution of Np in the sequential extraction under the dynamic condition with coexistence of the crystallization.

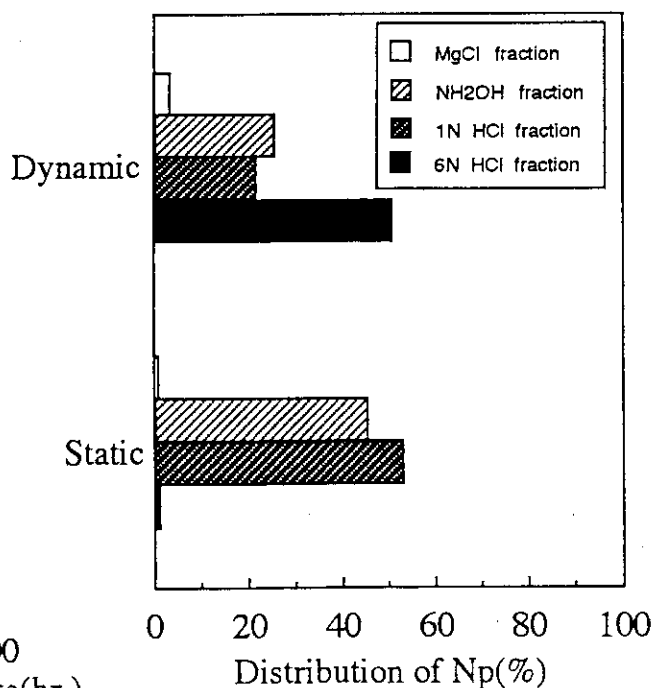


Fig. 3 Distribution of Np in the sequential extraction under the dynamic and static condition for the iron(III) precipitate with 100% crystallinity.

3.3 Long-term Radionuclide Fixation Mechanisms

3.3.1 The Use of Color to Quantify Effects of pH and Temperature on the Crystallization Kinetics of Goethite under Highly Alkaline Conditions¹

Tetsushi Nagano², Satoru Nakashima³, Shinichi Nakayama² and Muneaki Senoo²

Abstract

The crystallization kinetics of goethite were studied colorimetrically under highly alkaline conditions (pH10.1-12.2) at temperature regions from 40 to 85°C. Color changes during crystallization from fresh precipitates, plotted on a*-b* colorimetric diagrams, were used to discriminate between pure goethite and mixtures of goethite and hematite. Only the b* value increased as goethite crystallization proceeded, and even a minor increase in the a* value revealed the existence of hematite. The rate of goethite crystallization, estimated from the b* value, could be modeled by a pseudo-first-order rate law. This rate depended both on pH and on temperature. Apparent activation energies for the reactions of 56.1 kJ/mol at pH11.7 and 48.2 kJ/mol at pH12.2 were estimated from Arrhenius plots.

Keywords: Crystallization, Goethite, Kinetics, Colorimetry, Color, L*a*b* Color Space, Hematite

Introduction

Poorly ordered iron hydroxides (e.g. ferrihydrite) are known to transform into crystalline phases such as goethite, akaganeite and hematite depending on different synthetic and natural conditions. In nature, most ferrihydrite transforms to goethite (Lewis and Schwertmann, 1980; Cornell and Giovanoli, 1985), to hematite (Johnston and Lewis,

1 This article has been submitted to Clays & Clay Minerals.

2 Japan Atomic Energy Research Institute, Tokai, Naka, Ibaraki 319-11, Japan

3 The University of Tokyo, Hongo, Tokyo 113, Japan

1983: Combes et al., 1990), or to mixtures of the two phases (Schwertmann and Murad, 1983). The most likely reaction pathway of the transformation to goethite is thought to be dissolution of ferrihydrite and subsequent reprecipitation as goethite. Hematite is thought to form through internal rearrangement (i.e. direct dehydration) (Feitknecht and Michaelis, 1962; Schwertmann and Fischer, 1966). Although kinetic studies are one of useful methods to clarify the mechanisms of these transformations, which are influenced by temperature and pH as well as pressure, ionic strength and impurities, few of these studies have been reported in the literature (Cornell et al., 1989).

Color is one of the most distinguishing features of the oxidized iron compounds, which are largely responsible for the vivid colors of soils and rocks (Schwertmann and Cornell, 1991). Ferrihydrite typically is dark-brown, goethite is yellow, and hematite is red. Since crystallization of the iron compounds is accompanied by color changes, the color is considered to be a useful indicator for following the transformations. However, the use of color to quantify the iron compounds have been scarce (Barron and Torrent, 1984; Kosmas et al., 1986). Recently rapid and quantitative color measurements using a colorimeter have been successfully applied to rocks (Nagano and Nakashima, 1989; Nakashima et al., 1992) and marine sediments (Nagao and Nakashima, 1991). We showed that the color, described using the second CIE (Commission Internationale d'Eclairage) 1976 color space (generally referred to as $L^*a^*b^*$ color space), was a simple and quantitative parameter for the crystallization progress of goethite (Nagano et al., 1992). In the present study, we examined colorimetrically the kinetics of goethite crystallization under highly alkaline conditions, and the color changes occurring during hematite crystallization were quantified. In the kinetic study, we focussed on the effects of the aging temperature (40 to 85°C) and the initial pH of the solutions (pH 0.1-12.2) on the crystallization rates.

Experimental

Synthesis

Poorly ordered iron hydroxides were precipitated from 0.1M ferric nitrate solutions by adding 2M NaOH until an initial pH 0.1, 11.2, 11.7

and 12.2 had been reached. During the pH adjustment the solutions were stirred at least for fifteen minutes until the pH became stable. The solution temperature was $19.5 \pm 0.5^\circ\text{C}$. Portions of the fresh precipitates were centrifuge-washed twice with deionized water, freeze-dried, and slightly crushed with an agate mortar. The dried precipitates were identified as two-line ferrihydrite by X-ray diffractometry (XRD). Residual ferric precipitates were transferred into 12-mL transparent bottles and were kept at 40, 55, 70 and $85 \pm 1.0^\circ\text{C}$ in an electric oven. The bottles were not agitated during the aging because the agitation causes a change in the transformation rate. Colors of the precipitates were measured on the colorimeter at selected intervals. The color measurements can be made directly by reflecting light at the bottom of the samples through transparent glass.

Hematite was synthesized from a mixture of 0.1M ferric nitrate solution and 0.002M oxalic acid solution. The pH of the mixture was raised to pH 6.5 by adding 2M NaOH. The incubation temperature was 95°C (Schwertmann and Cornell, 1991). The initial precipitates at the start of the incubation period were also identified as two-line ferrihydrite. The color measurements were conducted in a manner similar to that described as above. The samples were then washed in dialysis tubes in 1 L deionized water at 10°C for two days and freeze dried.

Apparatus

Color measurements were conducted using a colorimeter (Minolta Chroma Meter, CR-200). The colorimeter is equipped with a pulsed lighting system for stable and uniform illumination of the specimen, photo-cells with filters to match the CIE standard observer spectral response, and electronic circuitry to determine accurate tri-stimulus values (Sugiyama, 1986). The colorimeter allows rapid, quantitative description of colors in terms of the values of standard color system (Munsell, Yxy, XYZ, $L^*C^*H^*$ and $L^*a^*b^*$ color space).

The Munsell notation, which consists of three dimensions of hue, value and chroma, has been the conventional method to describe the colors of soils or iron oxides. However, in this study we follow the recommendations of the CIE and use the $L^*a^*b^*$ color space to describe the colors of the precipitates. This system is considered to be more uniform, in which the coordinate scales are chosen with the intention of making equal

intervals represent as nearly as possible equal steps of discrimination for colors of the same luminance at all parts of the diagram. (Hunt, 1980). The L^* axis represents psychometric lightness; $L^*=0$ and $L^*=100$ correspond to black and white, respectively. The a^* and b^* axes represent psychometric chromaticness ($+a^*$ =red, $-a^*$ =green; $+b^*$ =yellow, $-b^*$ =blue) (Hunt, 1980). A white plate (Minolta) was measured as a reference.

Before every color measurement, the bottle was shaken to attain a homogeneous color of the precipitate and was centrifuged (1000 rpm, 1 minute) for rapid sedimentation. The precision of this measurement method was $\pm 0.7\%$ for L^* -value, $\pm 1.5\%$ for a^* , and $\pm 1.0\%$ for b^* , including the deviations arising from differences in the incubation bottles.

Crystalline phases of the resulting freeze-dried precipitates were characterized by X-ray diffractometry using a Rigaku powder diffractometer ($\text{CuK}\alpha$ radiation, 50kV, 35mA) equipped with the SUN data processing system. Infrared spectra of the samples were measured by diffuse reflectance spectroscopy using JEOL 3505 FT-IR spectrometer.

Results and Discussion

Color changes of goethite and hematite

Figure 1 shows color variations over time that are associated with the formation of goethite and hematite. The initial precipitate, identified as two-line ferrihydrite by XRD, exhibited a dark-brownish color (5YR 2/4 by Munsell chips) (Munsell Book of Color, 1976). On the other hand, the end product was brownish-yellow (10YR 5/8) for goethite and dark red (10R 3/8) for hematite. Color changes occurred continuously during the incubation from the initial precipitates to the end products. The XRD analyses showed that the end products of both the goethite and hematite crystallization reactions did not contain any other crystalline phases. Infrared spectroscopy analyses revealed that hematite contained a small amount of goethite (790 and 890 cm^{-1}), as well as water incorporated into the structure (3400 cm^{-1}), so that this phase is generally called hydrohematite (Wolska, 1981).

The crystallization of goethite seems to proceed colorimetrically parallel to the $+b^*$ axis, whereas that for hematite shows increases in both a^* and b^* values. This difference corresponds to the yellow appear-

ance of goethite and the red appearance of hematite to the naked eye. Figure 1 demonstrates that the b^* value can be used to measure the progress of goethite crystallization and that production of hematite can be detected by the increase in the a^* value.

In the incubation experiments in which hematite was synthesized, there was a positive correlation between color changes and X-ray diffraction patterns (Fig. 2) over time. These changes corresponded to nucleation and growth of hematite crystals. A peak height of the XRD 104 line of hematite (2.70\AA) was determined after smoothing the diffraction patterns and removing the backgrounds. During the first two hours, an induction period in which nuclei of hematite are thought to be forming (Cornell et al., 1989), the peak heights were equal to zero. From 2 until 8 hours, the intensity of the XRD peaks rapidly increased. Peak intensity was almost constant after 8 hours.

Equivalent changes were observed colorimetrically during the experiment. In the first two hours, there was virtually no change in color of the precipitates, followed by a pronounced change in color from 2 until 8 hours during which both a^* and b^* values increased accordingly. After 8 hours, little color change was observed.

The distinct colorimetric paths of crystallization for goethite and hematite that are shown on Fig. 1 suggest that a mixture of the two phases would be indicated by a value in the region between the lines defined by the single phases. As presented in the next section, we can use this method to describe the formation of pure goethite, pure hematite, or mixtures of the two phases on the a^* - b^* diagram.

Effects of temperature and pH

The effect of temperature between 40 and 85°C on the crystallization paths of ferrihydrite to the iron compounds is shown in Figs. 3a to 3d for four separate solutions with a pH 0.1, 11.2, 11.7 and 12.2, respectively. In the solution at pH 12.2 (Fig. 3d), temperature did not influence the direction of color change with the incubation time, which indicates formation of the single phase goethite. Goethite formation also appears to predominate at pH 11.7 between 40 and 70°C (Fig. 3c). At pH 0.1 and pH 11.2, higher temperatures result in larger a^* values, suggesting the formation of an appreciable amount of hematite in the mixture. All the curves in Fig. 3 can be plotted between those of goethite and

hematite shown in Fig. 1.

Data shown in Fig. 3 are replotted in Fig. 4 to show the effect of initial pH levels between 10.1 and 12.2 on the crystallization path at temperatures of 40, 55, 70, and 85°C. The pH effect on the direction of color change was not recognized in any of the solutions at 40°C except at pH10.1, nor was it noted at 55 and 70°C for the solutions above pH11.2. Development of hematite was noted in all solutions at 85°C. A dependence of the color change on pH, in which lower pH leads to larger a^* values, corresponds to the formation of hematite, which is favored at lower pH.

The direction of crystallization paths tends to shift toward the hematite line at higher temperatures and lower pHs. To determine the relative contents of goethite and hematite in the end products an XRD analysis was made (increment: $0.02^\circ 2\theta$, counting time: 10 sec./increment) for 20 to $25^\circ 2\theta$, which includes the strongest reflection of goethite at $21.2^\circ 2\theta(110)$, and of hematite at $24.2^\circ 2\theta(012)$ among non-overlapping peaks with goethite. Table 1 shows the integrated intensity (peak height times width at half height) of the 110 line of goethite and the integrated intensity of the 012 line of hematite. The greatest intensity was given by the sample at pH11.2 and 55°C for goethite and at pH6.5 and 95°C for hematite, and so the relative goethite or hematite content in these samples was set equal to 100. Based on hematite/goethite ratios (Hm/Gt) calculated from the relative contents (Table 1), a diagram of the fields of formation of goethite and mixtures of goethite and hematite was constructed as a function of the incubation temperature and the initial pH (Fig. 5). Higher temperatures and lower pHs in this study are obviously favorable for the formation of hematite. This tendency is also recognized by the color change. The sequence of the Hm/Gt ratios corresponds to that of directions of color changes represented by final a^* and b^* (Table 1). Although the color change direction for pH 11.2 and 55°C is clearly different from goethite line, the relative content of hematite is 0. As is shown in Table 1, pure goethites show similar widths of the 110 line (0.62-0.66) except at pH11.2 and 55°C (0.40). A thinner width of the 110 line indicates the formation of different types of goethite, e.g., acicular crystals of smaller width (Schwertmann and Murad, 1983), which may lead to the shift from the goethite line of color change at pH11.2 and 55°C. Since mixtures of goethite and hematite show the widths of the 110 line between 0.50 and 0.58 (Table 1), the directions of color change of the mixtures are considered to be controlled by the formation

of hematite rather than that of goethite with different morphology.

Kinetics of goethite crystallization

In our previous study on the color variations associated with goethite crystallization, the b^* values were related to the goethite proportion determined both by an XRD peak intensity of the 110 line and by an infrared peak area at 890 cm^{-1} (Nagano et al., 1992). Figure 6 shows goethite crystallization curves constructed based on the variations of b^* value. The b^* value increases with the incubation time, and remains constant. The crystallization of ferrihydrite to goethite was shown by Schwertmann and Murad (1983) to follow a pseudo-first-order reaction rate law; the rate of crystallization at any time is proportional to the amount of residual ferrihydrite in the precipitates. The positive relationship between goethite crystallinity and the b^* value also indicates an exponential increase in the b^* values. The crystallization curves shown in Fig. 6 follow the following type of equation.

$$b^* = C_1 - C_2 \cdot \exp(-k \cdot t) \quad (1)$$

where t is the incubation time (h), and C_1 , C_2 and k are constants. We fit the colorimetric data to equation (1) by a least-squares fitting method to estimate k , the rate constant of the overall reaction. The results are summarized in Table 2 for the samples with the color change directions corresponding to goethite.

Temperature effects on the crystallization kinetics of goethite are expressed in the form of the Arrhenius plots (Fig. 7). The positive temperature effect on the crystallization kinetics is obvious. Effects of pH on the goethite crystallization kinetics are shown in Fig. 8. Higher pH conditions apparently result in higher rate constants, and a positive effect of pH on the kinetics is also obvious.

Rates of goethite crystallization are significantly influenced by aging temperature and by the initial pH of solutions. With respect to the goethite crystallization mechanism, Misawa et al. (1974) stresses a solid state transformation on the basis that both ferrihydrite and goethite consist of hexagonal close-packed oxygen framework. However, the generally accepted model for the goethite crystallization consists of two steps: dissolution of ferrihydrite and reprecipitation of the Fe as goethite (Feitknecht and Michaelis, 1962; Schwertmann and Fischer, 1966). In the present study, we follow the two-step crystallization model to

explain both the pH- and the temperature-dependence of the rate as below.

According to a more refined model of the two-step model, goethite is strongly favored where the concentration of monovalent Fe(III) ions such as $\text{Fe}(\text{OH})_2^+$ or $\text{Fe}(\text{OH})_4^-$ is at a maximum (Schwertmann and Murad, 1983). $\text{Fe}(\text{OH})_4^-$ is the dominant dissolved species in highly alkaline aqueous solutions (Stumm and Morgan, 1981), and therefore could be the species controlling goethite precipitation. In considering the pH-dependence of the rate (Fig. 8), we can consider the dissolution of ferrihydrite for the present condition to be the OH^- promoted reaction as,



The apparent activation energies of the overall reaction were calculated from the slope of the Arrhenius plots to be 56.1 ± 0.6 kJ/mol for pH11.7 and 48.2 ± 4.1 kJ/mol for pH12.2. These values are within the range of mineral-solution alteration processes such as dissolution of some silicates (Lasaga, 1981; Schott and Petit, 1987).

Conclusion

The crystallization progress of goethite, hematite and mixtures of the two phases was investigated in alkaline aqueous solutions by measuring their colors. The direction of color changes on a^*-b^* diagrams allows us to discriminate between goethite and a goethite-hematite mixture. Goethite was indicated by parallel colorimetric changes to the b^* -axis, and hematite was indicated by increases in both the a^* and b^* values. Mixtures of the two phases had colorimetric values that plotted between the lines defined by goethite and by hematite alone. Crystallization curves for goethite based on the b^* values indicated exponential time evolution. Pseudo-first order rate constants were obtained from the curves. Arrhenius plots showed the apparent activation energies to be about 56.1 kJ/mol at pH11.7 and 48.2 kJ/mol at pH12.2. The temperature and pH dependence of the goethite crystallization rate supported the published two-step model consisting of dissolution of ferrihydrite and subsequent precipitation of goethite.

Acknowledgment

The authors would like to thank Drs. K. Sekine and S. Nagao of Japan Atomic Energy Research Institute (JAERI) for useful discussions and encouragement during the course of this work, and Dr. T. Sato of JAERI for the technical support of XRD analyses. Review of the manuscript for English stylistics by Dr. J. McMurtry is greatly appreciated. Critical reviews and comments by Drs. U. Schwertmann and J. Amonette are also gratefully acknowledged.

References

- Barron, V. and Torrent, J. (1984) Influence of aluminum substitution on the color of synthetic hematites: *Clays & Clay Minerals* 32, 157-158.
- Cornell, R.M. and Giovanoli, R. (1985) Effect of solution conditions on the proportion and morphology of goethite formed from ferrihydrite: *Clays & Clay Minerals* 33, 424-432.
- Cornell, R.M., Giovanoli, R. and Schneider, W. (1989) Review of the hydrolysis of iron (III) and the crystallization of amorphous iron (III) hydroxide hydrate: *J. Chem. Tech. Biotechnol.* 46, 115-134.
- Combes, J.M., Manceau, A., Calas, G. and Bottero, Y. (1990) Formation of ferric oxides from aqueous solutions: A polyhedral approach by X-ray absorption spectroscopy: II. Hematite formation from ferric gels: *Geochim. et Cosmochim. Acta* 54, 1083-1091.
- Feitknecht, W. and Michaelis, W. (1962) Über die Hydrolyse von Eisen (III) perchlorat-Lösungen, *Helv. Chim. Acta* 45, 212-224.
- Hunt, R.W.G. (1980) Color terms, symbols, and their usage: in *Optical Radiation Measurement*, F. Grum and C.J. Bartleson, eds., Academic Press, New York, 11-31.
- Johnston, J.H. and Lewis D.G. (1983) A detailed study of the transformation of ferrihydrite to hematite in aqueous medium at 95°C: *Geochim. et Cosmochim. Acta* 47, 1823-1831.
- Kosmas, C.S., Franzmeier, D.P. and Schulze, D.G. (1986) Relationship among derivative spectroscopy, color, crystalline dimensions, and Al substitution of synthetic goethites and hematites: *Clays & Clay Minerals* 34, 625-634.
- Lasaga, A.C. (1981) Rate laws of chemical reactions: in *Reviews in Min-*

- eralogy 8, *Kinetics of Geochemical Process*, A.C. Lasaga and R.J. Kirkpatrick, eds., 1-68.
- Lewis, D.G. and Schwertmann, U. (1980) The effect of [OH] on the goethite produced from ferrihydrite under alkaline conditions: *J. Colloid Interface Sci.* 78, 543-553.
- Misawa, T., Hashimoto, K. and Shimodaira, S. (1974) The mechanism of formation of iron oxide and oxyhydroxides in aqueous solutions at room temperature: *Corr. Sci.* 14, 131-149.
- Munsell Book of Color, 2.5R-10G (1976), Munsell Color Macbeth Division of Kollmorgen Corporation, Baltimore, Md.
- Nagano, T. and Nakashima, S. (1989) Study of colors and degree of weathering of granitic rocks by visible diffuse reflectance spectroscopy: *Geochem. J.* 23, 75-83.
- Nagano, T., Nakashima, S., Nakayama, S., Osada, K. and Senoo, M. (1992) Color variations associated with rapid formation of goethite from proto-ferrihydrite at pH13 and 40°C. *Clays and Clay Minerals* 40, 600-607.
- Nagao, S. and Nakashima, S. (1991) A convenient method of color measurement of marine sediment by chromameter: *Geochem. J.* 25, 187-197.
- Nakashima, S., Miyagi, I., Nakata, E., Sasaki, H., Nittono, S., Hirano, T., Sato, T. and Hayashi, H. (1992) Color measurement of some natural and synthetic minerals-I: *Rep. Res. Inst. Natural Resources, Mining College, Akita Univ.* 57, 57-76.
- Schott, J. and Petit, J.C. (1987) New evidence for the mechanisms of dissolution of silicate minerals: in *Aquatic Surface Chemistry*, W. Stumm, ed., Wiley-Interscience, New York, 293-315.
- Schwertmann, U. and Cornell, R.M. (1991) Iron Oxides in the Laboratory p.101-110. Verlag Chemie VCH, Weinheim, Germany.
- Schwertmann, U. and Fischer, W.R. (1966) Zur Bildung von α -FeOOH und α -Fe₂O₃ aus amorphous Eisen(III)-hydroxid. III, *Z. Anorg. Allg. Chem.* 346, 137-142.
- Schwertmann, U. and Murad, E. (1983) Effect of pH on the formation of goethite and hematite from ferrihydrite: *Clays & Clay Minerals* 31, 277-284.
- Stumm, W. and Morgan, J.J. (1981) Precipitation and Dissolution: in *Aquatic Chemistry 2nd Edition*, Wiley-Interscience, New York, 230-322.
- Sugiyama, M. (1986) Chroma Meters: *Minolta Techno Report*.
- Wolska, E. (1981) The structure of hydrohematite: *Z. Kristallogr.* 154, 69-75.

Table 1 Nature of crystalline products after aging at various pH and temperature conditions.

Condition		Goethite		Hematite		Hm/Gt	Final	
pH, T(°C)		WHH ₁₁₀	Intensity(%)	WHH ₀₁₂	Intensity(%)		a*	b*
12.2	40	0.62	86	—	—	—	9	38
	55	0.64	85	—	—	—	8	39
	70	0.66	74	—	—	—	9	38
	85	0.64	71	—	—	—	9	37
11.7	40	0.64	80	—	—	—	8	37
	55	0.64	79	—	—	—	8	37
	70	0.66	75	—	—	—	9	38
	85	0.58	83	0.44	2	0.02	13	42
11.2	40	0.66	79	—	—	—	9	36
	55	0.40	100	—	—	—	9	45
	70	0.50	92	0.36	2	0.02	13	44
	85	0.56	99	0.54	9	0.09	19	40
10.1	40	0.56	66	0.52	3	0.05	16	45
	55	0.58	81	0.48	15	0.19	23	40
	70	0.56	68	0.52	43	0.63	27	33
	85	0.58	41	0.54	70	1.71	27	30
6.5	95	—	—	0.52	100	∞	25	23

Table 2 Pseudo-first order rate constants for goethite crystallization.

pH, Temperature (°C)	k (h ⁻¹)
12.2, 85	1.46 ± 0.104
12.2, 70	0.72 ± 0.057
12.2, 55	0.40 ± 0.024
12.2, 40	0.13 ± 0.006
11.7, 70	0.45 ± 0.073
11.7, 55	0.18 ± 0.018
11.7, 40	0.07 ± 0.003
11.2, 40	0.03 ± 0.005

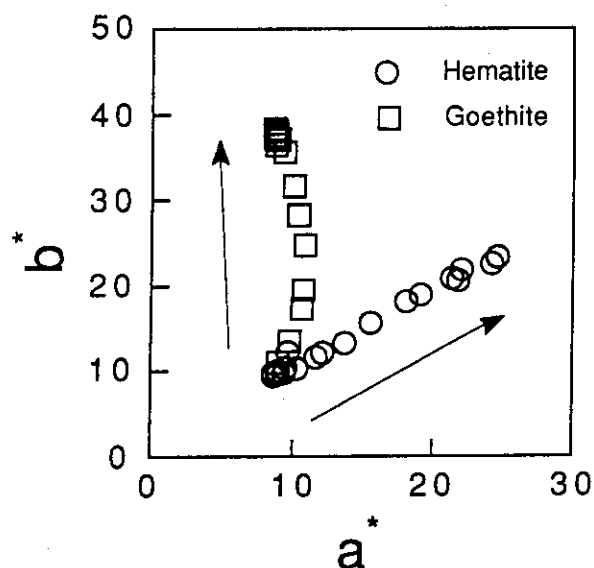


Fig. 1 Color variations on an a^* - b^* diagram associated with crystallization of ferrihydrite to goethite at pH12.2 and 40°C and to hematite at pH6.5 and 95°C. The crystallization of goethite seems to proceed almost parallel to b^* axis, whereas that for hematite shows increases in both a^* and b^* values. Arrows indicate increases in incubation time.

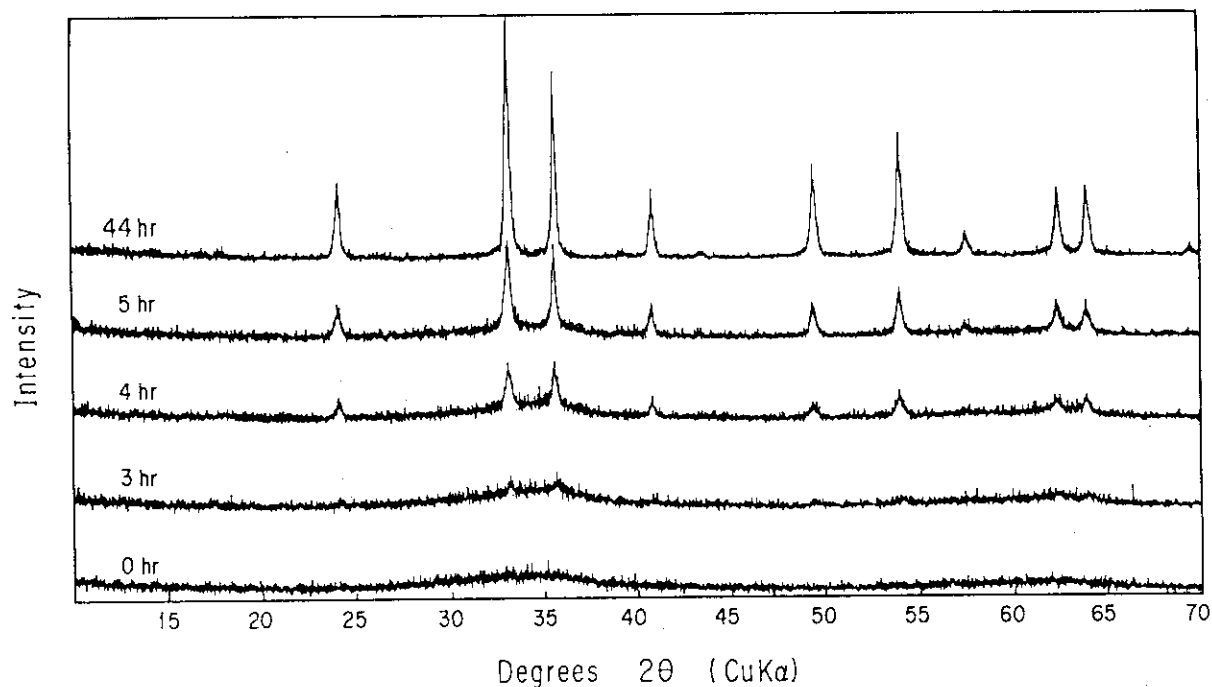


Fig. 2 X-ray diffraction patterns of the iron hydroxide crystallized to hematite with an aging time of 0, 3, 4, 5, and 44 hours.

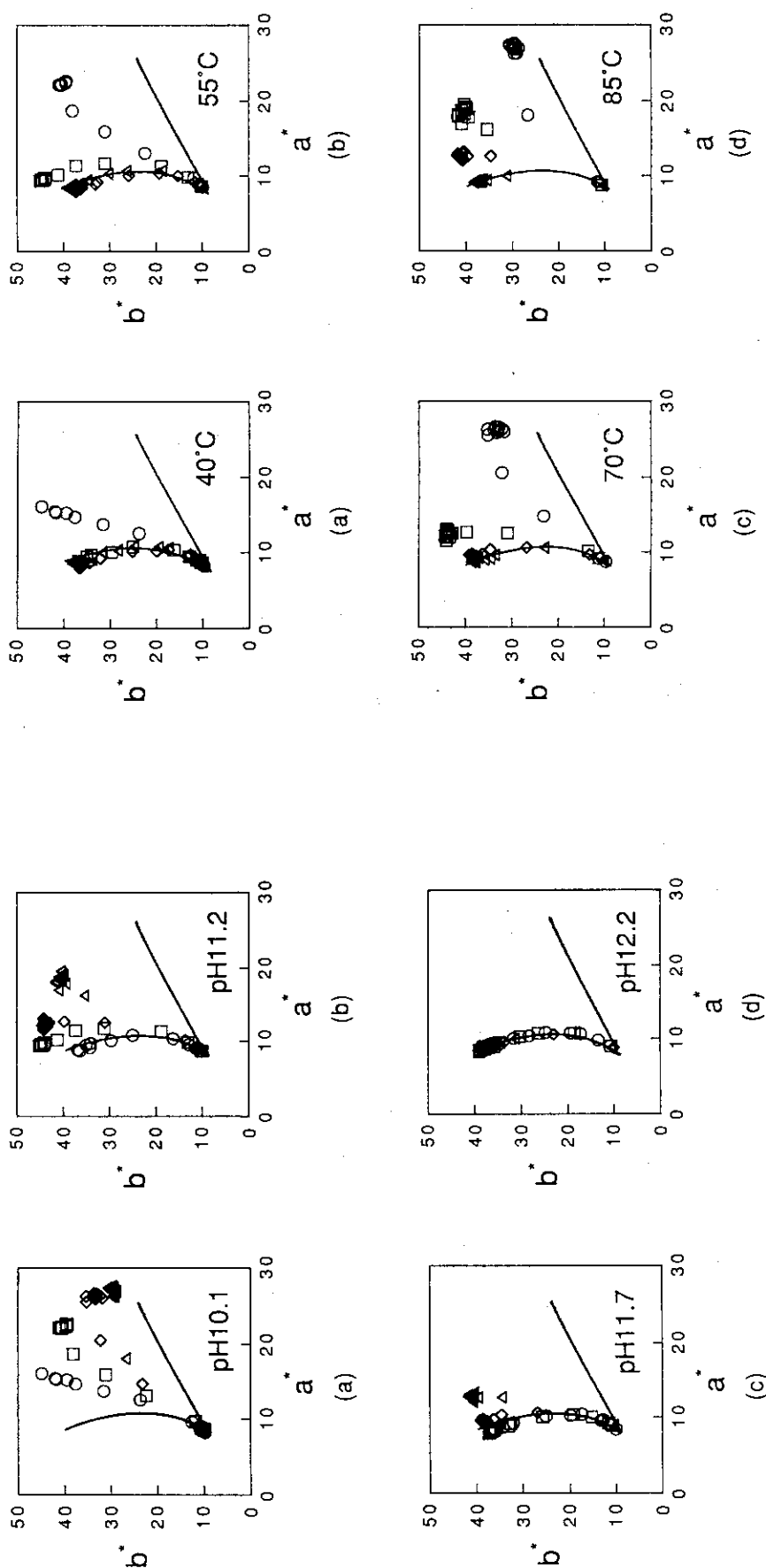


Fig. 3 Temperature effects on color variations during crystallization from ferrihydrite to goethite or hematite; (a) pH10.1, (b) pH11.2, (c) pH11.7, (d) pH12.2. Solid lines show the goethite and hematite lines from Fig. 1.

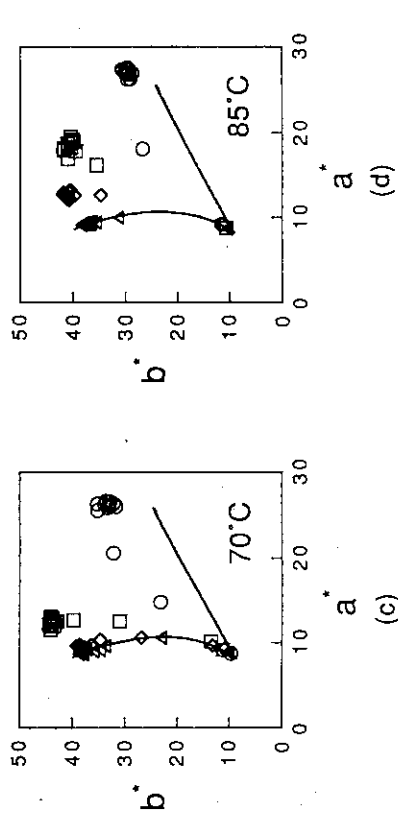


Fig. 4 Effects of pH on color variations during crystallization from ferrihydrite to goethite or hematite; (a) 40°C, (b) 55°C, (c) 70°C, (d) 85°C. Solid lines show the goethite and hematite lines from Fig. 1.

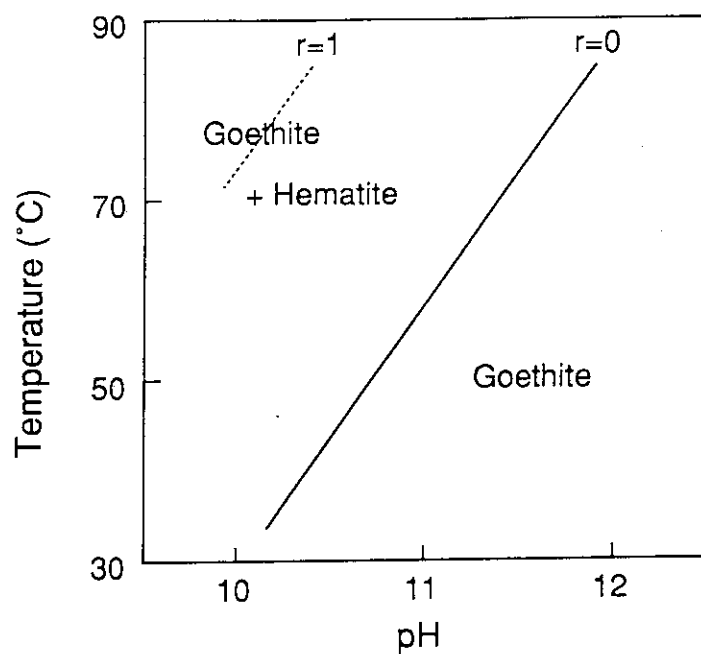


Fig. 5 Fields of formation of goethite and mixtures of goethite and hematite as a function of the initial pH and the aging temperature. An r represents the Hm/Gt ratio in Table 1.

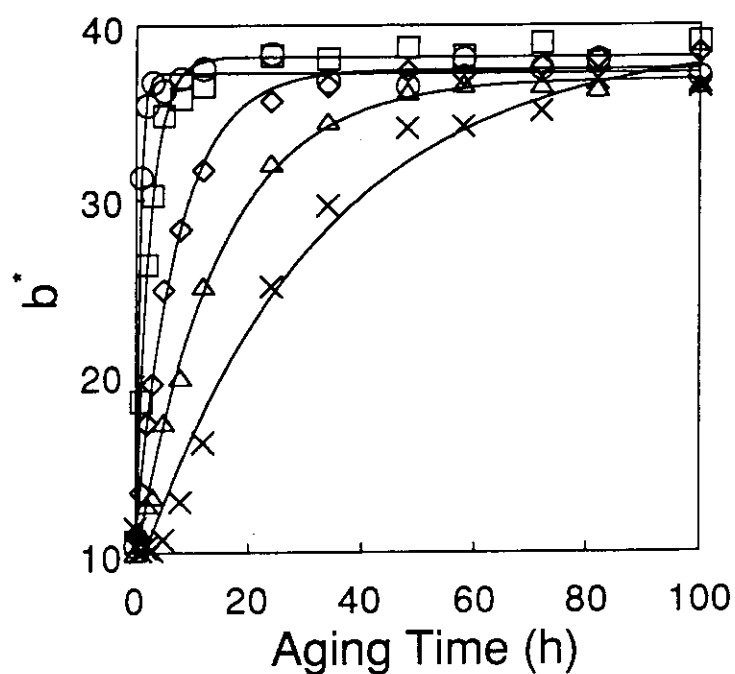


Fig. 6 Crystallization curves of goethite based on the b^* values. These curves appear to follow a pseudo-first order rate law.
 ○ pH12.2, 85°C, □ pH12.2, 55°C, ◇ pH12.2, 40°C, △ pH11.7, 40°C, × pH11.2, 40°C.

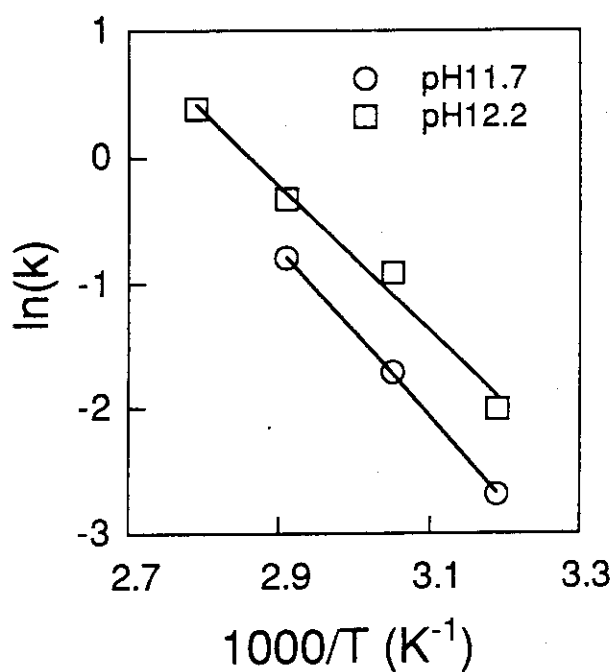


Fig. 7 Arrhenius plots for the samples at pH11.7 (40-70°C) and pH12.2 (40-85°C), where only goethite formed. Apparent activation energies of overall reactions were calculated to be 56.1 KJ/mol for pH11.7 and 48.2 KJ/mol for pH12.2.

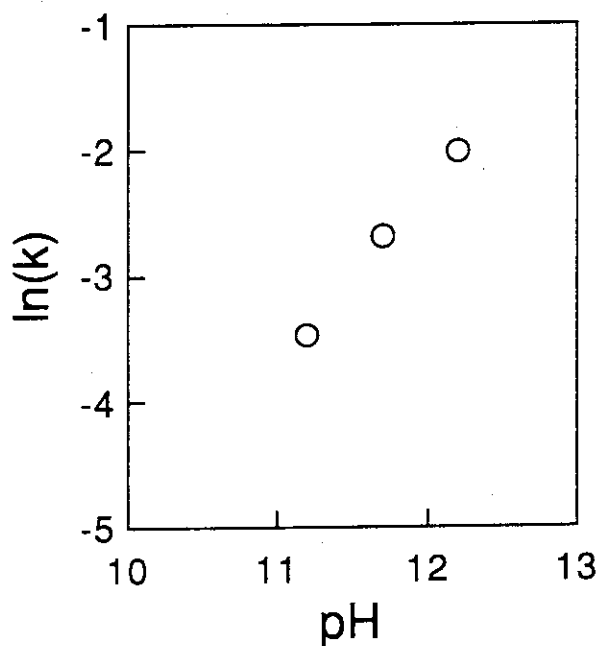


Fig. 8 Effects of pH on the crystallization rates of goethite at 40°C and pH11.2-12.2. Positive effects of $[\text{OH}^-]$ shown in this figure indicate that goethite crystallization is the OH^- promoted reaction.

4. Natural Analogue Study

4.1 Groundwater Geochemistry and Distribution of U-series Radionuclides in the Koongarra Uranium Ore Deposit, Australia

N. Yanase, T.E. Payne and K. Sekine

Introduction

A detailed understanding of the migration behavior of actinides in the geosphere is now urgently needed to assist in the safety assessment of high level radioactive waste disposal. Geochemical studies of uranium orebodies enable the migration of uranium and other radionuclides over long geologic timescales to be investigated. Information from these 'natural analogues' will be used to predict the behavior of repository systems over long timescales. Therefore, natural analogue studies have been carried out at several sites throughout the world (Airey, 1986; Cramer, 1989; Petit, 1990; Suutarinen et al., 1991; Menager et al., 1992; Menet et al., 1992; Nohara et al., 1992).

The Alligator Rivers Analogue Project (ARAP) was one of these natural analogue studies, and was aimed at understanding the mobility and retardation of uranium at the Koongarra uranium ore deposit over long timescales (Duerden et al., 1987). In this study the chemical characteristics of, and uranium distribution in, Koongarra groundwaters were investigated to provide a geochemical framework of the Koongarra system.

The decay series of uranium-238 contains a variety of elements, many of which have applications as tracers in the environment. The isotopes in this decay series have a wide range of half-lives, which makes them particularly useful in estimating the timescales of environmental phenomena. As well as ^{238}U ($T_{1/2} = 4.5 \times 10^9$ years), this decay series includes ^{234}U ($T_{1/2} = 2.4 \times 10^5$ y), ^{230}Th (7.5×10^4 y), ^{226}Ra (1600 y), ^{222}Rn (3.8 days) and ^{210}Pb (22 y), together with some shorter lived isotopes. The activity of each radionuclide in groundwaters varies over a wide range, depending on the level of ^{238}U in the solid phase which is the source of these radionuclides in the groundwater.

In many geochemical applications, it is not the absolute activity of each isotope which is of primary interest, but the relative activity of the isotopes to one another or to ^{238}U . This is not a function of the radioactivity of the solid phase, but is dependent on the groundwater

geochemistry. Therefore, activity ratios provide a useful tool in investigating the geochemical phenomena influencing radionuclide migration.

The Study Site

The Koongarra uranium deposit is situated 225 km east of Darwin in the Northern Territory of Australia. The details of the most recent studies of the geology, geochemistry and hydrology of the site were reported in the final reports of the ARAP studies (Snelling, 1993; Davis et al., 1994; Payne et al., 1994). The zone of primary uranium mineralization has been intersected by weathering conditions, and this has resulted in the formation of a secondary ore zone and a dispersion fan in the weathered zone. The dispersion fan is a uranium-rich zone which extends away from the primary ore-zone in the direction of groundwater movement. The primary orebody extends to depths exceeding 100 m, and the weathered zone is about 30 m thick. The host rock of the Koongarra ore deposit is quartz chlorite schist. Secondary uranium minerals and weathering products such as clay and iron minerals are present in the weathered zone. The groundwater flow direction is generally from northwest to southeast, moving away from the Koongarra fault.

Experimental

1. Sampling and field measurement

Numerous boreholes exist at Koongarra and may be used for groundwater sampling (Fig. 1). These boreholes fall into the following categories:

a) PH, KD, C and M holes. These boreholes have a metal casing through the weathered zone to prevent them from collapsing. Therefore, groundwaters are sampled from depths greater than about 20 m using these boreholes. Groundwater from these boreholes was usually obtained using a submersible pump suspended between inflatable packers (Fig. 2A).

c) W holes. The W boreholes were constructed to obtain groundwaters from within the weathered zone. They were cased with two PVC (polyvinyl-chloride) pipes, open at two separate intervals (Fig. 2B). These were at

depths 13-15 m (referred to as W1a, W2a, etc.), and 23-25 m (W1b, W2b, etc.).

Seven field samplings after and before the annual wet season were carried out in May and November 1988, May and October 1989, May and November 1990, and April 1991 for 48 boreholes to collect groundwater samples. The usual sampling procedure was to pump the borehole using a submersible electric or diaphragm pump whilst monitoring the pH and conductivity. When these parameters became stable it was considered that the standing water had been eliminated and aquifer water was being sampled. The bicarbonate concentration was determined by titration with standard (0.010 M) HCl solution (Barnes, 1964), and other field parameters including pH, Eh, conductivity and dissolved oxygen (DO), were measured. For most chemical analyses, samples were taken after filtration through a 0.45 μm membrane filter.

2. Chemical analysis

At the laboratory, elemental analyses were carried out using a number of techniques including ICPMS, ICPAES, AAS, anion exchange chromatography, and spectrophotometry. The procedures used were generally standard techniques and reported previously (Payne et al., 1994). Phosphate was determined using a standard molybdenum blue spectrophotometric method (APHA, 1985). Uranium was measured using alpha and gamma spectrometry, quantitative ICPMS and the Kinetic Phosphorescence Analyzer (KPA). The technique of alpha spectrometry has been documented in detail elsewhere (Ivanovich and Harmon, 1982). The gamma spectrometry is described in the next section. The KPA has been more recently developed, and enables rapid determination of uranium concentrations to be made in aqueous samples, with good sensitivity and accuracy provided that interferences are not present (Payne et al., 1994).

3. Measurement of uranium-series isotopes by gamma spectrometry

Radon-222 and ^{226}Ra in the groundwater were measured directly by gamma spectrometry (hereafter referred to as the "direct method"), and the other isotopes were measured by gamma spectrometry after evaporation of the groundwater to dryness (hereafter referred to as the "evaporation method"). The concentrations of ^{238}U and $^{234}\text{U}/^{238}\text{U}$ activity ratios in the residue of groundwater were also determined by alpha spectrometry.

3.1 Direct method

For the determination of ^{222}Rn and ^{226}Ra , about 250-500 mL of ground-water was collected in a polyethylene or polycarbonate bottle. At the time of analysis, the exact amount of the sample solutions was determined by weighing, and the amount of added HNO_3 was allowed for in subsequent calculations. Samples were measured using an ORTEC Ge detector (closed end coaxial type, N type crystal) for 5,000-50,000 seconds, with the count-time depending on the activity of the sample. The combined $^{222}\text{Rn} + ^{226}\text{Ra}$ concentration was determined from the 352 keV peak of ^{214}Pb , or the 609 keV peak of ^{214}Bi . These are both daughter nuclides of ^{222}Rn . Figure 3 shows a spectrum of groundwater collected at W4b.

In order to check the tightness of sample bottles for ^{222}Rn gas leakage, some samples with high ^{222}Rn activities were measured repeatedly. For these samples, the ^{222}Rn activity decreased in accordance with the half-life of ^{222}Rn (3.8 days), from which it was concluded that leakage of ^{222}Rn from the sample bottles was negligible.

After two months, all the samples were measured again (for 30,000-300,000 seconds), to determine the ^{226}Ra concentration. By this time, about 16 times of ^{222}Rn half-life had elapsed, so the contribution from "unsupported" ^{222}Rn (present at the time of sampling) was insignificant. The original ^{222}Rn concentration was calculated by subtraction of the ^{226}Ra activity from the original $^{222}\text{Rn} + ^{226}\text{Ra}$ concentration. Appropriate corrections for radioactive decay from the time of sampling to the commencement of the measurements, and during the measurements, were included in all calculations. The detector was calibrated by the measurement of a ^{226}Ra standard solution obtained from Amersham, UK, with the same conditions as for the sample measurement. The same samples were then analyzed by the evaporation method described in the next section.

3.2 Evaporation method

The groundwater samples (500-2000 mL) for the determination of ^{238}U , ^{226}Ra and ^{210}Pb , were weighed, then evaporated to about 100 mL in a glass beaker. They were then transferred to a plastic vessel (inner diameter 32 mm or 24 mm), and the evaporation was continued to near dryness using an infra-red lamp. The dried residue was sealed and stored for more than 5 months to equilibrate the ^{234}Th ($T_{1/2} = 24$ days) activity with ^{238}U activity. It was then measured by gamma spectrometry using an ORTEC LO-AX detector (51 mm and 19 mm in diameter and thickness, respectively).

Uranium-238, ^{226}Ra and ^{210}Pb were determined from the gamma-ray peaks at 63 keV (of ^{234}Th), 186 keV and 46.5 keV respectively. For the determination of ^{226}Ra in the residual sample, the contribution to the 186 keV peak from ^{235}U was subtracted. This was done using the counts in the 63 keV peak, using a constant activity ratio ($^{235}\text{U}/^{238}\text{U} = 0.046$), which was calculated from the natural abundance of ^{235}U (0.720 atom%) and ^{238}U (99.275 atom%). The 352 keV or 609 keV peaks (used for determinations in the direct method) were not used in this case, as a leakage of ^{222}Rn from the measurement vessel may have introduced a source of error.

The detector was calibrated by the measurement of ^{238}U and ^{226}Ra powder rock standards obtained from NBL (New Brunswick Laboratory), USA, with the same conditions as for the sample measurement. Figure 4 shows a spectrum of the residue of groundwater collected at W4b.

For the subsequent analysis of ^{238}U and ^{234}U , ^{232}U yield tracer and 6 M HCl were then added to the residue used in the previous determination. After more than 2 weeks, the liquid phase was filtered through a 0.45 μm membrane filter. The uranium leached from the residue was purified by chemical separation and measured by alpha spectrometry.

Results and Discussion

1. Main characteristics of groundwaters

Selected parameters for a groundwater sample from near the center of the orebody (borehole W4) are shown in Fig. 5. The region close to this borehole can be considered to be a starting point of uranium migration. The main characteristics of the W4 samples are:

- a) the pH is close to neutral,
- b) the conductivity is low, indicating a dilute groundwater with low levels of dissolved constituents,
- c) magnesium is the dominant cation, and is important at Koongarra because it is released by weathering of the chloritized schists of the host rocks by groundwaters (Murakami et al., 1990; Herczeg and Payne, 1992),
- d) the major anion is bicarbonate,
- e) the groundwater contains elevated concentration of uranium,
- f) the groundwater is slightly oxidizing with respect to $\text{U}^{4+}/\text{U}^{6+}$, and

g) levels of silicon are high relative to many of the cations present.

2. Seasonal effects

The annual fluctuation of standing water levels at Koongarra raises the possibility that the chemical conditions and movement of uranium in groundwater could be strongly dependent on the season. For the key parameters, magnesium and bicarbonate concentrations, only slight differences were detected between samples from different field trips (Fig. 6).

The relatively constant major ion concentrations of these groundwaters imply that seasonal change in groundwater geochemistry is a relatively minor consideration in uranium migration in the permanently saturated zone. The spatial variation is of far greater significance. The pH and the concentrations of phosphate together with the magnesium and bicarbonate were also reproducible, which implies that the speciation of uranium is likely to be similar throughout the year at the depths of both the 13-15 m and 23-25 m sampling points.

3. Change of chemical characteristics with depth

As discussed above, the seasonal change of groundwater characteristics was small, however, the characteristics were highly dependent on the sampling depth. The pH of samples from the depth greater than 13 m in the Cahill formation is fairly uniform, usually between 6.5 and 7.7 (Fig. 7). Rainwater, sampled at Koongarra on a field trip in April 1991, had a pH of 5.2, significantly below neutral, and contained very dilute levels of total dissolved constituents, as indicated by its low conductivity of 17 $\mu\text{S}/\text{cm}$. A small creek at Koongarra was also sampled in April 1991. At this time of year, it would be expected that this water would be similar to rainwater and this was shown by its composition. The pH was 4.6 and conductivity was 18 $\mu\text{S}/\text{cm}$. The pH/Eh conditions of groundwater samples are plotted on Fig. 7 for the samples collected in April 1991. The groundwaters from depths greater than 13 m plot in a field of relatively higher pH and lower redox potential. The pH/Eh of the shallower samples (<12 m) trends towards those of creek and rain waters. This diagram suggests a gradation in groundwater pH/Eh conditions as a function of depth.

Figure 8 shows the correlation between Mg and HCO_3 concentrations, which are the major cation and anion, in the three depth regions for all

the groundwater samples. It was apparent that both concentrations were lower in the shallow region (<12 m) than in the deeper region. However, there is no distinct difference in these concentrations for the deeper depth (>13 m). The characteristics of the Koongarra groundwaters are summarized in Table 1.

4. Chemical form of uranium

The pH and redox potential are indicators of the acidity and likely oxidation states of key species such as Fe and U. As shown in Fig. 7, pH/Eh conditions tended to be in the regime of significant uranium solubility (uranium present in its oxidized (U(VI) state) (Brookins, 1988). Therefore, Koongarra groundwaters would generally be expected to dissolve the rather insoluble mineral uraninite (UO_2) which is present in the primary ore zone. Similar conclusions have been reached after detailed geochemical modelling of the Koongarra groundwater data (Sverjensky, 1994). The chemical speciation of uranium (which influences its adsorption behavior) is a function of the concentrations of complexing ligands. Koongarra groundwaters are quite low in total organic carbon (generally below 2 mg/L), therefore inorganic species, such as carbonate and phosphate are likely to be the main uranyl complexants. If phosphate does not play a significant role, the speciation of uranium at Koongarra would be expected to be dominated by uranyl carbonate species. In fact, Sandino and Bruno (1992) suggested that carbonate species were dominant when the carbonate concentration was more than one order of magnitude greater than the phosphate concentration. At Koongarra, the bicarbonate concentration was three orders of magnitude higher than the phosphate concentration (Fig. 5). Furthermore, positive correlation between the concentrations of uranium and bicarbonate in groundwater was observed (Fig. 9), but there was no correlation between uranium and phosphate.

5. Radioactivity of uranium series nuclides

5.1 Horizontal distributions of ^{238}U and ^{210}Pb

The ^{238}U concentration was highest in the center of the orebody, being 6.3 Bq/L in a sample obtained from borehole W4a. The plan-view of ^{238}U activity (Fig. 10) showed that the extent of ^{238}U dispersion to the south (towards borehole C1) was greater than the dispersion towards the south-east, in the direction of PH94. Groundwater from PH80, which is

some 100 m from the recognized limits of the No.1 orebody, has ^{238}U concentrations of 0.056-0.18 Bq/L, which was significantly above the levels found at PH94 of 0.0026-0.0073 Bq/L, which are similar to the background levels for the Koongarra area.

The contours of ^{210}Pb activities suggested an elongation of the radiochemical halo from the orebody in the direction of PH80, where the concentration of ^{210}Pb was significantly elevated (Fig. 11). The PH88 (38-40 m) sample was noted as showing an unusually high ^{210}Pb activity. This sample, and the sample from PH80, had the highest ^{210}Pb content obtained outside the zones of primary and secondary uranium mineralization. Indeed, the ^{210}Pb activities at PH80 were higher than groundwaters from PH55, which intersects the dispersion fan. These data are a further indication of the possibility of groundwater flow towards C1 rather than towards PH94.

5.2 Activity ratios of uranium series nuclides

5.2.1 U-234/U-238 activity ratios

The measured $^{234}\text{U}/^{238}\text{U}$ activity ratios in groundwater are generally greater than unity. However, for many Koongarra groundwater samples, the $^{234}\text{U}/^{238}\text{U}$ ratio is below unity (Fig. 12). In the weathered and transition zones, the $^{234}\text{U}/^{238}\text{U}$ ratio ranges from 0.65 at W2 (13-15 m) to 1.25 at PH94 (26-28 m). In the unweathered zone, the highest value of this ratio is 1.41 at PH58 (38-40 m) and the lowest value is 0.76 at PH88 (38-40 m). Figure 13 shows a plan view of $^{234}\text{U}/^{238}\text{U}$ activity ratio at the depth of 20-30 m. There was an elongation of the low $^{234}\text{U}/^{238}\text{U}$ ratio around W2 borehole towards PH88 and PH80 boreholes.

A process contributing to the relative immobility of ^{234}U (compared to ^{238}U) has been proposed by Nightingale (1988), who observed that the process of alpha-recoil, as well as injecting ^{234}Th into solution, also immobilized some ^{234}Th by recoiling it into resistant mineral phases where the daughter ^{234}U was invulnerable to leaching, that is, "alpha-recoil emplacement". Another possible explanation of low $^{234}\text{U}/^{238}\text{U}$ activity ratio is that ^{234}Th (24 days), daughter of ^{238}U , is adsorbed on to clay and iron minerals produced by weathering of host rock, and ^{234}Th and its daughter nuclide, ^{234}U , are subsequently fixed in the minerals (Ohnuki et al., 1990). This results a depletion of ^{234}U in groundwater.

5.2.2 Ra-226/U-238

In the weathered zone, the highest value of the $^{226}\text{Ra}/^{238}\text{U}$ activity ratio was 34 at PH14 (20-26 m) and the lowest was 0.02 at W2 (23-25 m), where the lowest $^{234}\text{U}/^{238}\text{U}$ ratio was observed (Fig. 13). In the unweathered zone, the $^{226}\text{Ra}/^{238}\text{U}$ ratio ranges from 0.85 at PH49 (44-46 m) to 85 at PH94 (40-42 m). Previously reported values of measured $^{226}\text{Ra}/^{238}\text{U}$ ratios range from 0.026 to 5300 (Cline et al., 1983; Kanai, 1988; Gascoyne, 1989). In the weathered zone, ^{226}Ra is enriched around PH94 hole (southwest direction from ore zone), and depleted around W2 hole (edge of secondary dispersion fan and south direction from the center of ore zone). Uranium mobility is redox sensitive because the dominant oxidation state of uranium under reducing conditions is U(IV) which is relatively insoluble and immobile, whereas under oxidizing conditions mobile U(VI) species are present. Radium generally has an intermediate mobility between U(IV) and U(VI), but, in contrast to uranium, is less mobile in oxidizing conditions because it is strongly adsorbed by clay and iron minerals which are often present in oxidizing conditions and arise from weathering of the host rock. Therefore, the $^{226}\text{Ra}/^{238}\text{U}$ activity ratio in groundwater is expected to be lower in oxidized conditions (weathered zone) than in reduced conditions (unweathered zone). The lowest value (at W2) may be attributed to ^{226}Ra adsorption by graphite, which is present near this borehole.

5.2.3 Rn-222/Ra-226

Rn-222 is present at levels greatly in excess of those of ^{238}U in Koongarra groundwaters, as is generally observed in groundwater. The activity ratio of $^{222}\text{Rn}/^{226}\text{Ra}$ shows the highest value of 2.0×10^5 at W2 (23-25 m) and lowest value of 8.0×10^2 at C6 (23-24 m) in the weathered zone. The reported range of $^{222}\text{Rn}/^{226}\text{Ra}$ activity ratios in groundwaters is from 10^2 to 10^4 (Lee, 1979; Stenstrand, 1979; Strain, 1979; Asikainen and Kahlos, 1980; Hussain and Krishnaswami, 1980; Asikainen, 1981; King, 1982). The ratios obtained for Koongarra groundwaters are shifted towards higher values. The $^{222}\text{Rn}/^{226}\text{Ra}$ activity ratios of the groundwaters in shallower weathered zone would be expected to be higher than those in deeper unweathered zone, due to the mechanisms (noted above) of Ra adsorption on clay minerals, and the co-precipitation of Ra with Mn and Fe.

Radon gas is a useful tracer to investigate groundwater flow because

a mobility of radon in groundwater is fairly high (Hines et al., 1982). However, ^{222}Rn (with a half-life of 3.8 days) cannot migrate long distance at Koongarra because the velocity of groundwater flow is very slow (about 1 m/yr). Therefore, the distribution of ^{222}Rn should be similar to that of ^{226}Ra , precursor of ^{222}Rn , which would suggest a constant $^{222}\text{Rn}/^{226}\text{Ra}$ activity ratio at different sampling points. However, the results varied widely. This may be due to fast migration of ^{222}Rn through fractures sufficient to create disequilibria even in the short half-life of ^{222}Rn .

5.2.4 Lead-210/Rn-222

Lead-210 is produced, via a number of short-lived intermediates, from the decay of ^{222}Rn . High concentrations of ^{210}Pb were measured in groundwater samples from a number of Koongarra boreholes, particularly from the center of the orebody (Fig. 11). While the measured activities of ^{210}Pb varied over several orders of magnitude, from <0.028 Bq/L to 100 Bq/L, the measured $^{210}\text{Pb}/^{222}\text{Rn}$ activity ratios only ranged from 1.4×10^{-4} to 1.6×10^{-3} . This shows that a major factor determining the activity of ^{210}Pb in these groundwaters is the level of its precursor ^{222}Rn , which is reasonable considering the short half-lives of the intermediate radio-nuclides in the decay chain.

Assuming a simple box model, a scavenging residence time (t) for ^{210}Pb of 1 day was calculated from the $^{210}\text{Pb}/^{222}\text{Rn}$ activity ratio (R) for groundwater at Gujarat, India (Hussain and Krishnaswami, 1980), using the equation:

$$t = 11061 (R/(1-R))$$

(11061 days is the mean lifetime of ^{210}Pb).

At Koongarra, ^{210}Pb residence time of about 6 days can be calculated from the mean $^{210}\text{Pb}/^{222}\text{Rn}$ activity ratio (5.1×10^{-4}). The longer residence time, and the higher relative levels, of ^{210}Pb suggest a slow adsorption reaction of ^{210}Pb to the solid phase, and the possible presence of a semi-stable form of ^{210}Pb in Koongarra groundwater.

6. Horizontal trends and flow patterns

A number of different approaches have been used in studies of geo-chemical trends in Koongarra groundwaters. Giblin and Snelling (1983) concluded that chemical characteristics of groundwater towards PH80 and

PH88 (direction towards C1) was similar to the orebody. In a study of groundwater helium values (Gole et al., 1986), the elevated levels of helium had a similar distribution to that obtained with the chemical characteristics of groundwater, again showing a slight elongation towards PH80. The plan-view of the ^{238}U (Fig. 10) derived in the present study indicates groundwater movement towards the south (towards C1).

Thus, the different investigations of groundwater components have reached essentially similar conclusions, that present groundwater flow paths may well include a component towards the south, which is at an angle to the flow inferred from the extent of the secondary uranium mineralization which extends more perpendicularly away from the fault (towards the south-east). However, it should be emphasized that groundwater geochemistry reflects flow patterns and chemical interactions which have occurred over recent geological times.

7. Migration distance of uranium

The transport of uranium towards C1 (which may be a geologically recent phenomenon) has been discussed above. Figure 14 shows the ^{238}U concentrations along a transect through the orebody. (The transect extends approximately from borehole KD1 across the ore-zone towards borehole PH96 and PH94. In Fig. 14, there is a sharp increase in ^{238}U concentrations, up to as much as three orders of magnitude above background levels, when moving groundwaters intersect the orebody. The variation in U is by about three orders of magnitude, much greater than the range of other ions. Uranium concentrations of groundwaters return to background levels about 200 m down-gradient of the orebody, and this result is consistent with the uranium distribution of solid phase (Edis et al., 1994). This can be attributed to the localized U distribution and to the reduction of U concentrations by adsorption. Therefore the front of elevated U concentrations has migrated by about 200 m since weathering of the primary orebody commenced, although most of the uranium remains very near or within the primary ore body. Furthermore, more recent migration of uranium towards C1 may have occurred. However, the limit of uranium migration towards C1 is unknown due to the lack of data in the region beyond C1 borehole.

A diversity of modeling approaches have been used to estimate the age of the dispersion fan (Golian et al., 1994). The age estimates lie

in the range 0.5 to 3 million years, with a median in the range 1 to 1.5 million years. In the present geochemical conditions have been maintained during the formation of the secondary mineralized zone and the dispersion fan, the migration of uranium over distances up to about 200 m is therefore estimated to have occurred over timescales of 1-1.5 million years.

Acknowledgments

Peter Duerden directed ARAP with great skill and guided this groundwater study. Robin Lowerson and David Garton provided invaluable administrative and technical support. We acknowledge numerous ANSTO and CSIRO staff who carried out chemical and isotopic analysis. Personnel from the Northern Territory Department of Mines and Energy provided capable field assistance. Denison Australia kindly allowed access to Koongarra and provided support in the field. We warmly acknowledge productive interactions with other participants in ARAP throughout this study.

References

- Airey, P.L. (1986) Radionuclide migration around uranium ore bodies in the Alligator Rivers Region of the Northern Territory of Australia - analogue of radioactive waste repositories - a review. *Chem. Geol.* 55, 255-268.
- APHA (1985) Standard Methods for the Examination of Water and Wastewater. 16th Edition, American Public Health Association.
- Asikainen, M. (1981) State of disequilibrium between ^{238}U , ^{234}U , ^{226}Ra and ^{222}Rn in groundwater from bedrock, *Geochim. Cosmochim. Acta* 45, 201.
- Asikainen, M. and Kahlos, H. (1980) Natural radioactivity of drinking water in Finland. *Health Phys.* 39, 77.
- Barnes, I. (1964) Field measurement of alkalinity and pH. 1535-H, USGPO, Washington.
- Brookins, D.G. (1988) Eh-pH diagrams for geochemistry, Springer-Verlag, New York.

- Cline, W., Adamovitz, S., Blackman, C. and Kahn, B. (1983) Radium and uranium concentrations in Georgia community water systems. *Health Phys.* 44, 1.
- Cramer, J.J. (1989) Natural Analog Studies on the Cigar Lake Uranium Deposit: An Update. in CEC Natural analogue working group, Third Meeting. Come, B. and Chapman, N.A. ed. CEC, Brussels, pp.50-56.
- Davis, S.N., Marley, R.D. and Norris, J.R. (1994) Hydrogeological Field Studies. Alligator Rivers Analogue Project Final Report Vol.5, Australian Nuclear Science & Technology Organisation (in press).
- Duerden, P., Golian, C., Hardy, C.J., Nightingale, T. and Payne, T. (1987) Alligator Rivers analogue project. Review of research and its implications for model validation. in Natural Analogues in Radioactive Waste Disposal. Come, B. and Chapman, N.A. ed. Alden Press, Oxford, pp.82-91.
- Edis, R., Cao, L., Cashion, J., Klessa, D., Koppi, A.J., Murakami, T., Nightingale, T., Payne, T.E., Snelling, A. and Yanase, N. (1994) Chemistry and Mineralogy of Rocks and Soil. Alligator Rivers Analogue Project Final Report Vol.8, Australian Nuclear Science & Technology Organisation (in press).
- Gascoyne, M. (1989) High levels of uranium and radium in groundwaters at Canada's Underground Research Laboratory, Lac du Bonnet, Manitoba, Canada. *Appl. Geochem.* 4, 577-591.
- Giblin, A.M. and Snelling, A.A. (1983) Application of hydrogeochemistry to uranium exploration in the Pine Creek Geosyncline, Northern Territory, Australia. *J. Geochem. Explor.* 19, 33-55.
- Gole, M.J., Butt, C.R.M. and Snelling, A.A. (1986) A groundwater helium survey of the Koongarra uranium deposits, Pine Creek Geosyncline, Northern Territory. *Uranium* 2, 343-360.
- Golian, C., Lever, D.A., Baker, A.J., Bennett, D.G., Brandberg, F., Connell, L.D., Kimura, H., Lindgren, M., Murakami, T., Ohnuki, T., Pers, K., Read, D., Skagius, K. and Snelling, A. (1994) Radionuclide transport. Alligator Rivers Analogue Project Final Report Vol.14, Australian Nuclear Science & Technology Organisation (in press).
- Herczeg, A.L. and Payne, T.E. (1992) Recharge and weathering processes in fractured rock aquifers in Northern Australia. The 7th International Symp. on Water-Rock Interaction, Park City, Utah, USA, 561-564.

- Hines, J., Cohen, D., Fried, S. and Friedman, A.M. (1982) The use of ^{222}Rn as a flow path monitor for studies of radionuclide transport in fissures. *Mat. Res. Soc. Symp. Proc.* 6, 187-190.
- Hussain, N. and Krishnaswami, S. (1980) U-238 series radioactive disequilibrium in groundwater: Implications to the origin of excess U-234 and fate of reactive pollutants. *Geochim. Cosmochim. Acta* 44, 1287-1292.
- Ivanovich, M. and Harmon, R.S. (1982) Uranium Series Disequilibrium: Applications to Environmental Problems. Clarendon Press, Oxford.
- Kanai, Y. (1988) Behavior of uranium-238 and its daughter nuclides in the Masutomi spring, Yamanashi Prefecture, central Japan. *Geochem. J.* 22, 285-292.
- King, P.T., Michel, J. and Moore, W.S. (1982) Groundwater geochemistry of ^{228}Ra , ^{226}Ra and ^{222}Rn . *Geochim. Cosmochim. Acta* 38, 1173.
- Lee, R.O., Watson, J.E. Jr. and Fong, S.W. (1979) An assessment of radium in selected North Carolina drinking water supplies. *Health Phys.* 37, 777-779.
- Menager, M.-T., Petit, J.-C. and Brocandel, M. (1992) The migration of radionuclides in granite: a review based on natural analogues. *Appl. Geochem. Suppl. Issue*, 217-238.
- Menet, C., Menager, M.T. and Petit, J.C. (1992) Migration of Radioelements Around the New Nuclear Reactors at Oklo - Analogies with a High-Level Waste Repository. *Radiochim Acta* 58-9, 395-400.
- Murakami, T., Isobe, H. and Edis, R. (1990) Effects of Chlorite Alteration on Uranium Redistribution in Koongarra, Australia. *Mat. Res. Soc. Symp. Proc.* 212, 741-748.
- Nightingale, T.J. (1988) Mobilisation and redistribution of radionuclides during weathering of a uranium orebody. MSC thesis, University of Sydney.
- Nohara, T., Ochiai, Y., Seo, T. and Yoshida, H. (1992) Uranium-Series Disequilibrium Studies in the Tono Uranium Deposit, Japan. *Radiochim. Acta* 58-9, 409-413.
- Ohnuki, T., Watanabe, S. and Murakami, T. (1990) Study on Role of ^{234}Th in Uranium Series Nuclides Migration. *Mat. Res. Soc. Symp.*, Boston, 733-740.
- Payne, T.E., Edis, R., Herczeg, L., Sekine, K., Seo, T., Waite, T.D. and Yanase, N. (1994) Chemistry and Isotopic Composition of Groundwater. Alligator Rivers Analogue Project Final Report Vol.7, Australian

- Nuclear Science & Technology Organisation (in press).
- Petit, J.C. (1990) Migration of radionuclides in the geosphere: what can we learn from natural analogues? *Radiochim. Acta* 51, 181-188.
- Sandino, A. and Bruno, J. (1992) The solubility of $(\text{UO}_2)_3(\text{PO}_4)_2 \cdot 4\text{H}_2\text{O}(\text{s})$ and the formation of U(VI) phosphate complexes: Their influence in uranium speciation in natural waters. *Geochim. Cosmochim. Acta* 56, 4135-4145.
- Snelling, A.A. (1993) Geologic Setting. Alligator Rivers Analogue Project Final Report Vol.2, Australian Nuclear Science & Technology Organisation.
- Stenstrand, K., Annanmaki, M. and Rytomaa, T. (1979) Cytogenetic investigation of People in Finland using Household Water with High Natural Radioactivity. *Health Phys.* 36, 441-444.
- Strain, C.D.a.W., J.E. (1979) An Evaluation of ^{226}Ra and ^{222}Rn Concentrations in Ground and Surface Water Near a Phosphate Mining and Manufacturing Facility. *Health Phys.* 37, 779-783.
- Suutarinen, R., Blomqvist, R., Halonen, S. and Jaakkola, T. (1991) Uranium in groundwater in Palmottu Analogue Study Site in Finland, *Radiochim. Acta* 52/53, 373-380.
- Sverjensky, D.A. (1994) Geochemical Modelling of Present-day Groundwaters. Alligator Rivers Analogue Project Final Report Vol.12, Australian Nuclear Science & Technology Organisation (in press).

Table 1 Geochemical characteristics of the Koongarra groundwaters.

Depth	pH	Eh (mV)	Conductivity ($\mu\text{S}/\text{cm}$)	Ion concentration (mg/L)	Seasonal variation
<12 m	Slightly acidic (6.27)	Oxidized (300)	Low (76)	Low HCO ₃ (40) Mg(4.4)	Large
13-30 m	Neutral (6.82)	Slightly oxidized (168)	High (170)	Medium HCO ₃ (101) Mg(15)	Small
>31 m	Neutral (7.04)	Slightly oxidized (120)	High (202)	High HCO ₃ (153) Mg(22)	Small
Rain water	Acidic (5.2)	Oxidized (555)	Low (17)	Very low (ND)	
Creek water	Acidic (4.6)	Oxidized (485)	Low (18)	Low (0.14)	

The figures in parentheses denote mean value.

ND: no data

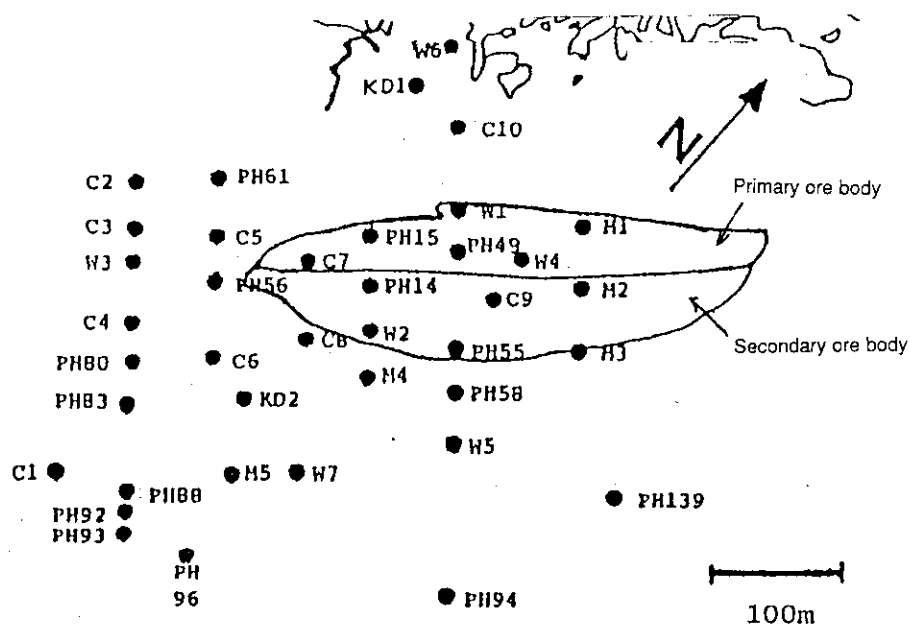


Fig. 1 Horizontal distribution of boreholes used for the groundwater sampling.

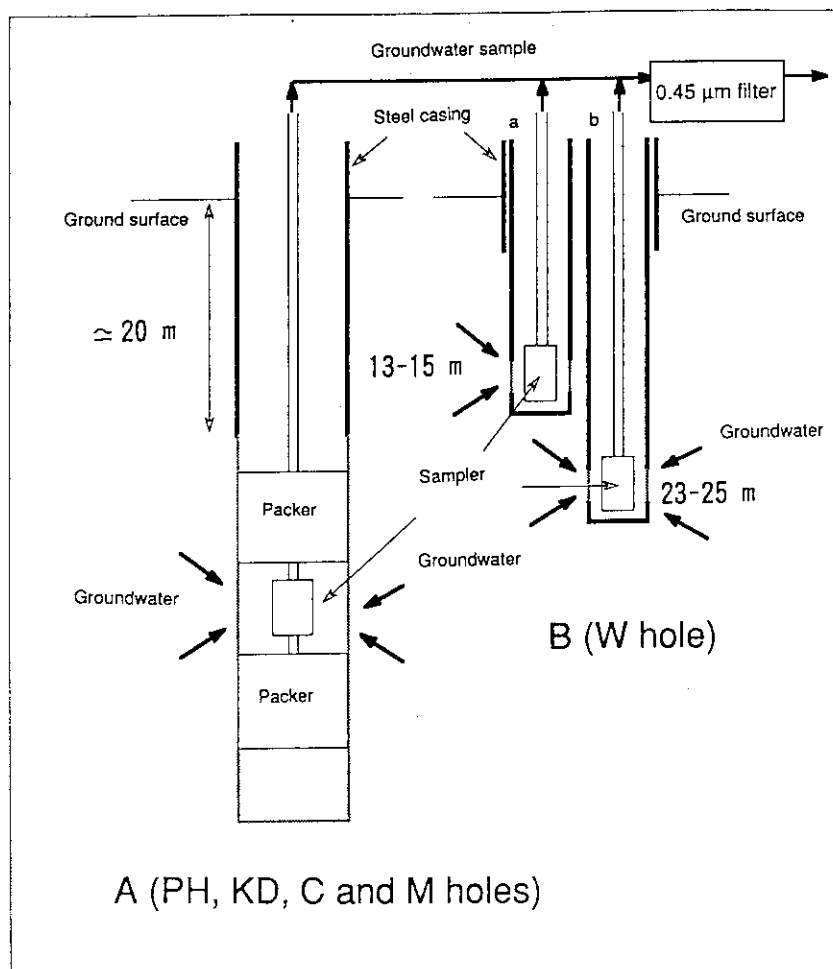


Fig. 2 Groundwater sampling from Koongarra boreholes, A) Double packer sampling, and B) W-series borehole showing separate sampling intervals.

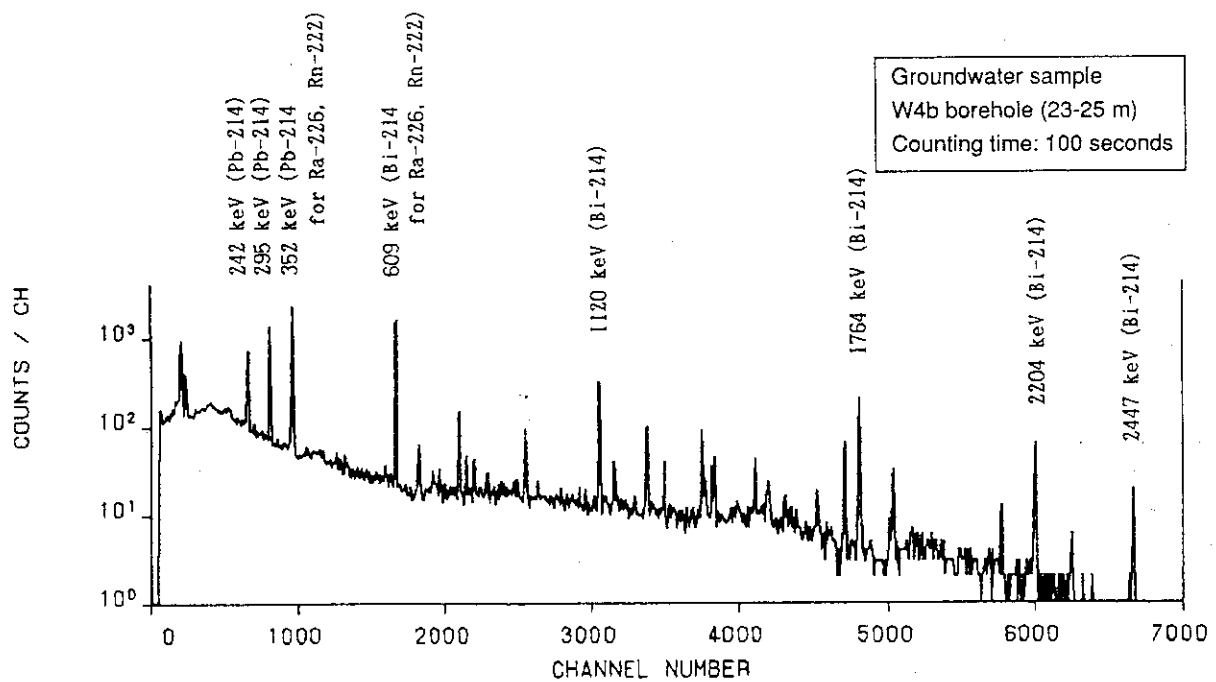


Fig. 3 Gamma-ray spectrum of W4b (23-25 m) groundwater sample measured by the direct method.

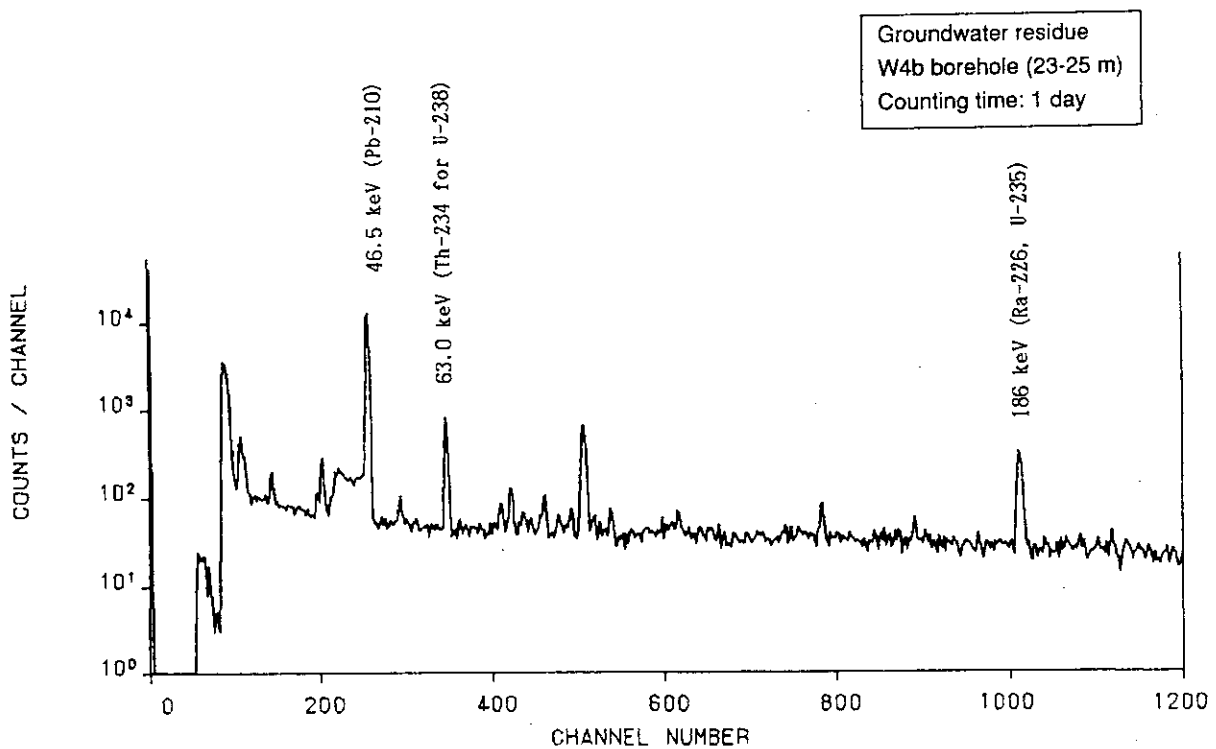


Fig. 4 Gamma-ray spectrum of W4b (23-25 m) groundwater residue measured by the evaporation method.

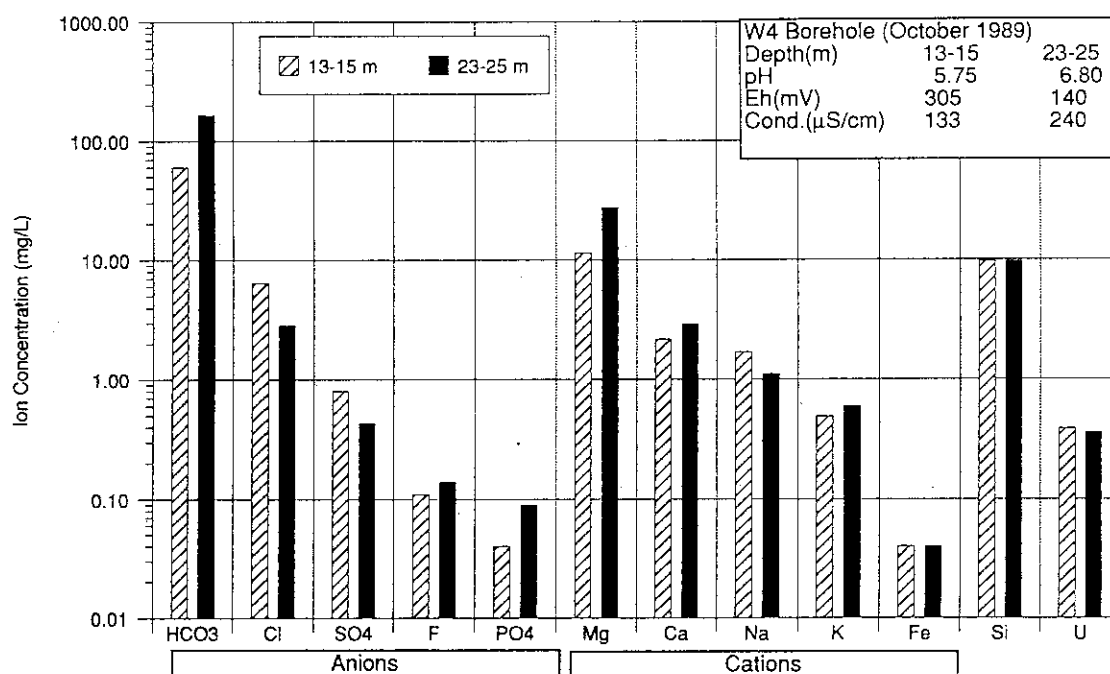


Fig. 5 Geochemical compositions of the groundwaters from W4 borehole.

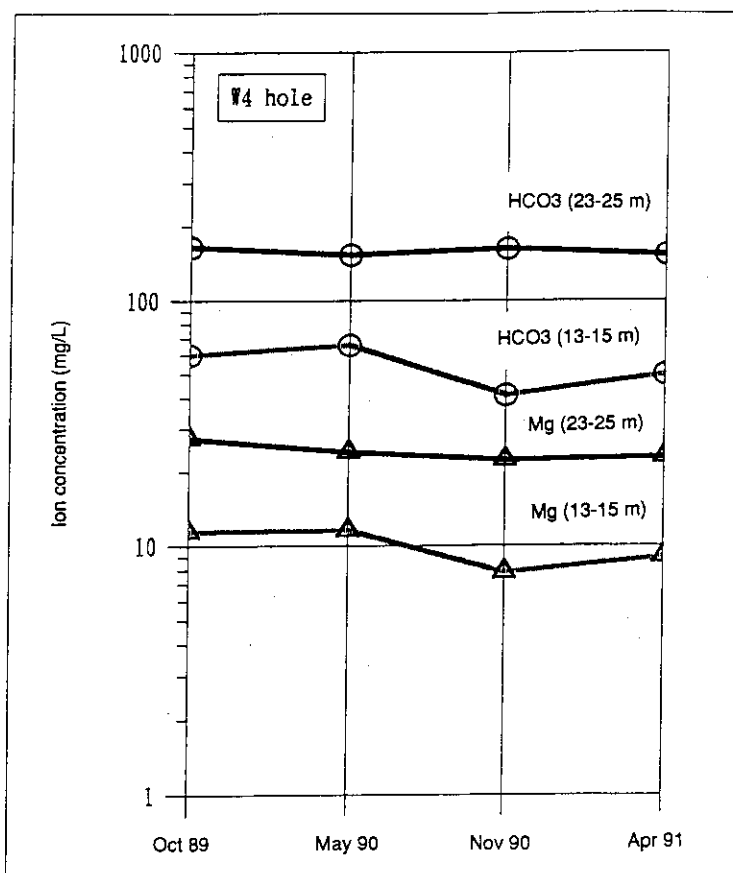


Fig. 6 Variation of magnesium and bicarbonate concentrations for W4 borehole (field trips October 1989 to April 1991).

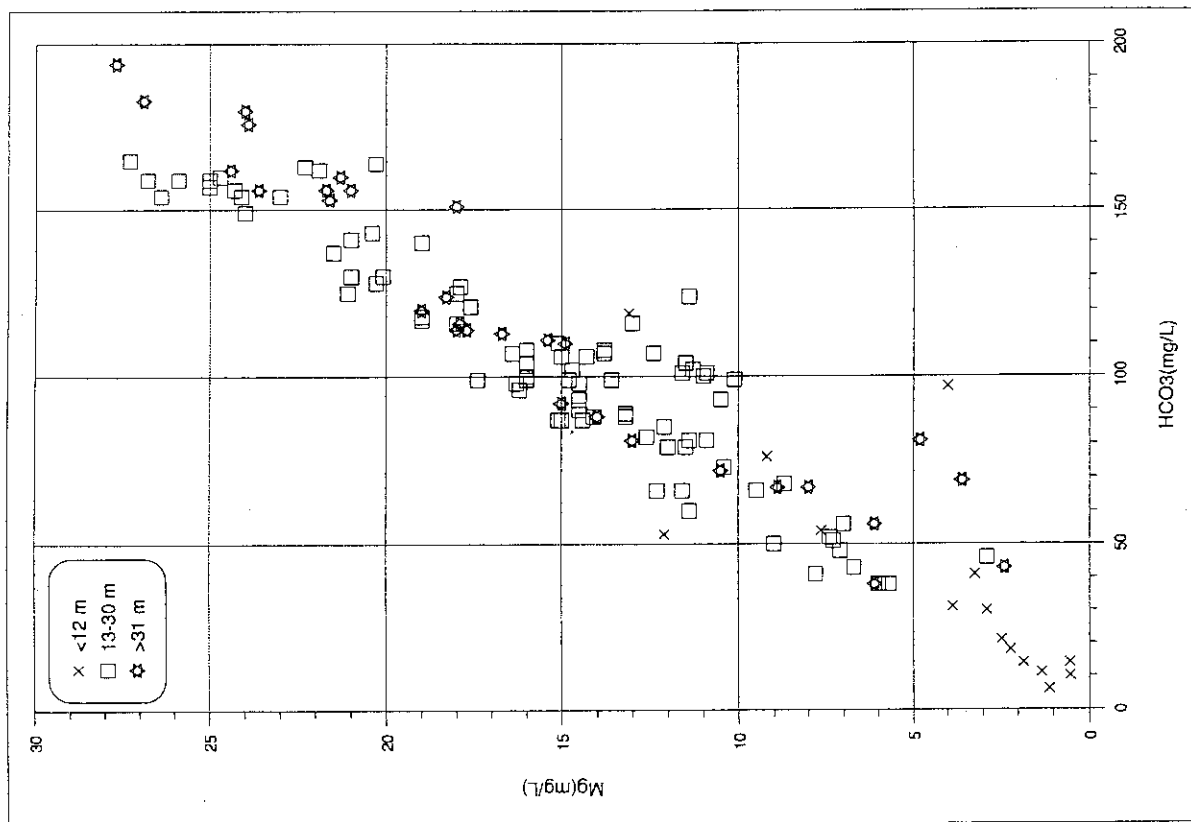


Fig. 8 Correlation between magnesium and bicarbonate concentrations in the Koongarra groundwaters.

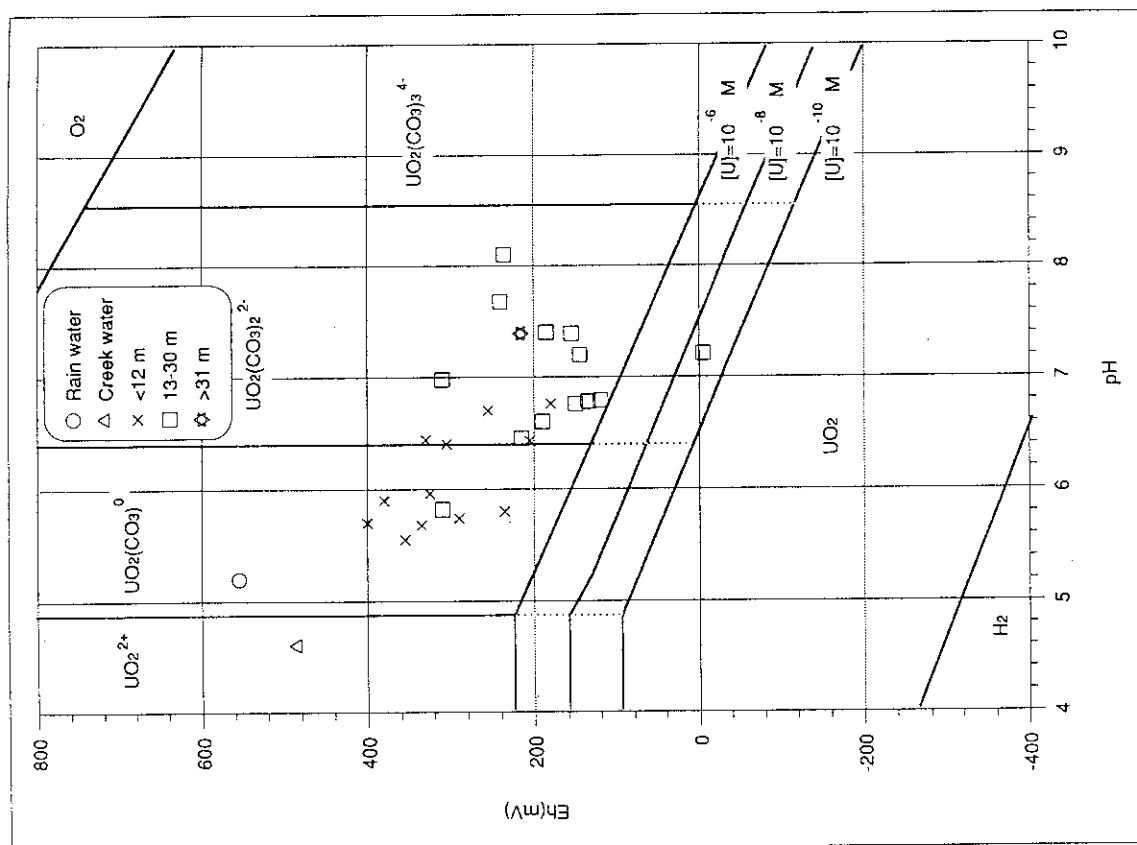


Fig. 7 pH/Eh state of Koongarra groundwater samples (data from April 1991 field trip).

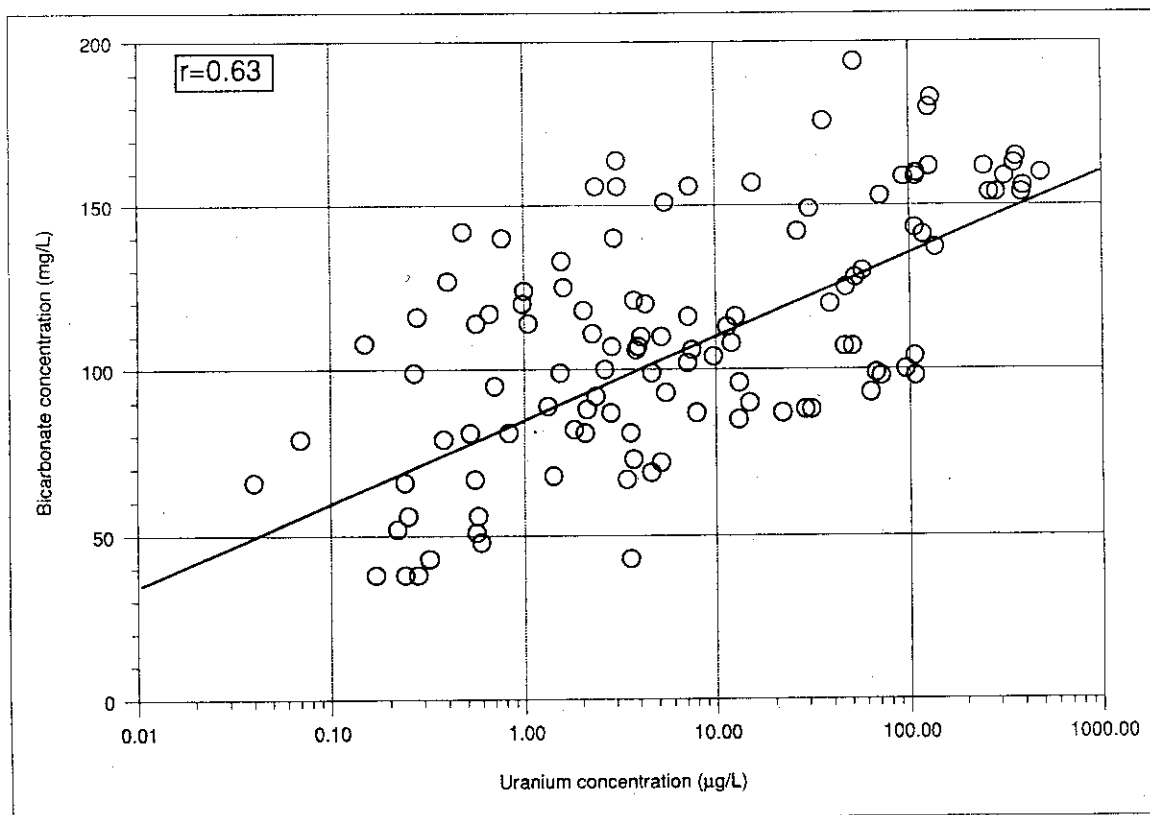


Fig. 9 Correlation between uranium and bicarbonate concentrations in the Koongarra groundwaters.

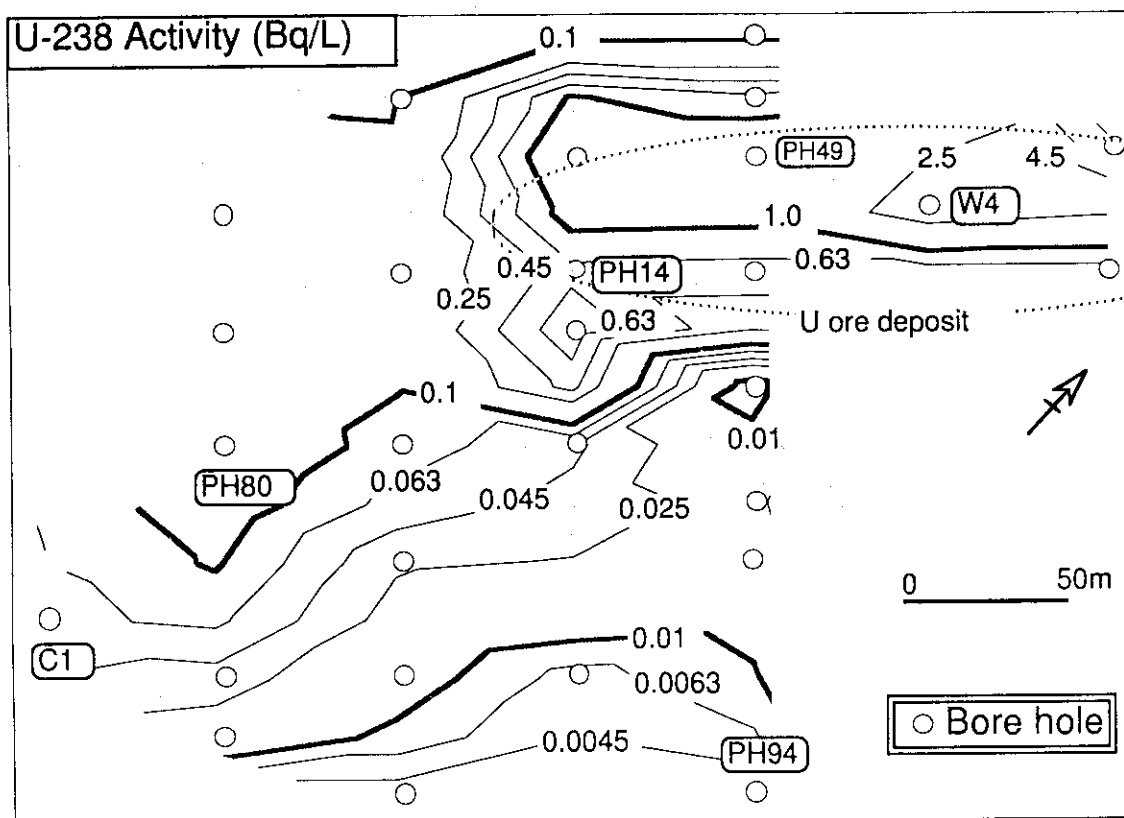


Fig. 10 U-238 concentrations in groundwater (Bq/L)
- contour plan (20-30 m).

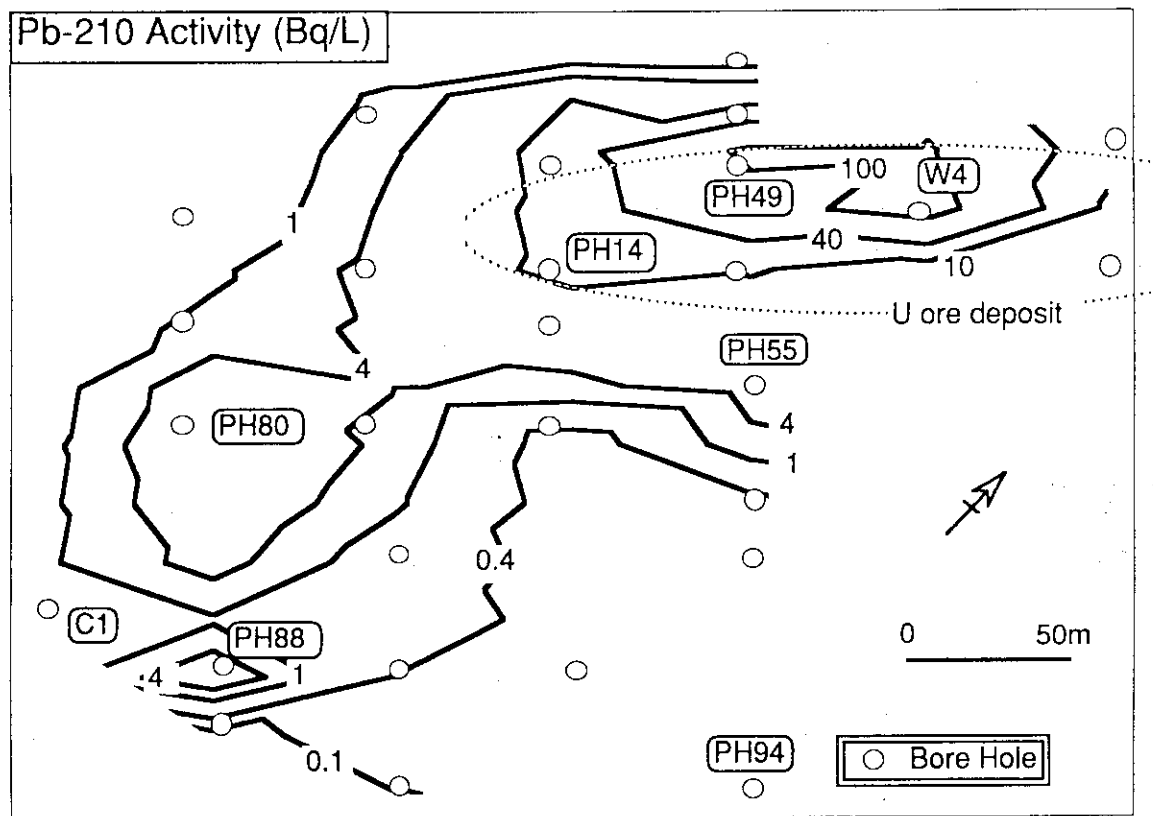


Fig. 11 Pb-210 activities (Bq/L) in groundwater
- contour plan (20-30 m).

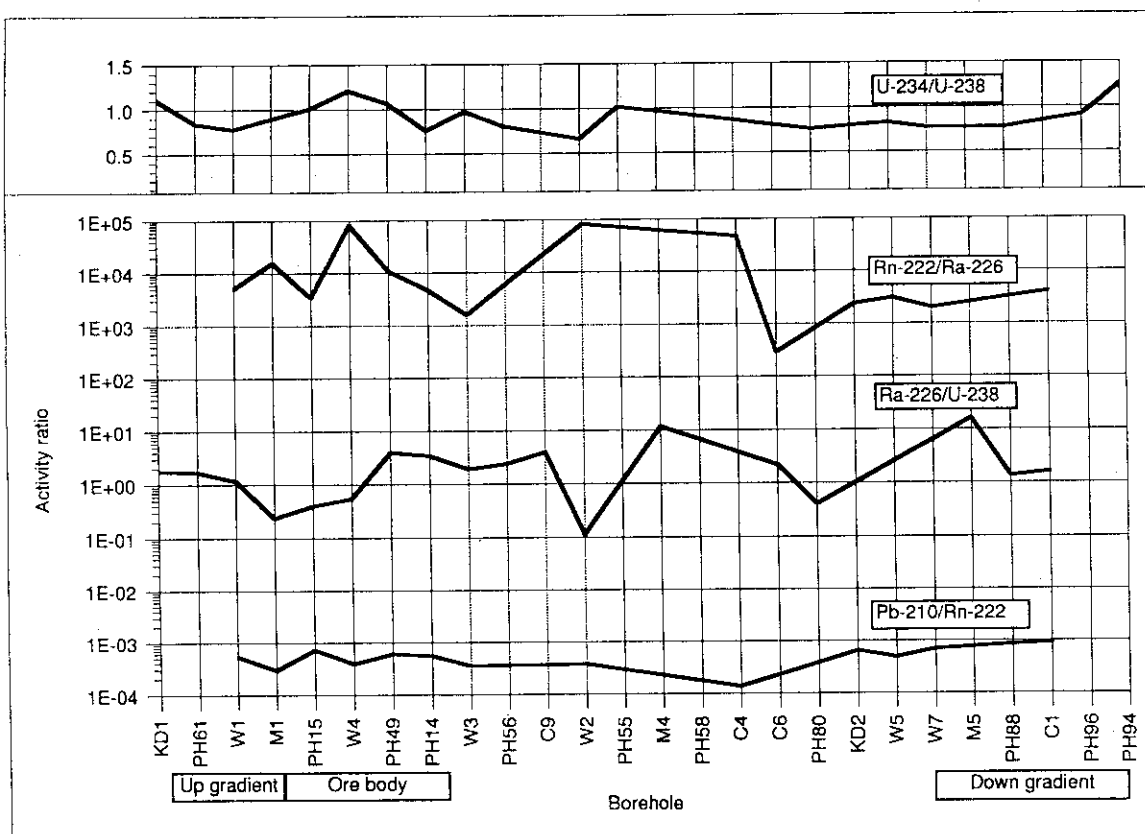


Fig. 12 Variation of mean activity ratios in groundwaters
with the location of boreholes (>16 m).

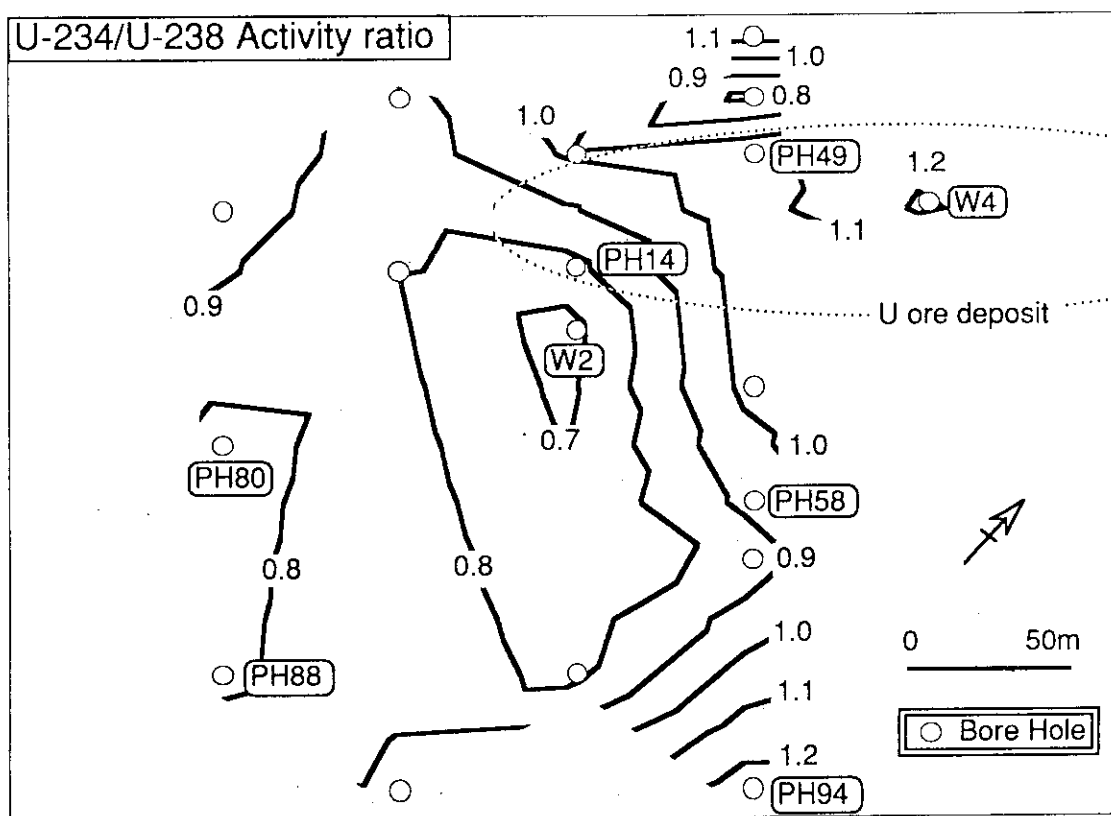


Fig. 13 U-234/U-238 activity ratios in groundwater
- contour plan (20-30 m).

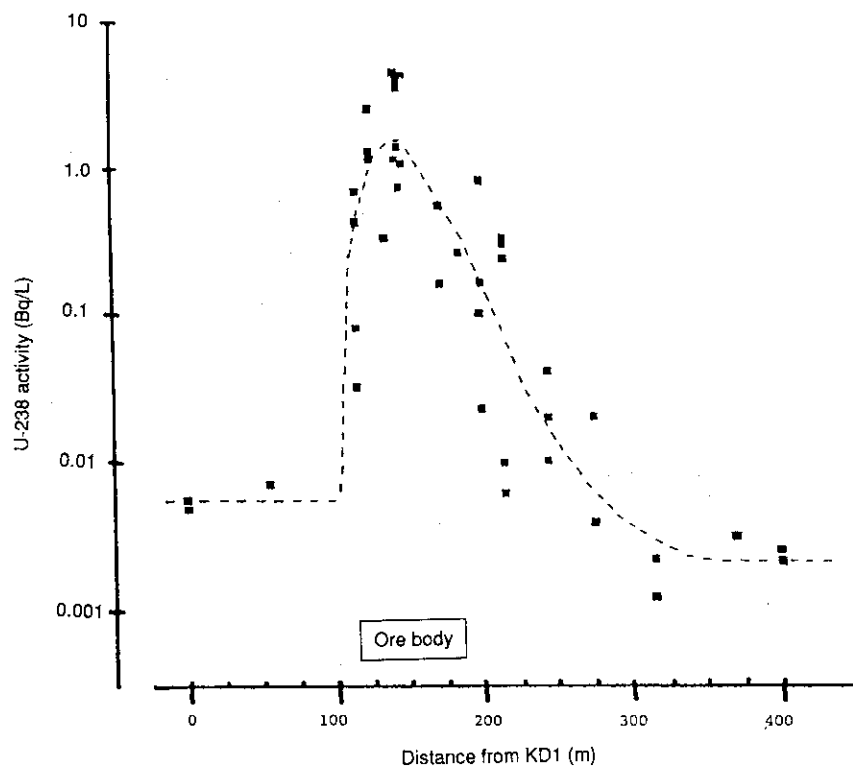


Fig. 14 U-238 activities (Bq/L) in groundwater
as a function of distance from KD1.